Unravelling decadal-scale coastal response to accelerated sea level rise

Han-Yu, Wu

Delft University of Technology

TU Delft

Unravelling decadal-scale coastal response to accelerated sea level rise

by

Han-Yu, Wu

to obtain the degree of

Master of Science

in Civil Engineering

at the Delft University of Technology,

to be defended publicly on Monday September 23, 2024 at 4:00 PM.

Student number:	5849659	
Project duration:	March 1, 2024 – September 23, 2024	
Thesis committee:	Prof. Dr. ir. Sierd de Vries,	TU Delft
	Prof. Dr. ir. Oswaldo Morales Napoles,	TU Delft
	Prof. Dr. Roshanka Ranasinghe,	IHE Delft
	Researcher Johan Reyns,	IHE Delft

Cover: De Pier - Den Haag by Han-Yu Wu

An electronic version of this thesis is available at `http://repository.tudelft.nl/`.

TU Delft

Abstract

Anthropogenic activities induced global warming have caused visible consequences in the increase of atmosphere and ocean temperatures. During the 20th century, the global sea level rise behaves a non-uniformed rising rate. In most of the 20th century, the global mean sea level (GMSL) has risen to around 1.8 mm/yr. However, since the early 90s, this rate has increased beyond 3 mm/yr, and from 2006 – 2018 the rate of rise is 3.7 mm/yr. Many researchers have suggested that relatively moderate changes in sea level can cause significant shoreline changes. One of the most significant impacts of sea level rise can be attributed to the retreat of the shoreline, owing to the permanent passive submersion of lands and coastal erosion. To comprehensively understand the effect of sea level rise on different coastal areas, multiple site-specific data-driven models are developed based on the collected global sandy beach datasets. Based on the long-term evolution of available beach indicators, this research are dedicated to studying spatial and temporal topographic morphological variation as a response to relative regional sea level rise.

Contents

Abstract **i**

1 Introduction **1**
1.1 Research Scope . . . 2
1.2 Research Questions . . . 3
1.3 Thesis Outline . . . 3

2 Methodology **4**
2.1 Coastal and Sea Level Dataset Description . . . 6
2.1.1 NASA . . . 8
2.1.2 Aquitaine . . . 8
2.1.3 Duck . . . 10
2.1.4 Hasaki . . . 12
2.1.5 Jarkus . . . 12
2.1.6 Narrabeen . . . 13
2.2 Coastal Characteristic . . . 15
2.2.1 Shoreline Position . . . 15
2.2.2 Dune Toe Position . . . 16
2.2.3 Beach Width and Volume . . . 16
2.3 Spectral Analysis . . . 18
2.3.1 Inverse Fourier Filter Transform Model . . . 18
2.3.2 Singular Spectrum Analysis . . . 18
2.4 Cross-correlation Analysis . . . 19

3 Result **22**
3.1 Aquitaine . . . 24
3.2 Duck . . . 30
3.3 Hasaki . . . 36
3.4 Jarkus . . . 41
3.5 Narrabeen . . . 50

4 Discussion **57**

5 Conclusion **59**

6 Reference **61**
References . . . 61

7 Equation Derivation Appendix **65**
7.1 Inverse Fourier Filter Transform . . . 65
7.2 Singular Spectrum Analysis . . . 65

List of Figures

2.1 Schematisation of employed methodology in this research. The blue boxes indicate the obtained dataset, the green boxes represent the analysed results, and the red box is the deduced conclusion in combination with the sediment transport hypothesis and quantification of sea level-coast interaction. 5
2.2 The overview of the collected datasets. Five coastal sites and one sea level data were used. 6
2.3 Global and Regional Sea Level Rise 8
2.4 Boucau Station - The Sea level signal in the upper figure includes the vertical land motion and is removed in the lower figure. 8
2.5 The three surveyed cross-sections behaved in a similar morphological variation and were chosen as the research scope. 9
2.6 Yearly measurement of extracted waterline and dune toe position. (seaward positive). Some measurements were extended into the targeting submerged area, resulting in discontinuities. 10
2.7 Two different surveyed cross-section lines at the north of FRF. 10
2.8 Time series of overlooking beach layout of Profile 1097 at FRF (seaward positive). . 11
2.9 Duck Station - The Sea level signal in the upper figure includes the vertical land motion and is removed in the lower figure. 11
2.10 OKADA Station - The Sea level signal in the upper figure includes the vertical land motion and removes it in the lower figure. 11
2.11 The raw time series of overlooking beach layout at HORS. 12
2.12 Den Helder Station - The Sea level signal in the upper figure includes the vertical land motion and is removed in the lower figure. 13
2.13 Ijmuden Station - The Sea level signal in the upper figure includes the vertical land motion and is removed in the lower figure. 13
2.14 Annual Evolution of two Narrabeen beach profiles at the edge of the north (PF1) and the south (PF8) embayment. 14
2.15 The raw time series of overlooking beach layout at Narrabeen PF1 Profile 14
2.16 Sydney Fort Denison Station - The Sea level signal in the upper figure includes the vertical land motion and is removed in the lower figure. 14
2.17 Schematisation of beach cross-section profile. T0 is the pre-storm condition and T1 is the post-storm condition before the regional sea level rise. T2 is the pre-storm condition after the sea level rise. The new equilibrium profile was not depicted for clear illustration in the plot. 15
2.18 Classification of interaction between sea level rise and sediment supply. This figure is derived from (Bosboom & Stive, 2021). 16
2.19 Power spectrum density results of Direct Conversion, Periodogram, and Welch's method. Welch's method provides a smoother spectrum result by averaging over multiple converted spectra. 18
2.20 Demonstration of the inverse Fourier filter transform model. The large-year filter would smear out the linear trend or the offset events. 19
2.21 Two toy datasets were decomposed into three eigenmodes by singular spectrum analysis. The applied window size L in the upper figures is N/25 = 4 data points, which simulates the detail of the trend. The window size in the lower figure is N/4 = 25 data points, which better separates the raw signal into various components. 20

3.1 (a) The upper figure shows spectrum results from three approaches (periodogram, direct conversion, and Welch's method), where the Welch method is adopted in this research for better performance. The colour lines depicted in the lower figure are derived spectrum by applying different window sizes. (b) Pronounced seasonal mechanisms detected by Welch's method where the occurrence amount of stars in (a) exceeds two. Different year-values represent the seasonality in the 22
3.2 Demonstration of filtered signals. Three prominent cut-off years are chosen. The reconstructed signals by using 6.552 and 7.645 cut-off years are overlapped, suggesting the magnitude of this 7.645-year event contributing to the original signal might be weak. 23
3.3 Demonstration of remaining high-frequency mechanisms in the SSA results despite a large window size adoption. 23
3.4 Aquitaine: Evolution of three cross-section profiles north (Profile L9) and south (Profile L11) to the pier. The colour lines show profile development through time, the measurement duration is divided into 10 segments for clarity display. Beach volume is calculated from the mean sea level to the dune front position 24
3.5 Aquitaine: Singular spectrum decomposition of sea level and topographic signal for the first eigenmode. N is the total amount of data points where the window size depends on the computation efficiency and high-frequency mechanisms to filter out. 25
3.6 Aquitaine: Singular spectrum decomposition of sea level and topographic signal for the first eigenmode. N is the total amount of data points where the window size depends on the computation efficiency and high-frequency mechanisms to filter out. 27
3.7 Aquitaine: Singular spectrum decomposition of sea level and topographic signal for the first eigenmode. N is the total amount of data points where the window size depends on the computation efficiency and high-frequency mechanisms to filter out. 28
3.8 Aquitaine - Normalized cross-correlation between sea level surface and coastal indicators where the heat map and confidence interval are grounded on zero time-lag results. The legend pairs represent the combination of representative pairs, "sea level data cutting year - indicator cutting year". 29
3.9 Duck: Evolution of two cross-section profiles north (Profile 1097) and south (Profile -91) to the pier. The measurement duration is divided into 10 segments for clear display. Beach volume is calculated from the depth of closure to the dune toe position. 30
3.10 Duck: Singular spectrum decomposition of sea level and topographic signal for the first eigenmode. N is the total amount of data points where the window size depends on the computation efficiency and high-frequency mechanisms to filter out. 31
3.11 Duck: Singular spectrum decomposition of sea level and topographic signal for the first eigenmode. N is the total amount of data points where the window size depends on the computation efficiency and high-frequency mechanisms to filter out. 33
3.12 Duck: Singular spectrum decomposition of sea level and topographic signal for the first eigenmode. N is the total amount of data points where the window size depends on the computation efficiency and high-frequency mechanisms to filter out. 34
3.13 Duck - Normalized cross-correlation between sea level surface and coastal indicators where the heat map and confidence interval are grounded on zero time-lag results. The legend pairs represent the combination of representative pairs, "sea level data cutting year - indicator cutting year". 35
3.14 Hasaki: Singular spectrum decomposition of sea level and topographic signal for the first eigenmode. N is the total amount of data points where the window size depends on the computation efficiency and high-frequency mechanisms to filter out. 36
3.15 Hasaki: Singular spectrum decomposition of sea level and topographic signal for the first eigenmode. N is the total amount of data points where the window size depends on the computation efficiency and high-frequency mechanisms to filter out. 38

3.16 Hasaki: Singular spectrum decomposition of sea level and topographic signal for the first eigenmode. N is the total amount of data points where the window size depends on the computation efficiency and high-frequency mechanisms to filter out. 39
3.17 Hasaki - Normalized cross-correlation between sea level surface and coastal indicators where the heat map and confidence interval are grounded on zero time-lag results. The legend pairs represent the combination of representative pairs, ”sea level data cutting year - indicator cutting year”. 40
3.18 Noordwijk: Singular spectrum decomposition of sea level and topographic signal for the first eigenmode. N is the total amount of data points where the window size depends on the computation efficiency and high-frequency mechanisms to filter out. 41
3.19 Egmond: Singular spectrum decomposition of sea level and topographic signal for the first eigenmode. N is the total amount of data points where the window size depends on the computation efficiency and high-frequency mechanisms to filter out. 42
3.20 Noordwijk: Singular spectrum decomposition of sea level and topographic signal for the first eigenmode. N is the total amount of data points where the window size depends on the computation efficiency and high-frequency mechanisms to filter out. 44
3.21 Noordwijk, Jarkus: Singular spectrum decomposition of sea level and topographic signal for the first eigenmode. N is the total amount of data points where the window size depends on the computation efficiency and high-frequency mechanisms to filter out. 45
3.22 Noordwijk, Jarkus - Normalized cross-correlation between sea level surface and coastal indicators where the heat map and confidence interval are grounded on zero time-lag results. The legend pairs represent the combination of representative pairs, ”sea level data cutting year - indicator cutting year”. 46
3.23 Egmond: Singular spectrum decomposition of sea level and topographic signal for the first eigenmode. N is the total amount of data points where the window size depends on the computation efficiency and high-frequency mechanisms to filter out. 47
3.24 Egmond, Jarkus: Singular spectrum decomposition of sea level and topographic signal for the first eigenmode. N is the total amount of data points where the window size depends on the computation efficiency and high-frequency mechanisms to filter out. 48
3.25 Egmond, Jarkus - Normalized cross-correlation between sea level surface and coastal indicators where the heat map and confidence interval are grounded on zero time-lag results. The legend pairs represent the combination of representative pairs, ”sea level data cutting year - indicator cutting year”. 49
3.26 Narrabeen: Evolution of PF1 cross-section profile. The measurement duration is divided into 10 segments for clear display. Beach volume is calculated from the land-water interface to the dune toe position. 50
3.27 Narrabeen: Singular spectrum decomposition of sea level and topographic signal for the first eigenmode. N is the total amount of data points where the window size depends on the computation efficiency and high-frequency mechanisms to filter out. 51
3.28 Narrabeen: Singular spectrum decomposition of sea level and topographic signal for the first eigenmode. N is the total amount of data points where the window size depends on the computation efficiency and high-frequency mechanisms to filter out. 52
3.29 Narrabeen: Singular spectrum decomposition of sea level and topographic signal for the first eigenmode. N is the total amount of data points where the window size depends on the computation efficiency and high-frequency mechanisms to filter out. 53
3.30 Narrabeen - Normalized cross-correlation between sea level surface and coastal indicators where the heat map and confidence interval are grounded on zero time-lag results. The legend pairs represent the combination of representative pairs, ”sea level data cutting year - indicator cutting year”. 54

List of Tables

1.1 Data Resources 3

2.1 Metadata of collected raw dataset 6
2.2 Definition of beach characteristic. 7

3.1 Aquitaine: Linear Fitting results of the SSA and IFFT filtered signal, the cut-off year in IFFT Model is 7.115 year and the window size in SSA Model is N/3. The symbol means that there is no statistical evidence proving the changing rate is non-zero. SL: sea level variation, SP: shoreline position, DP: dune toe position, BW: beach width . 26
3.2 Duck Profile 1097: Linear Fitting results of the SSA and IFFT filtered signal, the cut-off year in the IFFT Model is 6.552 years and the window size in the SSA Model is N/10. SL: sea level variation, SP: shoreline position, DP: dune toe position, BW: beach width 32
3.3 Hasaki: Linear Fitting results of the SSA and IFFT filtered signal, the cut-off year in IFFT Model is 5.611 year and the window size in SSA Model is N/10. SL: sea level variation, SP: shoreline position, DP: dune toe position, BW: beach width 37
3.4 Noordwijk, Jarkus: Linear Fitting results of the SSA and IFFT filtered signal, the cut-off year in IFFT Model is 7.116 year and the window size in SSA Model is N/3. SL: sea level variation, SP: shoreline position, DP: dune toe position, BW: beach width 43
3.5 Egmond, Jarkus: Linear Fitting results of the SSA and IFFT filtered signal, the cut-off year in IFFT Model is 7.762 year and the window size in SSA Model is N/3. SL: sea level variation, SP: shoreline position, DP: dune toe position, BW: beach width . 43
3.6 Narrabeen: Linear Fitting results of the SSA and IFFT filtered signal, the cut-off year in IFFT Model is 11.222 year and the window size in SSA Model is N/11. SL: sea level variation, SP: shoreline position, DP: dune toe position, BW: beach width . . . 51
3.7 The Inverse Fourier Filtering Model Result 55
3.8 The Singular Spectrum Analysis Model Result 56

Introduction

Increasing heat-trapping greenhouse gas generated from anthropogenic fossil fuel combustion causes Earth's warming climate. The IPCC AR6 Synthesis Report (Core Writing Team, 2023) indicates that incremental changes of compound extreme events due to climate changes impose more possible concurrent and repeated climate hazards to extensive ranges. As a key indicator revealing climate changes, sea levels have gradually encroached on the coastal areas at an accelerating rate in the last century. The most apparent impact of sea level rise is the permanent and irreversible inundation of low-elevation regions. The corresponding coastal impacts include degradation of livelihoods, flood risk, infrastructure deconstruction, and industry threat. Besides the visible deterioration of habitable lands, latent hazards include slat water intrusion to freshwater aquifers and nearby soils, penetration of storm surge, and coastal erosion. Apart from these physical phenomena, (Hauer et al., 2020) indicated that sea level rise could also threaten multiple social-economical aspects, such as tourism, fisheries, silviculture, and coastal agriculture, forcing local communities to migrate. These socioeconomic, demographic, and cultural factors are regarded as disincentives that expel people to migrate out of the coastal areas (Hauer et al., 2020; Lincke & Hinkel, 2021).

Global mean sea level variations provide an important measure of the warming climate, yet the sea level rising rate shows a significant regional difference (Spada et al., 2013; Stammer et al., 2013). The regional variability in sea level can be attributed to multiple physical processes that vary both spatially and temporally (Cazenave & Cozannet, 2014; Stammer et al., 2013). In addition, from the topographic aspect, regional heterogeneity in coastal evolutions can also be expected, where the interactions are strongly subjected to local hydrodynamic conditions and sediment sources/sinks. It is thus more important to perceive the influence of regional sea level rise while assessing potential coastal impacts. In correspondence to the site-specific mechanisms, a serious challenge obstructing the early studies of the impacts of regional sea level rise is the lack of available topographic data. The surveys provided barely enough temporal and spatial resolution to capture the dynamics of beaches (Le Cozannet et al., 2014). An intra-decadal dataset can be appropriate for observing long-term beach morphological evolution (Larson et al., 2000; Aagaard et al., 2004; Larson et al., 2003), while postulationally not an adequate temporal scale for sea level rise studies. This becomes more significant when comparing the global datasets which are restricted to inconsistent measurement frequencies and diverse measuring targets.

In coastal dynamics, the sandy beach morphology encompasses numerous aleatoric uncertainties within the natural and anthropogenic coastal processes (Dean & Houston, 2016; Bosboom & Stive, 2021; Dastgheib et al., 2022). These involved mechanisms interact nonlinearly with active coastal zones on spatial and temporal scales (Cazenave & Cozannet, 2014; Coco & Murray, 2007; Hesp, 2002) and can be classified into natural sediment mechanisms (hydrodynamical transportation, aeolian transportation, river supplement etc.) and human interventions (coastal engineering, upstream river engineering, dredging etc.). As the primary factors shaping the coastal landscape, Woodworth et al. (2019) reviewed the hydrodynamic forcing factors affecting the coastal sea level. The higher frequency events (e.g. wave and tide) tend to have a profound magnitude at the coast due to resonance and other dynamics. Besides, these short-term mechanisms are comparably more visible from the observation aspect. In contrast, the contributions to the landscape from the sea level rise are long-term, gradual, and implicit, which requires decadal surveying signals to reveal the embedded trends. This renders another conspicuous obstacle in studying sandy beach responses to accelerating sea level rise.

Within the decadal years, massive research has been proposed to study the sea level rise phenomenon and its accompanying impacts on coastal areas. The most widely known method for determining shoreface profile response to sea level rise is the Bruun rule developed in 1962 (Bruun, 1962). It argued that the shore profile maintains vertically spatiotemporal invariance to the mean sea level owing to the relatively rapid upper shoreface adaption to the slow-rising mean sea level. The shoreline thus retreats to supply the sediment into the submerged area. Nevertheless, in reality, this will

only satisfy without any other external forces. Owing to the increasing threats from unprecedented coastal recession, this deterministic method which depends on highly uncertain estimates has been challenged, and more revised frameworks are proposed. Cazenave and Cozannet (2014) reviewed the contemporary research approaches and indicated two main types of methodology, proposed to evaluate the impacts of sea-level changes on shoreline changes. The first one is the observation-based approach, studying the relationship between sea level and shoreline response by analysing the spatial and temporal. The other is the model-based approach, which predicts shoreline change from the coastal model to field observations.

Various model-based approaches are thus proposed to tweak the Brunne rule and predict the future sea level rise-induced risks in coastal management. Dean and Houston (2016) developed a deterministic model including the sediment budget from cross-shore transport, alongshore gradient and sediment source/sink to describe the shoreline variation. Ranasinghe et al. (2012) proposed a process-based model describing the probabilistic estimate of sea level rise-driven coastal recession. Dastgheib et al. (2022) applied the probabilistic coastline recession model on coastal management and studied the coastal retreat. Lentz et al. (2016) considered coastal elevation, vertical land movement, and probabilistic sea level rise projection to develop a probabilistic model to evaluate the likelihood that a region will be inundated or dynamically adapted. Luque et al. (2023) derived an analytical shoreline evolution equation based on the premise of the equilibrium beach profile.

In addition to the beach characteristics responses, sea level rise may also deteriorate the formation of coastal nature communities. Feagin et al. (2005) indicated that the severe IPCC scenario resulted in the breakdown of the distribution of colonisation vegetation on the foreshore. This isolated and ephemeral nature can not counterbalance the stress of the rising sea level and further fails to establish a community succession. Schuerch et al. (2018) studied the relationship between the development of tidal wetlands and accommodation spaces for retreating and suggested the correlation of sea level rise to the inland migration of tidal wetlands. Phillips (2018) studied the changes in multiple environmental gradients and reported their negative reflections on the relative sea level rise.

The aforementioned researches declare that coastal hydrodynamic, geodynamic, biological, and anthropogenic factors render coastal reactions more intricate, leading to difficulty in assessing the impact of sea level rise, especially on a global scale. The influence of sea level rise can be amplified due to the static and steric effect while dissipated since other coastal processes are still dominated (Cazenave & Cozannet, 2014). van IJzendoorn et al. (2021) indicated that the ambient sediment transport is more dominant than the sea level rise causing erosion by showing that the dune foot prograding rate is much larger than the sea level rising rate. Moreover, Harley et al. (2022) proposed that a single extreme storm can offset the decadal shoreline retreat due to sea level rise. Although massive models on the prediction and evolution of sandy coast landforms at a decadal to multi-decadal time scale have been widely investigated, no direct correlation between the sea level rise and sandy beaches in terms of global scales is quantified. To quantitatively study the correlation between coastal response and accelerated sea level rise is still obscure. This master thesis research is dedicated to integrating the geometric characteristics of the sandy beaches and statistically proving the relations between regional sea level rise and coastal topographical morphology. From this, research questions and research scopes are proposed as follows.

1.1. Research Scope

This research project is in collaboration with IHE Delft (the Netherlands) and retrieved the observation dataset from Oregon State University (USA), Bureau de Recherches Géologiques et Minières (BRGM) (France), and Tohoku University (Japan). Five sandy beach datasets are selected as the representativeness to analyse the time series of coastal characteristics. Coastal morphological processes involved in each system will be discussed and eliminated to obtain actual responses from sea level rise. Since part of the utilized raw measurement data is authorised by these institutes, a non-disclosure agreement should be fulfilled. As for the open datasets utilized in this research, they are

only for academic research usage. Details are shown in Table 1.1.

Table 1.1: Data Resources

Dataset	Location	Institution	Type
JarKus	The Netherlands	Delft University of Technology	Open Data
Hazaki	Japan	Tohoku University	Authorized
Duck	USA	United States Geological Survey	Open Data
Aquitaine	France	Bureau de Recherches Géologiques et Minières	Open Data
Narrabeen	Australia	University of New South Wales Water Research Laboratory	Open Data
NASA	USA	NASA Sea Level Evaluation Assessment Tool	Open Data

1.2. Research Questions

The main content that the research aims to address is to unravel the correlation between sandy coast evolution and relative sea level rise at the decadal temporal scale. Relevant research sub-questions are proposed as follows:

1. How to remove the embedded high-frequency morphological mechanisms and disclose reaction to the sea level rise in the observation dataset?
2. Can the model derive the morphological evolution trend of the beach characteristic?
3. To what extent does regional variability between the global coastal sites affect the coastal response to rising sea level signals?
4. Does the coastal profile present distinguish morphological evolution after the 1990s accelerating sea level rise?

1.3. Thesis Outline

Chapter 1 includes the background information relevant to the research of interest, from which the research objectives and utilized dataset in this study were introduced.

Chapter 2 describes the collected dataset and adopted methodology in this research. First, both sea level data and topographic data will be introduced, including their geographical properties and metadata. Next, the working pipeline of methodology will be elaborated. Detailed applied techniques will further be explained section by section.

Chapter 3 presents the results from all adopted methodologies mentioned in Chapter 2. Normalized signal cross-correlation will be derived among different coastal indicator signals and sea level signals to show the relations between the sea level signal and the topographic signal.

Chapter 4 discusses the implemented simplifications and populations while building the models and processing the data. Besides, the model limitation and potential uncertainty will also be mentioned. In this chapter, future working directions and notable factors that might dominate the system will also be mentioned.

Chapter 5 summarises the discovered phenomena and conclusion in master thesis research.

Methodology

This chapter will discuss the datasets' coastal characteristics and the methodology utilised in this research. Figure 2.1 presents the schematisation of the detailed data processing pipeline. Firstly, the geography of the coasts will be briefly introduced site by site in Section 2.1, and from there, the motivation for selecting specific cross-sections as the research candidates will be proposed. A good nomination for researching transactions within the coastal site can significantly eliminate aleatoric uncertainties embedded in sediment transportation. Furthermore, the data pre-processing procedures will be elaborated based on the temporal duration and the surveying resolution of various collected topographic datasets. The format of obtained raw datasets at Aquitaine, Duck, Jarkus, and Narrabeen are consecutively measured cross-section profiles and at Hasaki is the time series of specific indicator locations. Details can be found in the subsections of each coastal site. Secondly, Section 2.2 will discuss the definition of adopted beach characteristics in this research. Three distinct indicators (shoreline position, dune toe position, and beach width) were used to reflect the coastal responses to ocean dynamics and rising sea levels. Another utilized indicator is the time series of beach volume, which provides the general sediment increment or reduction behaviour. Next, the detailed employed time series analysis and signal processing techniques will be elaborated in Section 2.3. Two models applied in this research will be introduced, The Inverse Fourier Filter Transform (IFFT) Model and the Singular Spectrum Analysis (SSA) Model. Results from these two approaches will be compared to reduce the epistemic uncertainty within the developed model. Finally, to discover the correlation between filtered sea level signals and filtered topographic signals, Section 2.4 will talk about the theory of signal cross-correlation. In this section, the bootstrapping method will study the reliability of cross-correlation between sea level signals and topographic signals.

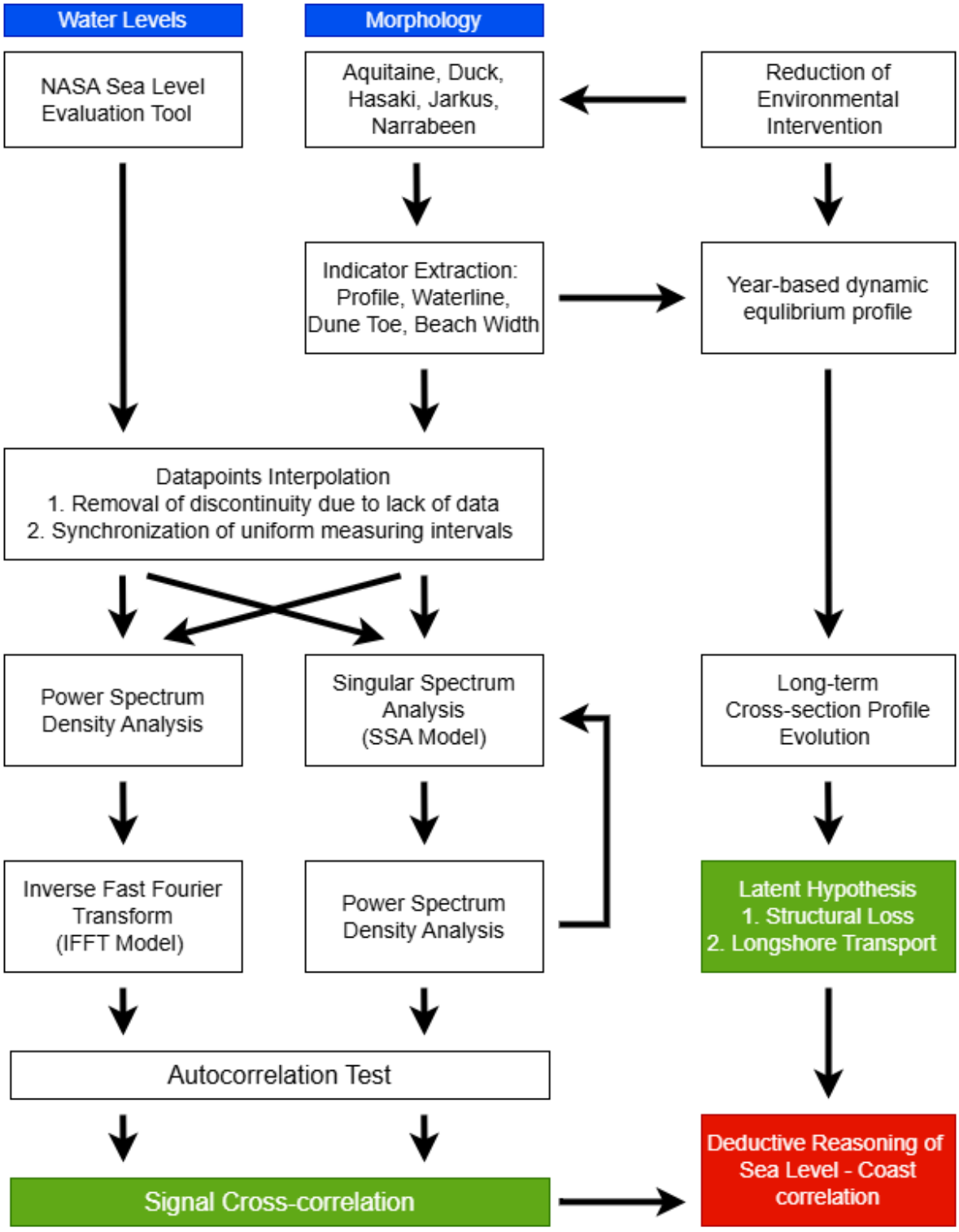

Figure 2.1: Schematisation of employed methodology in this research. The blue boxes indicate the obtained dataset, the green boxes represent the analysed results, and the red box is the deduced conclusion in combination with the sediment transport hypothesis and quantification of sea level-coast interaction.

2.1. Coastal and Sea Level Dataset Description

Given the research scope, Figure 2.2 illustrates the research location of the global dataset. These datasets provide intact surveying measurement record, containing decadal measurement data points with an appropriate and feasible temporal resolution. Table 2.1 summarizes the metadata of five coastal sites and their respectively nearest sea level stations obtained from NASA's "Sea Level Evaluation & Assessment Tool". Most of the obtained datasets were accessed as multiple transactions, and the format of the Hasaki dataset was the time series of indicators. The target transactions were selected based on the reduction of the environmental sediment transport effects, such as the outflow of the upstream basin and beach nourishment, and the amount of available measurements. The targeting profile should contain the most surveys which extend into the upper shoreface and enclose the beach indicators. Moreover, the temporal duration of these profiles should overlap with the record duration of sea level data due to the morphological causality. Links to all data resources can be achieved in the acknowledgement section.

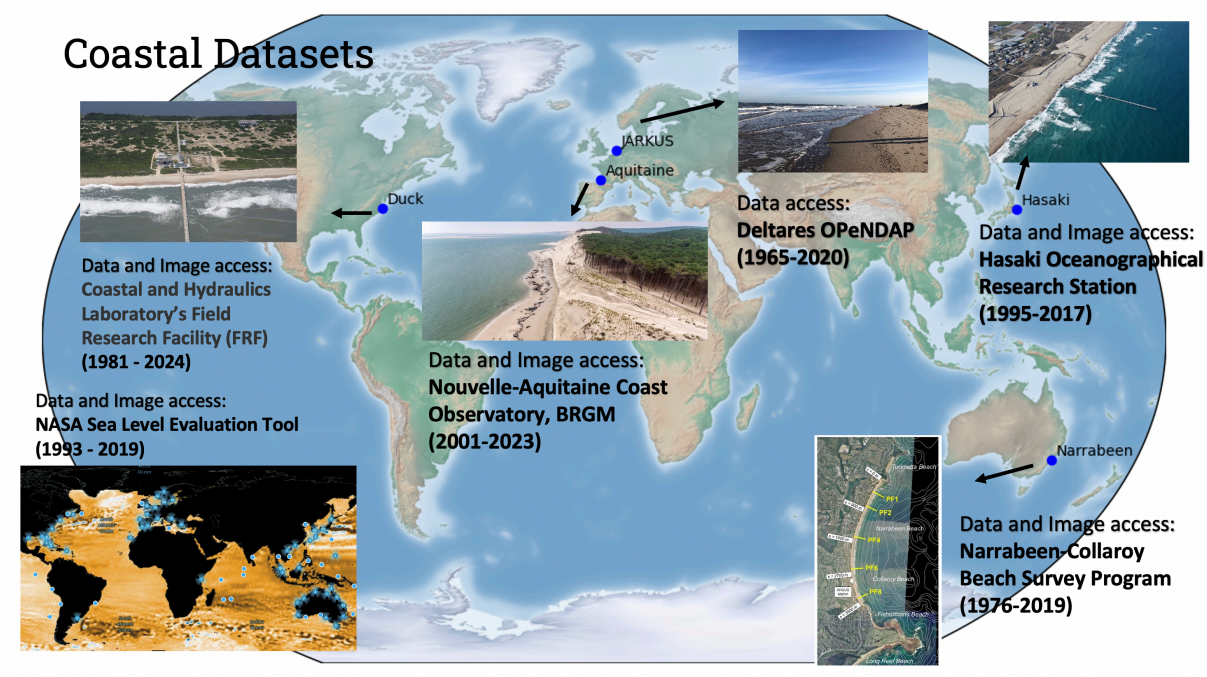

Figure 2.2: The overview of the collected datasets. Five coastal sites and one sea level data were used.

Table 2.1: Metadata of collected raw dataset

Dataset	Location	Time Span	Raw data	NASA Sea Level station
JarKus	The Netherlands	1965 - 2020	Cross-section Profile	Den Helder , IJMUIDEN
Hazaki	Japan	1995 - 2017	Coastline, Berm, Dune Toe Coordinate	Okada
Duck	USA	1974 - 2024	Cross-section Profile	Oregon Inlet Marina
Aquitaine	France	2008 - 2023	Cross-section Profile	Boucau
Narrabeen	Australia	1976 - 2019	Cross-section Profile	Fort Denison
NASA	USA	1993 - 2019	Sea Level Variation	-

With decadal measurement, nowadays, the duration of collected data may be long enough to capture the implicit reaction of the sandy coasts (see Table 2.1). Hence, according to the comparison among global coastal sites, the beach characteristics are defined pragmatically, shown in Table 2.2. Followed by the underlying principles for obtaining coastline position, dune toe position, and beach/width volume are calculated from various datasets. Hereby the direction of the coastal profile is seaward positive and landward negative in all coastal sites. MSL: Mean Sea Level, MHW: Mean High Water, DoC: Depth of Closure, E: elevation

Table 2.2: Definition of beach characteristic.

Coast	Shoreline	Dune Toe	Beach Width	Beach Volume	Reference
Aquitaine	MSL (E = 0.5)	E = 10	MHW to Dune toe	MSL to Dune top	(Nicolae Lerma et al., 2022)
Duck	MSL (E = 0)	E = 2.5	MSL to Dune toe	Doc to Dune toe	(Zhang & Larson, 2021)
Jarkus	MSL (E = 0)	E = 3	MSL to Dune toe	MSL to Dune toe	(Spanhoff et al., 2003)
Hasaki	-	-	MSL to Dune toe	-	(Kuriyama, 2002)
Narrabeen	MSL (E = 0)	E = 3	MSL to Dune toe	MSL to Dune toe	(Turner et al., 2016)

2.1.1. NASA

The NASA Sea Level Evaluation and Assessment Tool, provides two types of sea level observation, the tidal gauge and satellite altimeter, with the measurement duration from 1993 to 2018 (Harvey et al., 2020). The satellite altimetry measures the absolute sea level variations with respect to the land station in the geocentric reference frame, and the observations from the tidal gauge include the effect of ground motions.

In the sea level rise impact management, the rise-associated coastal morphology should take the vertical land movements (VLMs) into account since it is of direct impact on the coastal vicinity (Cazenave & Cozannet, 2014). These VLMs encompass tectonic and volcanic active activities, natural sediment loading, anthropogenic intervention, and glacial isostatic adjustment (GIA) (Cazenave & Cozannet, 2014). Hence, all the sea level variation data used in the research includes the VLMs. Figure 2.3 shows the rising rate of individual site-corresponding tidal stations used in this research (Harvey et al., 2020) and global mean sea level (GMSL) (Beckley et al., 2017). VLM was not corrected in both raw datasets, while annual and semi-annual signals were removed in the latter one. The rising trends show evidence of rising sea levels and demonstrate worldwide regional variability.

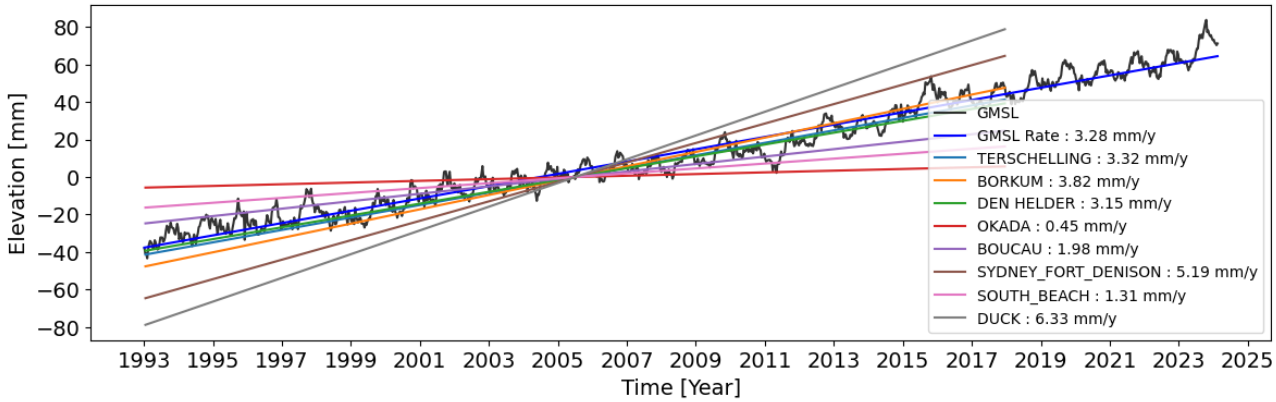

Figure 2.3: Global and Regional Sea Level Rise

2.1.2. Aquitaine

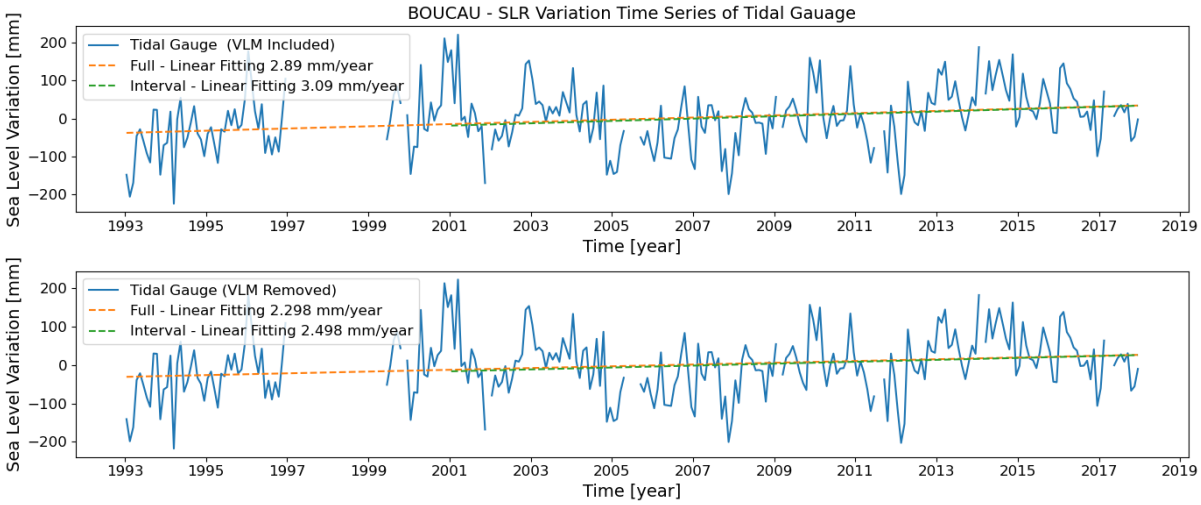

Figure 2.4: Boucau Station - The Sea level signal in the upper figure includes the vertical land motion and is removed in the lower figure.

The Aquitaine coast is located in southwestern France with approximately 230 kilometres of sandy beach extending from the Gironde estuary in the north to the Adour Estuary in the south (Nicolae Lerma et al., 2022). Under the auspices of Observatoire de la Côte Aquitaine (OCA), surveys of the foredune system have been conducted since 2008 with the measuring range in cross-section direction from the lee side of the dune to the proximity position of mean sea level (waterline), shown in Figure 2.5. Surveys were mainly measured with a centimetric GNSS in yearly temporal resolution. The Aquitaine coast was classified into 6 subsegments, indicating the prevailing direction and magnitude of alongshore sediment transport. In view of the more stable decadal coastline evolution mentioned in (Nicolae Lerma et al., 2022), profiles L9, L10, and L11 in Landes Coast (Segment 5.2) were assumed to be regional invariant in profile evolution. Figure 2.6 illustrates some absences in extracting the coastal indicators from these profiles since some measurements did not extend into the submerged area. To compensate for these discontinuities, the time series of extracted coastal indicators were averaged over three profiles and subsequently debiased to remove the average value. At Aquitaine, the calculation of the beach volume is based on (Nicolae Lerma et al., 2022), ranging from the elevation of mean sea level (MSL) (e = 0.5) to the dune top (e = 10). The borders of the beach width are mean high water (MHW) (e = 2) to dune foot (e = 6), shown in Tabel 2.2.

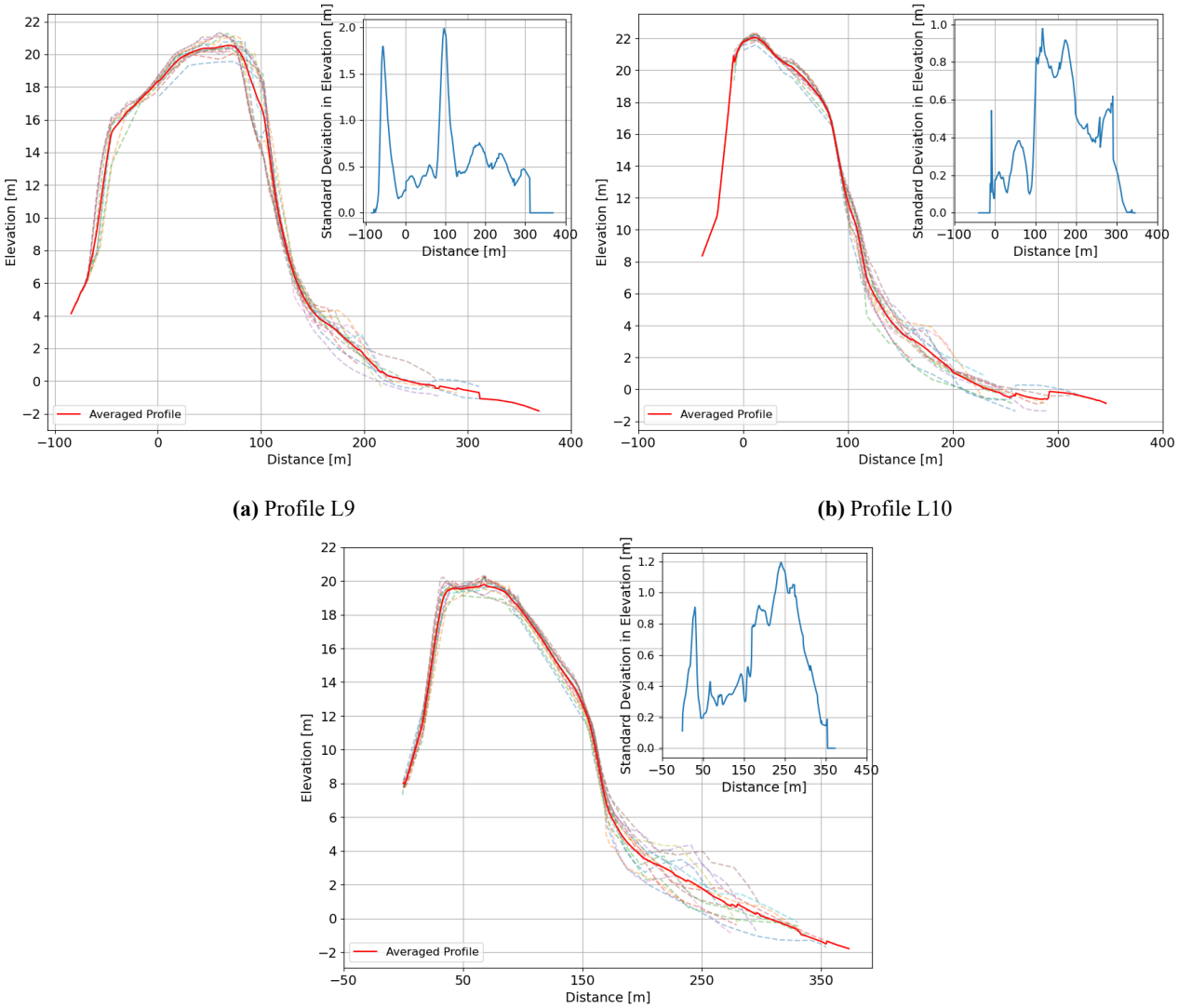

(a) Profile L9

(b) Profile L10

(c) Profile L11

Figure 2.5: The three surveyed cross-sections behaved in a similar morphological variation and were chosen as the research scope.

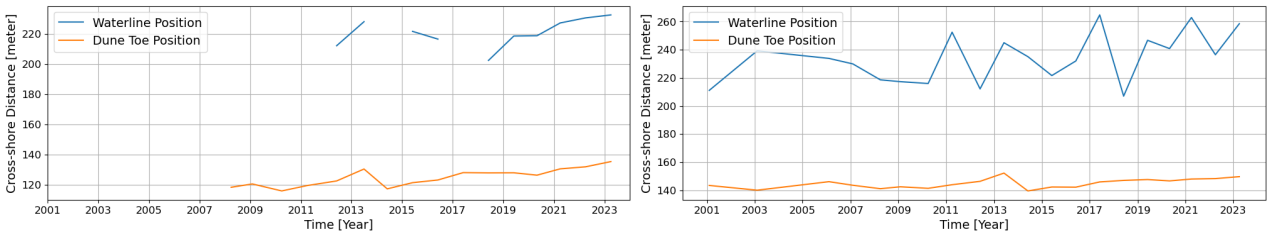

(a) Without averaged over three cross-section profiles

(b) Averaged over L9, L10, and L11 cross-section profiles

Figure 2.6: Yearly measurement of extracted waterline and dune toe position. (seaward positive). Some measurements were extended into the targeting submerged area, resulting in discontinuities.

2.1.3. Duck

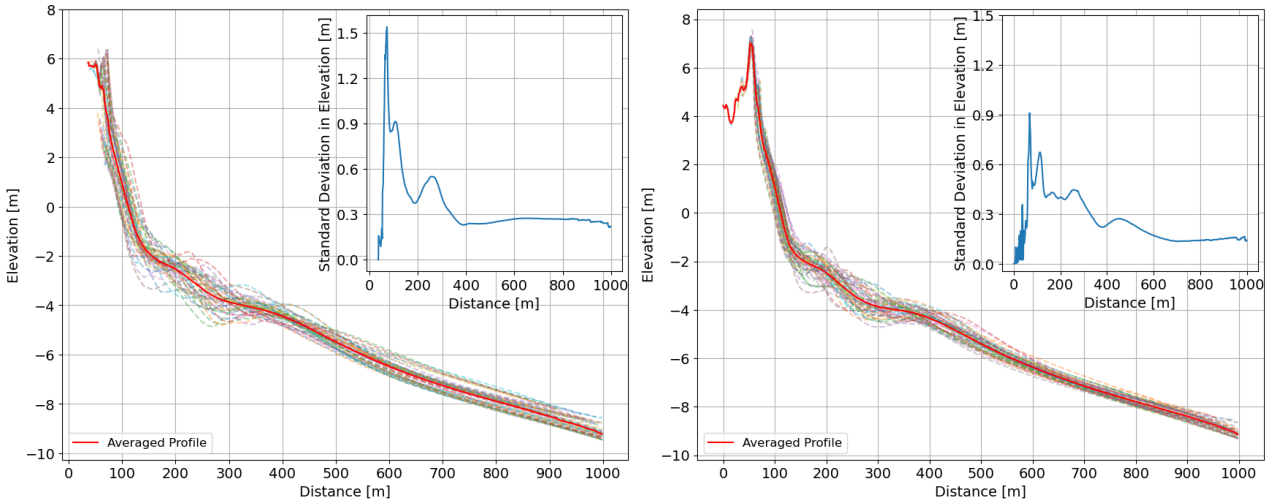

(a) Profile Number 1097

(b) Profile Number -91

Figure 2.7: Two different surveyed cross-section lines at the north of FRF.

The Duck dataset was obtained from the Field Research Facility (FRF), constructed at Duck, North Carolina by the US Army Corps of Engineers in 1977. The FRF possess a 560-meter-long research pier, whose main tasks were to measure nearshore hydrodynamics and storm conditions. The topography surveys include 28 lines, extending from 600 meters south of the FRF research pier to 600 meters north. These surveys are usually measured monthly; in some special situations (e.g. post-storm), the surveying frequency and coverage are higher. Four specific lines were measured approximately biweekly from 1981 to nowadays (43 years), providing the most cross-shore profile data (Zhang & Larson, 2021) (Profile Number 1097, 1006, 1, and -97). Two researching coastal profiles are utilized, located respectively north (Number 1097) and south of(Number -91) the pier.

Figure 2.7 shows the annual evolution of profiles Number 1097 and Number -91. There are two significant peaks on the shore area, one near the waterline (0 meters in elevation) and the other near the foredune (4 meters in elevation), showing an abrupt morphological change in subaerial areas. The location of the depth of closure (DOC) can be found from the sudden drop in the standard deviation value at approximately 400 meters offshore in Profile 1097, and 600 meters offshore in Profile -91. Figure 2.8 depicts the raw signal of the waterline and dune toe position.

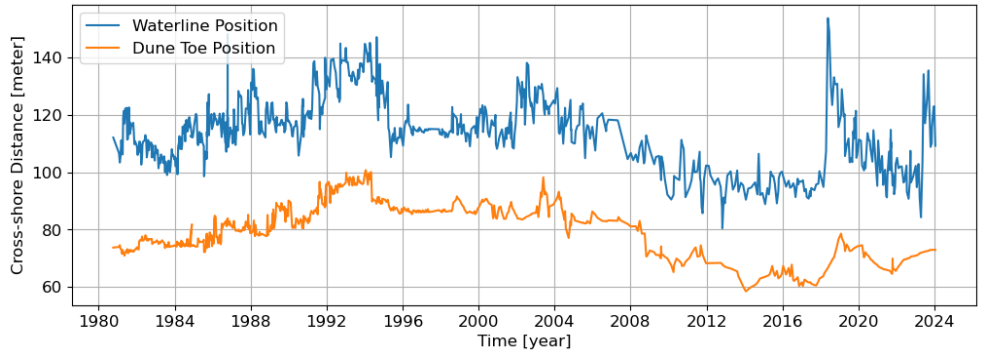

Figure 2.8: Time series of overlooking beach layout of Profile 1097 at FRF (seaward positive).

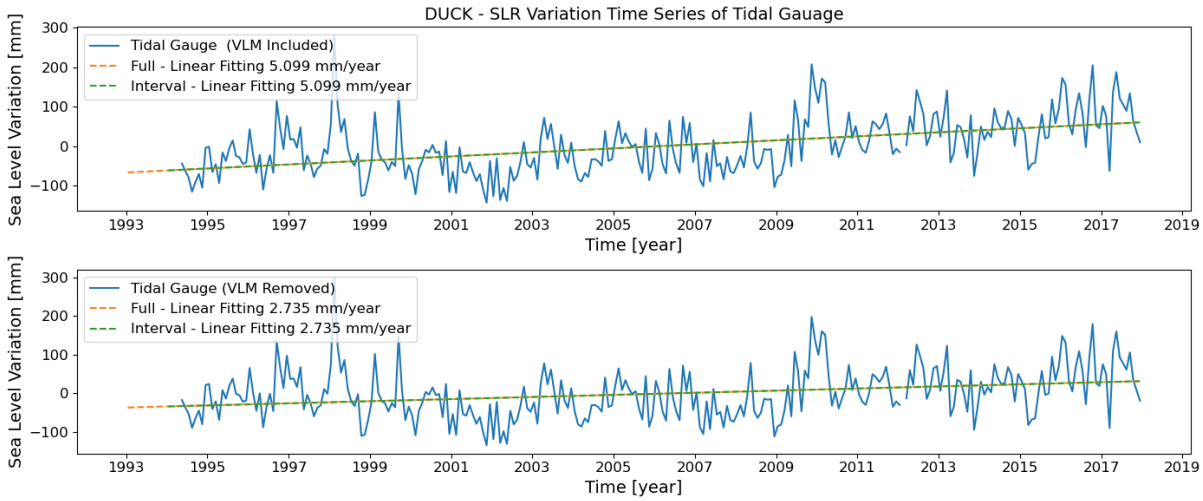

Figure 2.9: Duck Station - The Sea level signal in the upper figure includes the vertical land motion and is removed in the lower figure.

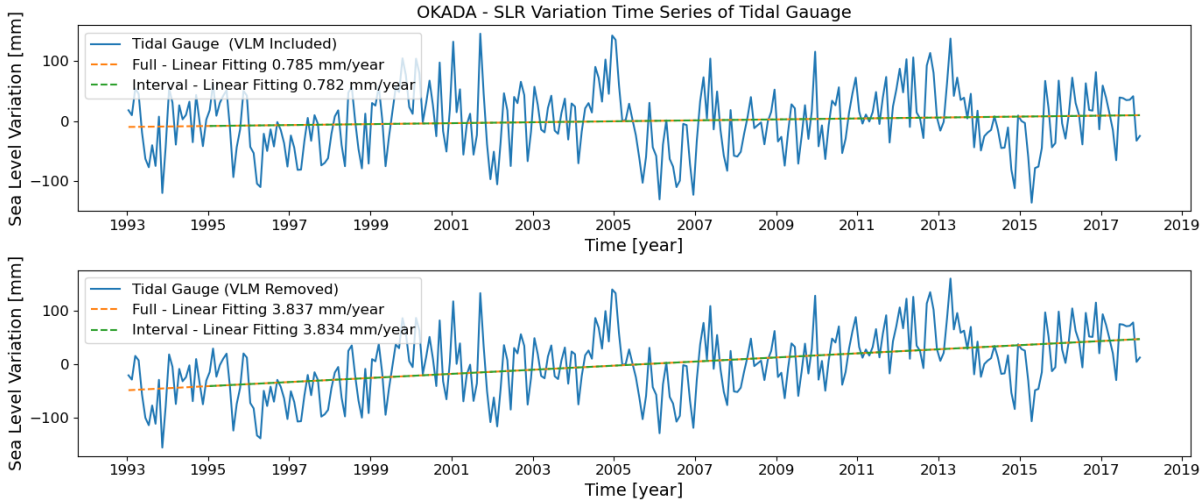

Figure 2.10: OKADA Station - The Sea level signal in the upper figure includes the vertical land motion and removes it in the lower figure.

2.1.4. Hasaki

By deploying the linear fitting on the raw tidal gauge data, Figure 2.10 shows that the vertical land motions counteract the rising sea level by approximately 3 mm/year near Okada station. The difference implies a possible abatement for sea level rise impact; nevertheless, it should be noted that the Okada station is located on Oshima Island rather than in the vicinity of HORS. The spatial deviation between the tidal gauge station and the research coast may misevaluate the realistic influence of the sea level rise.

Waterline, berm, and dune toe data were obtained from the Hasaki-Oceanographic Research Station (HORS), a field data measurement station formed by the Port and Harbour Technical Research Institute, Ministry of Transport (Dastgheib et al., 2022). A 427-meter-long pier was constructed at the HORS, where the reference point of the coordinates of the beach layout (Figure 2.11) is located near the entrance (Kuriyama, 2002). The period of collected measurements spanned 1995 to 2017 (22 years) with the nearly daily temporal resolution (Kuriyama, 2002). The signals can therefore capture short-term morphological activities properly. However, the raw data contains only the time series of the specific location of these three coastal indicators, to validate the results after deploying the methodology from other cross-section profiles is impossible, either to calculate the beach volume. Figure 2.11 depicts raw signals of three beach characteristics. For a proper comparison with other coastal sites, only the waterline and dune toe position will be used in this research.

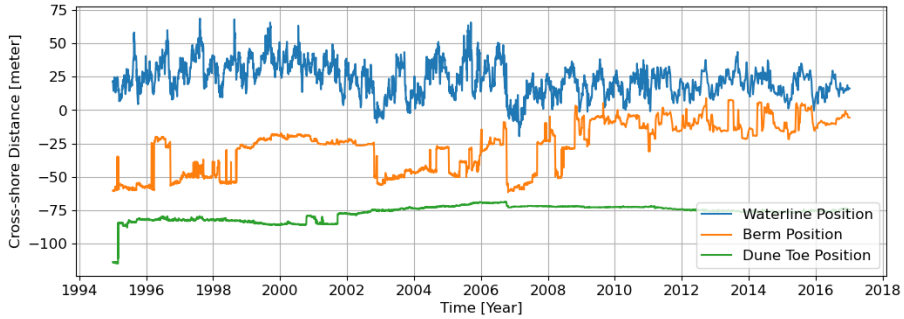

Figure 2.11: The raw time series of overlooking beach layout at HORS.

2.1.5. Jarkus

The JAaRlijkse KUStmeting (JARKUS) datasets have measured the dune-beach-shoreface profiles yearly since 1965, providing the largest database in the world for nearshore morphological development. The primary purpose is to inspect the position of the momentary coastline and provide the reference for beach nourishment against structural loss of alongshore current on the Dutch Coast (Do, Anh TK et al., 2019; Bosboom & Stive, 2021). The range can be grouped into 16 regions, covering the Dutch North Sea coast from North to South. Among these regions, three main coasts can be recognized from north to south: the Wadden coast, Holland coast, and Delta coast (van IJzendoorn et al., 2021). In corresponding to the previously founded coastal progradation phenomenon at the Holland Coast and Delta Coast, and following the logic for alleviating ambient sediment transport influence (the existing beach nourishment), two study sites were selected. The Noordwijk coast at the South Holland Coast and Egmond coast at the North Holland Coast. The corresponding profile in Jarkus indices are 8007100-8007250 for Noordwijk, and 7004150-7004350 for Egmond. The developed JARKUS Analysis Toolbox (van IJzendoorn et al., 2021) was utilized to derive the beach characteristics. Coastal indicators were extracted from these transactions in the JARKUS Analysis Toolbox and averaged intra-sites to interpolate the data discontinuity.

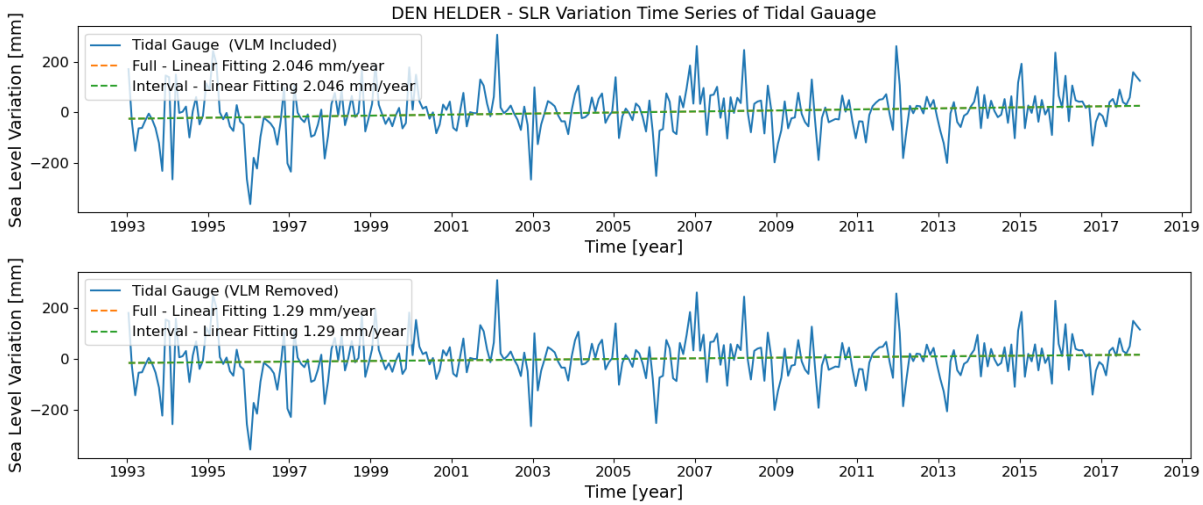

Figure 2.12: Den Helder Station - The Sea level signal in the upper figure includes the vertical land motion and is removed in the lower figure.

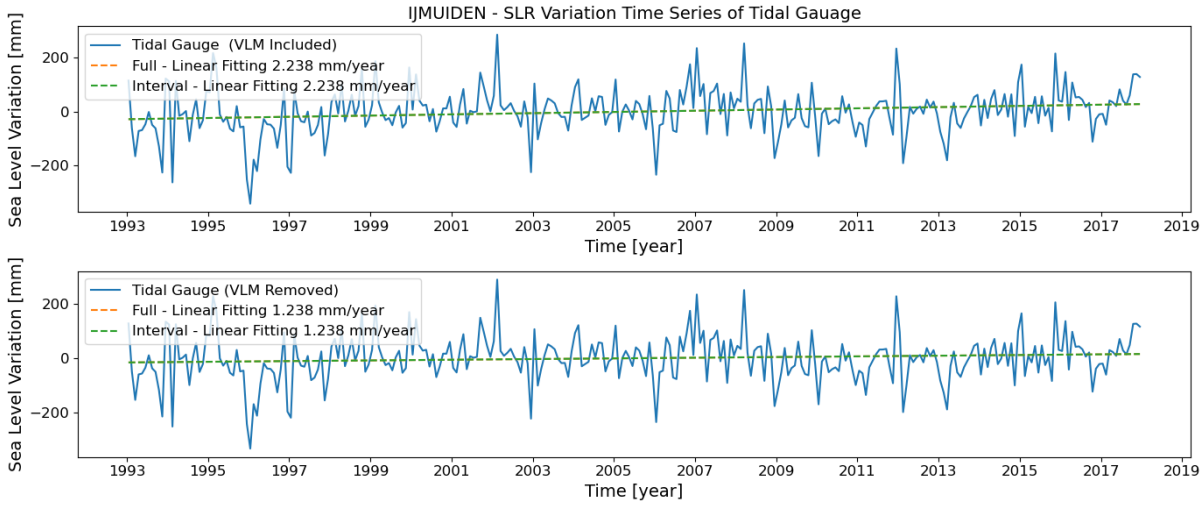

Figure 2.13: Ijmuden Station - The Sea level signal in the upper figure includes the vertical land motion and is removed in the lower figure.

2.1.6. Narrabeen

The Narrabeen-Collaroy is a 3.6 km-long sandy beach embayment located on Sydney's Northern Beaches in southeast Australia. The embayment can be classified into the northern part (Narrabeen coast) and the southern part (Collaroy coast). Under the management of the Water Research Laboratory, UNSW, coastal profiles were measured monthly since 1976. These measured profiles separate uniformly, ranging from the Narrabeen coast to the Collaroy coast. Following the beach characteristic definition in (Turner et al., 2016), in this research, the mean sea level table is defined as the land-water interface at 0 m AHD (Australian height datum).

Turner et al. (2016) indicate that the natural evolution of the coastal dune system at the southern end of the embayment has been intervened by urban development. The foredune has been impinged on, with the remaining dune height at 3-4 meters, shown in Figure 2.14. In contrast, the coastal profiles were less-intervened at the Narrabeen beach. Therefore, PF1 is selected as the research profile to reduce the anthropogenic effects on coastal profile evolution.

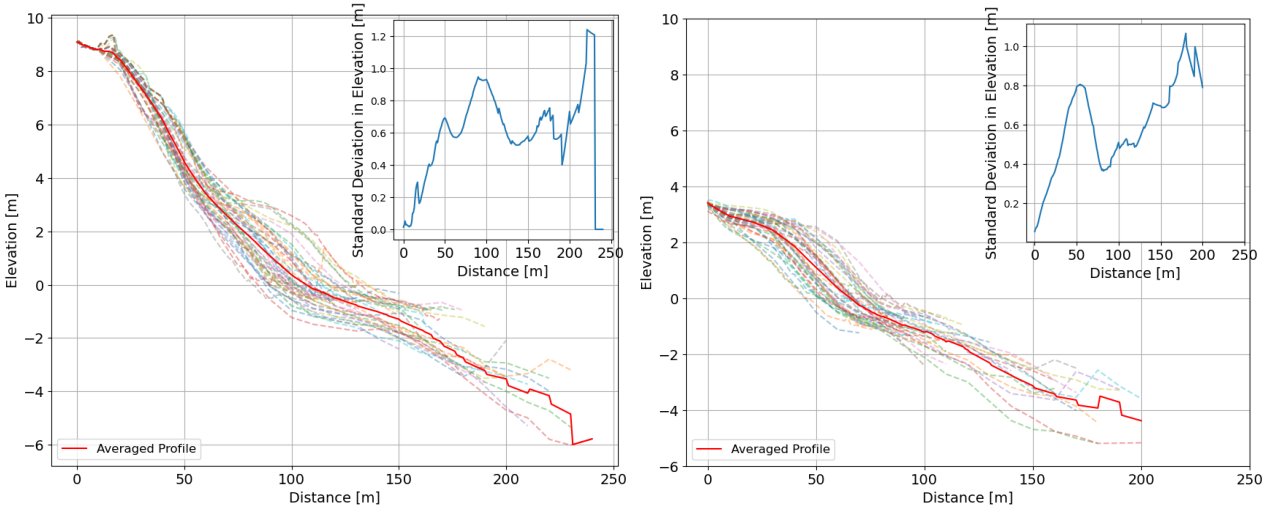

(a) PF1 Profile **(b)** PF8 Profile

Figure 2.14: Annual Evolution of two Narrabeen beach profiles at the edge of the north (PF1) and the south (PF8) embayment.

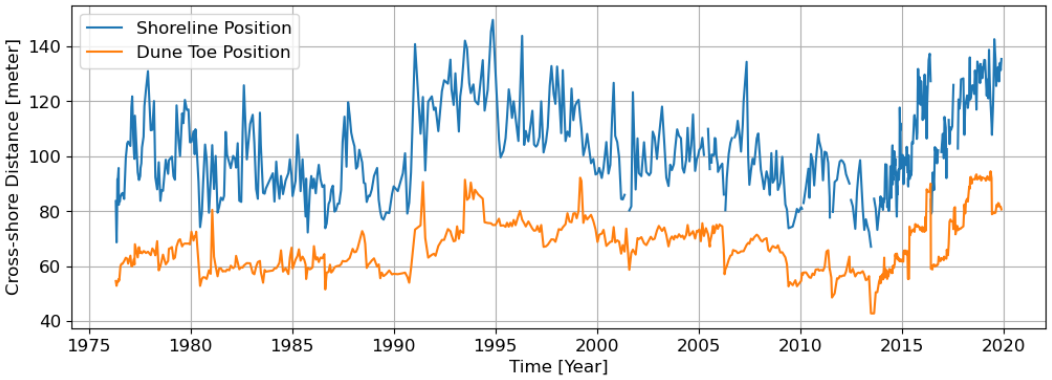

Figure 2.15: The raw time series of overlooking beach layout at Narrabeen PF1 Profile

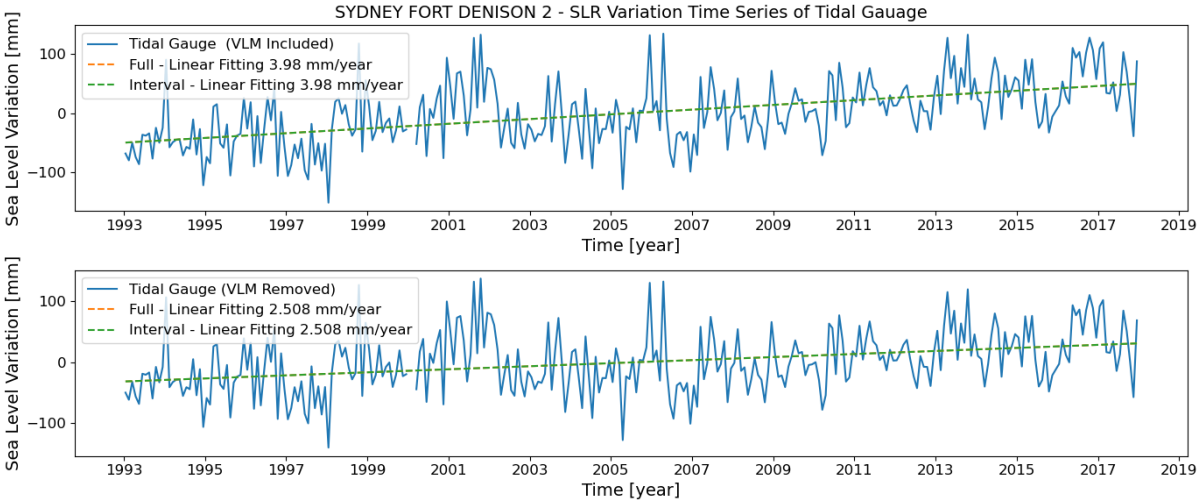

Figure 2.16: Sydney Fort Denison Station - The Sea level signal in the upper figure includes the vertical land motion and is removed in the lower figure.

2.2. Coastal Characteristic

This section will propose the motivation for selecting specific beach characteristics as the coastal indicators to study the evolution of beach morphology. The indicators, shoreline position and dune toe position were utilized to reflect the research site's transgressive or regressive coastal system. The evolution of beach width reveals the conformity of ideal coastal adaption to rising sea levels. Since the sea surface variation is the only collected hydrological data in this research, calculating the sediment transport for each coastal site is difficult. Hence, the final indicator utilized is the foreshore sediment volume, which provides the sediment budget within the coastal area.

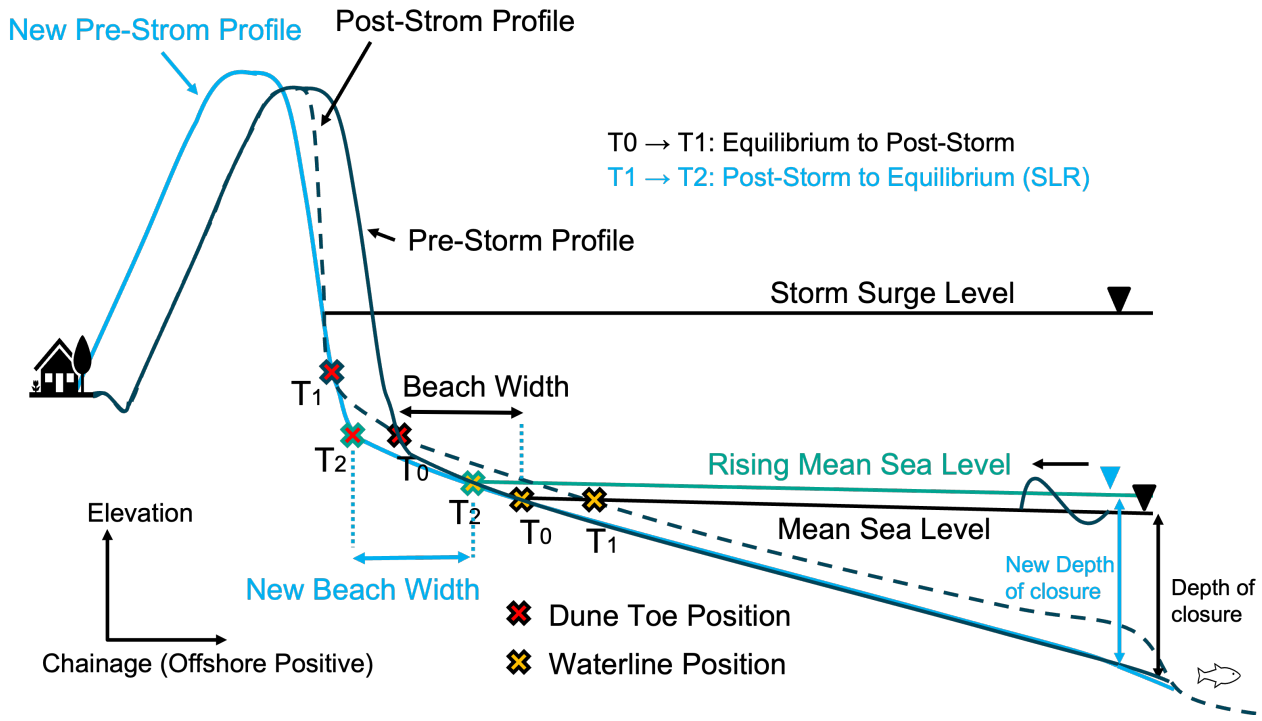

Figure 2.17: Schematisation of beach cross-section profile. T0 is the pre-storm condition and T1 is the post-storm condition before the regional sea level rise. T2 is the pre-storm condition after the sea level rise. The new equilibrium profile was not depicted for clear illustration in the plot.

2.2.1. Shoreline Position

In contemporary coastal management, the response to sea level rise is based on the well-accepted concept that an increased elevation in sea level will result in a shoreline recession. The rising sea level causes the shoreline to migrate landward due to permanent inundation of terrestrial land (FitzGerald et al., 2008). The superimposition of land subsidence and sediment reduction also augmented the shoreline retreating magnitude (Uehara et al., 2010; Kiguchi et al., 2021). Whereas, acting as the possible countering effects to accelerating sea level rise, the sediment supply amount and vertical motions can be dominated in controlling transgression versus regression, illustrated in Figure 2.18. Exerting the direct hydrodynamic forces, the shoreline position directly reflects the involved sophisticated environmental factors. The direct interactions of shoreline position and the sea level height propose it as the front-edge indicator in evaluating the response to rising sea level impact (Cazenave & Cozannet, 2014; Dastgheib et al., 2022; Vitousek et al., 2017; Dean & Houston, 2016).

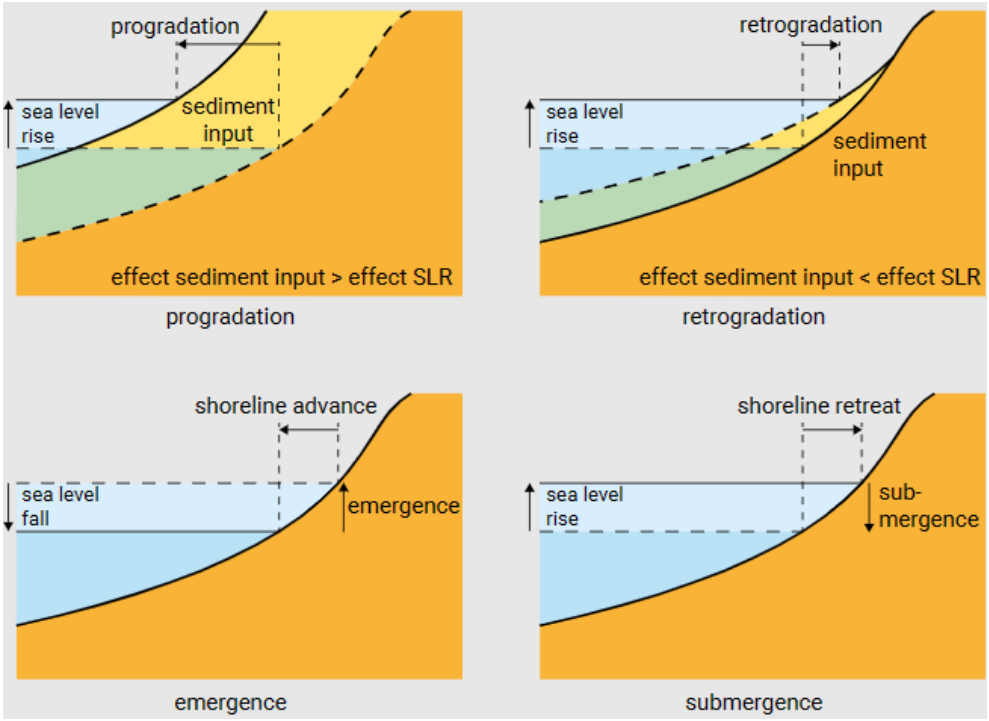

Figure 2.18: Classification of interaction between sea level rise and sediment supply. This figure is derived from (Bosboom & Stive, 2021).

2.2.2. Dune Toe Position

Another good nomination for assessing the influence of sea level rise is the coastal dunes, which provide the importance of coastal protection, storm surge defence, salt intrusion defence etc. Under the stress of sea level rise, it is predicted that this long-term effect causes increased erosion rates and eventually deconstruction of the dune system (FitzGerald et al., 2008). With the rising water table, there is a higher probability that waves can penetrate into inland areas. Exposure of the dune foot to energetic wave action is considered a key damage factor in dune retreat (Masselink et al., 2022). Nevertheless, the impact of sea level rise on coastal dunes is still uncertain. van IJzendoorn et al. (2021); Burvingt and Castelle (2023) indicated a progradation dune system with a dune system development rate larger than the sea level rising rate. This opposite phenomenon may be attributed to the local dominance of the geomorphological transport mechanisms, leading to the ambiguous realisation of in-situ dune system reactions to sea level rise impact. This bestows motivation regarding the dune toe as the research characteristic.

2.2.3. Beach Width and Volume

Adhering to the dynamic equilibrium and profile adaption, the natural beach width should behave relatively stable in progradation and recession conditions. The dynamic equilibrium system bestows the upper shoreface to recovery from the perturbation, where the adjusting timescale depends on the magnitude of the existing disruption and water depth (Bosboom & Stive, 2021). Likewise, the dune system responds to the episodic environmental forcing in the dynamic equilibrium system, even though a longer recovery timescale is required (Houser et al., 2015; Burvingt & Castelle, 2023). After exerting the instantaneous, seasonal, or episodic ambient forces onto the coastal profile, sediments merely redistribute between the subaerial area and active zone and the total amount remains unchanged. The ideal rising sea level affecting beach width can be regarded unchanged under the longer engineering timescales (a few decades) (Idier et al., 2019; Woodworth et al., 2019). It is well-adopted as an engineering assumption that profiles will slowly migrate landward with a con-

stant cross-section profile shape (Bruun, 1962; Dean & Houston, 2016; Bosboom & Stive, 2021) as shown in Figure 2.17.

The dynamic equilibrium is subjected to no structural losses or gains in the coastal regime, in which the longshore current gradient and aeolian transport may play a significant role and violate the presumption. In many two-dimensional vertical (2DV) cross-section studies, the contribution of alongshore transport to gross sediment transport amount is especially quantified and elaborated (Houser et al., 2015; Harley et al., 2022; Suanez et al., 2023; Casamayor et al., 2022). In reality, the structural losses or accretions encompass the long-term trend-involved activities, including sea level rise, longstanding wave-induced sediment transport, alongshore drift, tidal inlet trapping, river outflow etc. Separating and quantifying these mechanisms then becomes subtle and sophisticated. Hence a proper alternative approach in this research to quantify the sediment conservation via the long-term coastal volume which pertains to structural sediment erosion/accretion.

The discrete beach profile surveying instigates the numerical integration over a certain cross-shore distance for computing beach volume. Equation 2.1 shows a commonly adopted Simpson's numerical integration 1/3 rule. In the equation, a and b are the landward and seaward boundaries respectively which depend on the site-specific beach foreshore characteristics. Hereby, the standard deviation in elevation as a function of the average profile for available coastal sites was computed. The corresponding offshore coordinate for depth of closure can therefore be pinpointed at where a sudden drop of standard deviation values occurs in the submerged area. The landward boundary is defined at the proximity of the dune toe pragmatically.

The other type of shoreline response is related to the short period and natural variability of hydrodynamic conditions in the coastal zone. These phenomena can be seasonal fluctuation or inter-annual, being contingent on the hydrometeorological magnitude. In the next section, two data-driven models will be proposed to remove the high-frequency mechanisms and acquire long-term behaviour in the time series.

$$\int_a^b f(x)\,dx \approx \frac{b-a}{6}\left(f(a) + 4f(\frac{a+b}{2}) + f(b)\right) \tag{2.1}$$

2.3. Spectral Analysis

In this section, two statistical models will be proposed to capture the long-term behaviour of the signal and meanwhile eliminate the embedded high-frequency mechanisms. The first approach is the Inverse Fourier Filter Transform Model, which filters out all the high-frequency Fourier series in the signal to get a pure low trend. The second approach is the Singular Spectrum Analysis Model, which implements the singular value decomposition techniques to decompose the initial signal into several eigenvectors. From these eigenvectors, multiple eigenmodes describing the characteristics of the raw signal will be derived.

2.3.1. Inverse Fourier Filter Transform Model

The signal processing in the Inverse Fourier Filter Transform (IFFT) Model can be separated into two stages, including the frequency perception and the signal removal. The first step is to utilize the power spectrum to discover the implicit constituted events in the signal. The second step is to get rid of the unwanted unnecessary signal by employing the inverse Fast Fourier transform.

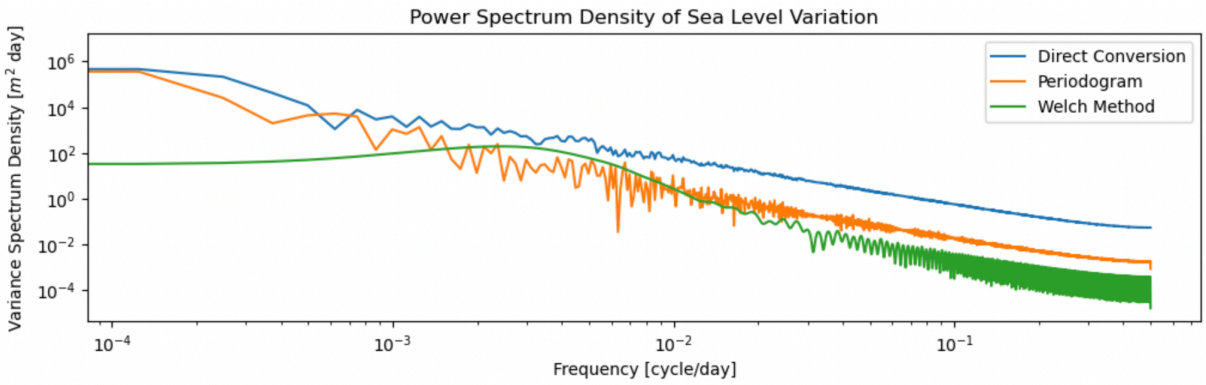

Figure 2.19: Power spectrum density results of Direct Conversion, Periodogram, and Welch's method. Welch's method provides a smoother spectrum result by averaging over multiple converted spectra.

The next step in the IFFT Model is to implement the inverse fast Fourier transform to filter out partial Fourier series in the raw signal. The raw signal is considered as the combination of massive Fourier series, which contains all the low-frequency and high-frequency mechanisms. Based on the detected rhymical events from the power spectrum density, the specific frequencies are selected as the cut-off year. The inverse fast Fourier transform is subsequently used to remove all the series in which the frequencies are larger than the specified cut-off year. Figure 2.20 demonstrates the reconstructed signals by applying different filters. Suppose that a 5-year event is detected by the spectrum, all the events that the periods are smaller than 5 years were eliminated, forming a reconstructed signal.

2.3.2. Singular Spectrum Analysis

Singular spectrum analysis (SSA) is a nonparametric statistical technique, which decomposes the time series into various components. It aims to decompose the original signal series into a sum of subset components, including trends, oscillations, periodic signals, and noise. The SSA can be regarded as the lower dimension of principle component analysis (PCA) which is also called empirical orthogonal function in the meteorology field (Hannachi et al., 2007). As the lower dimension of EOF, the SSA only looks into one dimension (the specified location) of the morphological variation, namely the time series of a single indicator. The theory of SSA is based on two steps, the decomposition and reconstruction of time series (Nina Golyandina, 2013). The decomposition process is to

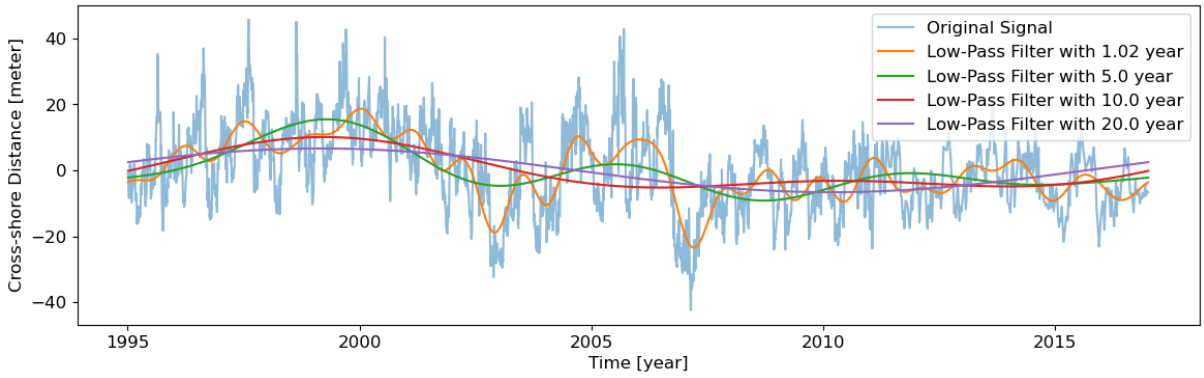

Figure 2.20: Demonstration of the inverse Fourier filter transform model. The large-year filter would smear out the linear trend or the offset events.

separate the original time series into several sub-vectors, then do the singular value decomposition to find the eigenvalue of corresponding eigenvectors. This separates the original time series into temporal eigenvector and spatial eigenvector, shown as Equation 7.4. The variable U is the spatial-related eigenvector and the variable V is the temporal-related eigenvector.

$$\mathbf{X_i} = \sqrt{\lambda_i} U_i V_i^T \tag{2.2}$$

In the reconstructed step, these eigenvectors will be superimposed by the researcher-specified combinations, which hereby the terminology "eigenmode" is utilized to describe these combinations. Usually, the first eigenmode is considered as the smoothed trend, representing the long-term behaviour of the raw signal. A detailed introduction to singular spectrum analysis is in the Appendix. In SSA, selecting a suitable window size is very important for determining the decomposed eigenvalues in the signal decomposition process. In general, the window size is bounded in the interval $2 \leq \mathrm{L} \leq \mathrm{N}/2$. L is the window size. The larger the L, the more pure the time series component (trend, oscillations, periodic signals, and noise) will be decomposed (Zhang & Larson, 2021; Nina Golyandina, 2013), subsequently providing a strong separation concerning the small perturbation. Nevertheless, a too-large window size can over-separate the signal of interest and mix up with other eigenmodes. For instance, the "correct" sea level rising trend is over-divided into a linear line and other periodic signals.

2.4. Cross-correlation Analysis

To study the relationship between two phenomena, the most straightforward technique is the correlation research. From the signal-processing perspective, the cross-correlation is to measure the similarity of two signals as the function of the displacement of each other. Analogized to the principle of convolution, the most positively/negatively similar pattern at certain displacement can be found by continuously shifting the data points. These two vectors will be shifted one data point each time, and do the inner product data point by data point. Hence, the signal cross-correlation is also known as dot sliding product. Equation 2.3 and Equation 2.4 are the definitions of signal cross-correlation (Bracewell et al., 1965) in the continuous and discrete functions respectively. The functions (t) and (t) are two distinct time series where the overbar symbol represents the complex conjugate of the function. The τ denotes the displacement between two functions. To discretise the equation for signals calculation, $f(t)$ and $g(t)$ can be rewritten into x and y, where k is the displacement, and N is the total number of measurements. To remove the deviation caused by the outliers in the signal, cross-correlation results can be normalized between the interval $[-1, 1]$, and simultaneously be dimensionless, as shown in Equation 2.5.

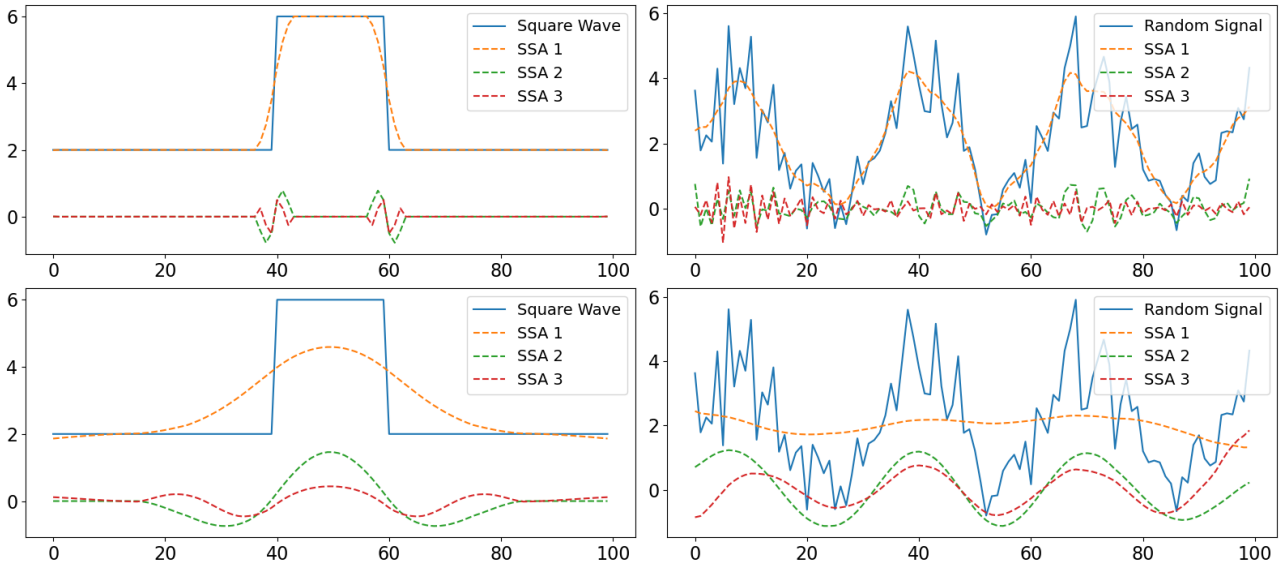

Figure 2.21: Two toy datasets were decomposed into three eigenmodes by singular spectrum analysis. The applied window size L in the upper figures is N/25 = 4 data points, which simulates the detail of the trend. The window size in the lower figure is N/4 = 25 data points, which better separates the raw signal into various components.

$$z = (f * g)(\tau) = \int_{\infty}^{-\infty} \overline{f(t)} g(t+\tau) dt \tag{2.3}$$

$$z(k) = (x * y)() = \sum_{l=0}^{\|x\|-1} x_l^* y_{l-k+N-1} \tag{2.4}$$

$$z(k)_{norm} = \frac{z(k)}{\sqrt{\sum_{n=0}^{N-1} {x_n}^2 \sum_{n=0}^{N-1} {y_n}^2}} \tag{2.5}$$

Given the perspective that the relationship between two time series is a function of lags, the causality between sea level rise and coastal morphological change should be noticed. Assume that the effect of sea level variation on the beach profile is more prominent whereas the opposite interaction can be negligible. Only the negative lags of the correlation outcomes will be discussed, indicating that the sea level variations cause the morphological responses but not vice versa. The other factor required to be considered is the time-lagging effect. Sometimes, climate change-induced impact on nature is not only indistinct but retarded, especially when concerning the biological communities and habitats. From an ecological aspect, this influence will wreak irreversible harm when the accumulative damage exceeds the environment's carrying capacity (Zhao et al., 2020). A certain amount of time is necessary to reveal the consequences. This implies that there is an existing lagging effect within the response of ecology to climate change. A similar perspective occurs in coastal areas where a former upland is converted into coastal wetlands due to inundation. The establishment of these converted coastal wetland vegetation is assumed to be associated with a response lag of five years (Schuerch et al., 2018; Wu et al., 2017). By analogy with this, a reasonable suspicion that there may be a latent lagging effect existing in the coastal geomorphological responses to accelerating sea level is raised. Will the coast slowly adapt and show the evidence after a couple of years? This lagging effect will be introduced by shifting the time series sequences while comparing the coastal indicators' signals and

sea level signals. The occurrence of lagging effects is somehow contradictory to the conventional concept of shoreline adaption to hydrodynamic forces. The dynamic equilibrium in morphological adjustment in the coastal site can be intra-annual. Yet, the displacement study in the cross-correlation may presumably provide a deductive subtle hindsight.

This chapter will address the IFFT and SSA model deployment onto the three indicators at different coast sites. At first, in the IFFT Model, the Welch method was applied to derive the power spectrum density to reveal the potential seasonal mechanisms within sea level and topographic raw trends. In Welch's method, different window sizes will provide distinct outcomes of the converted spectrum, illustrated in Figure 3.1 (a). Multiple colourful lines in the below figure represent the detected density spectrum from different window sizes. For each employed window size, the first three highest densities (peaks) were detected and marked as 'black', 'blue', and 'red' stars respectively. These peaks are the significant constituted seasonal events within the raw signals, which hereby be regarded as the cut-off filtering signal in the IFFT Model. To eliminate the redundant uncertainty from the detected peak frequency, the number of occurrences of these stars must exceed two while considering them as significant peaks. For a better elaboration, Figure 3.1 (b) shows the entire spectrum results with a log-log plot. The spectrum range is the envelope encompassing the outcomes from different window sizes, revealing the inconsistency of detected results. The significant peaks are depicted on the averaged spectrum, showing the embedded morphological and hydrodynamical mechanisms in each coastal site.

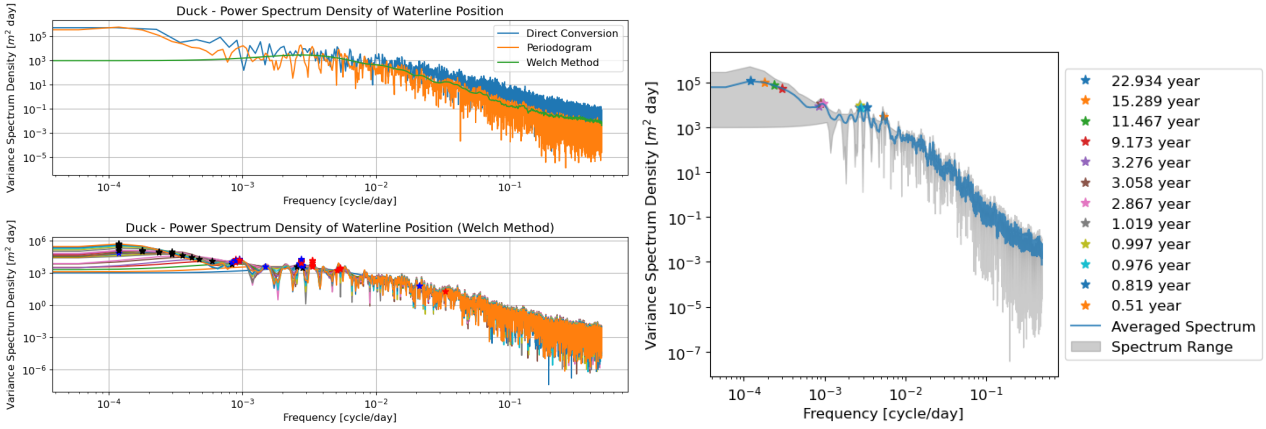

(a) **(b)**

Figure 3.1: (a) The upper figure shows spectrum results from three approaches (periodogram, direct conversion, and Welch's method), where the Welch method is adopted in this research for better performance. The colour lines depicted in the lower figure are derived spectrum by applying different window sizes. (b) Pronounced seasonal mechanisms detected by Welch's method where the occurrence amount of stars in (a) exceeds two. Different year-values represent the seasonality in the

The specific cut-off frequency should be defined in the IFFT Model, yet there is no certain and ubiquitous rule for a site-specific model. Values will vary site by site, adhering to the global physical and geographic differences. This research did not study details of the embedded sediment transport and hydrodynamics in all coastal sites. Instead, five individual low to high cut-off periods were directly adopted from the detected peaks, whose motivations can be ascribed to computation efficiency and physical event-based facts. For instance, Figure 3.2 illustrated the nearly identical reconstructed signals after using 7.64 year-filtering and 22.934 year-filtering, that the frequencies bounded between these boundaries will not be selected. On the contrary, there is an obvious difference in 2.41 year-filtering year. Another advocation here is the imputation of seasonality to possible phenomena, such as the 2.41-year event to ocean dynamics and the 7.64 / 15.29-year events to the sea level rise, global tide, or vertical land motion (Woodworth et al., 2019). The cross-correlation study used the mid-term

temporal scale between 5 to 10 years as the representative reconstructed signal.

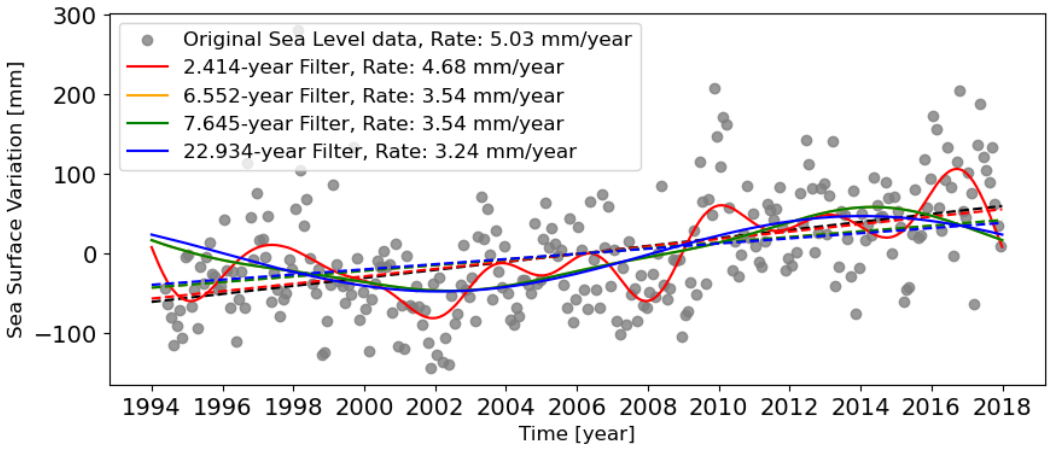

Figure 3.2: Demonstration of filtered signals. Three prominent cut-off years are chosen. The reconstructed signals by using 6.552 and 7.645 cut-off years are overlapped, suggesting the magnitude of this 7.645-year event contributing to the original signal might be weak.

In consistency with the IFFT Model, the singular spectrum analysis implements five different window sizes on each indicator's and sea level signals. As mentioned in Chapter 2.3, the derived eigenmodes from the SSA analysis contain no physical meaning and can not fully remove the high-frequency signals, shown in Figure 3.3. Multiple window sizes are thus computed iteratively to derive the optimal results. The residual trend in Figure 3.3 is the remaining eigenmodes of the original signal subtracted from eigenmode SSA1 (long-term trend). It can be clearly seen that the high-frequency behaviour still exists in the filtered SSA eigenmode.

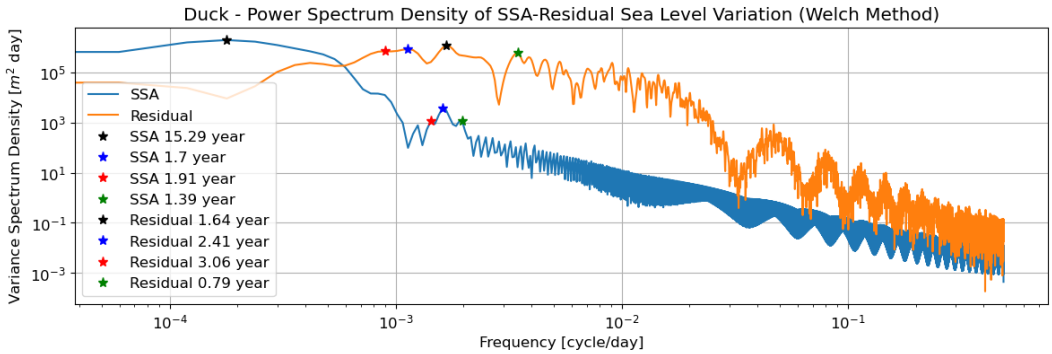

Figure 3.3: Demonstration of remaining high-frequency mechanisms in the SSA results despite a large window size adoption.

3.1. Aquitaine

Figure 3.4 shows the decadal coastal profile evolution of three successive cross-sections. The beach face and backshore area (adhering to the definition by (Nicolae Lerma et al., 2022) in Section 3.1), experienced a relatively dynamic variation in the bounded envelope. The coastal dune systems were stable with no clear coastal profile migrations observed, indicating that the dynamic equilibrium profile stayed put. Qualitatively, no clear coastal migration direction is observed within 15 years of measurement.

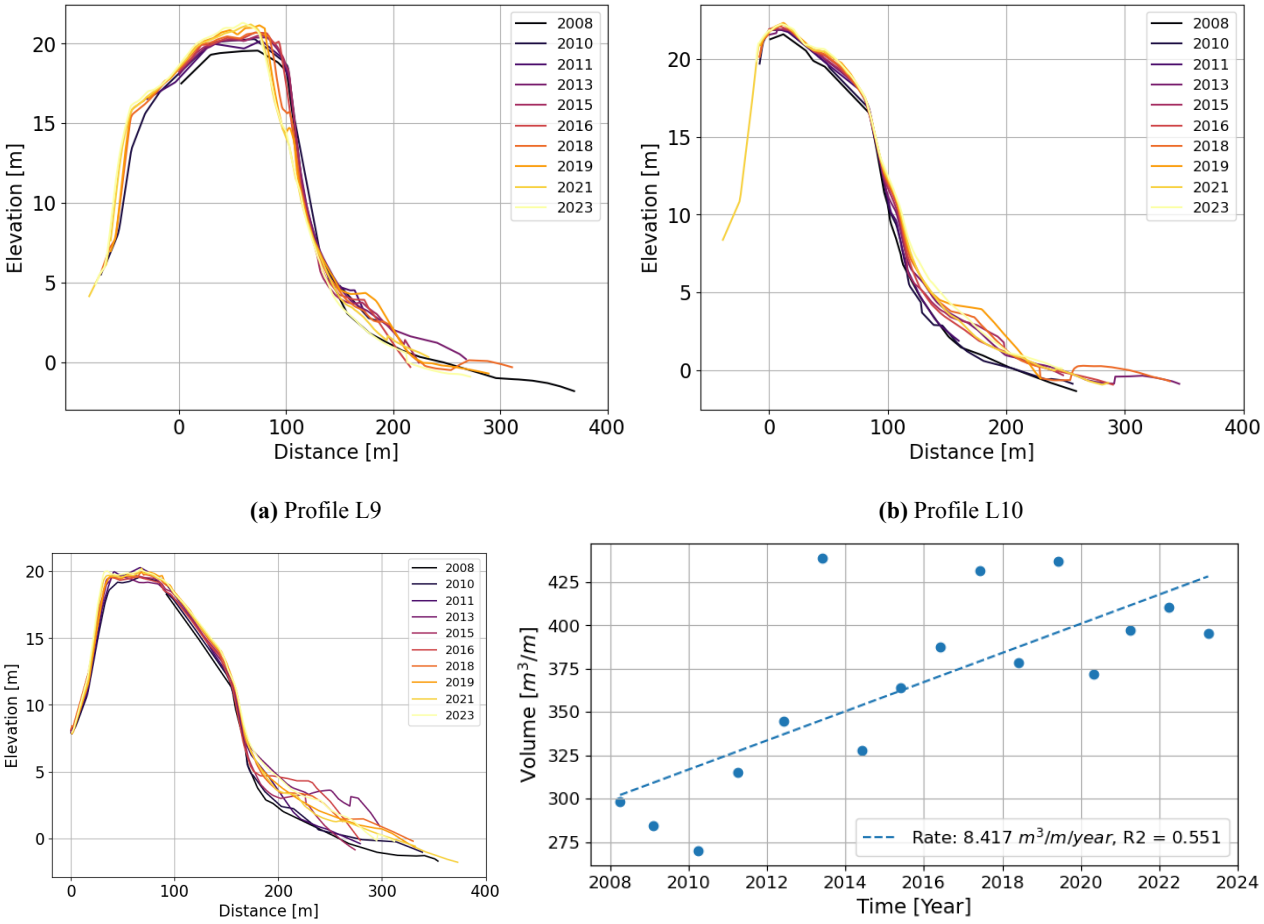

(a) Profile L9

(b) Profile L10

(c) Profile L11

(d) Long-term beach volume development average over three profiles.

Figure 3.4: Aquitaine: Evolution of three cross-section profiles north (Profile L9) and south (Profile L11) to the pier. The colour lines show profile development through time, the measurement duration is divided into 10 segments for clarity display. Beach volume is calculated from the mean sea level to the dune front position

The power spectrum density results present a consistent event-driven relationship between sea level and topographic signals, shown in Figure 3.5. A 7.12-year event and a 3.56-year event are revealed in all PSD outcomes, implying the influence of sea level variation on coastal profile at mid-term and long-term scales. Moreover, there is a 4.27-year event disclosed in sea level, dune toe, and beach width power spectrum, yet not in the shoreline signal. The difference may be ascribed to the non-linear interactions of sea level-induced and additional environment transport-induced. The other detected common periods may attributed to additional morphological transport mechanisms, for instance, the 10.673-year period in both the shoreline position and beach width signal.

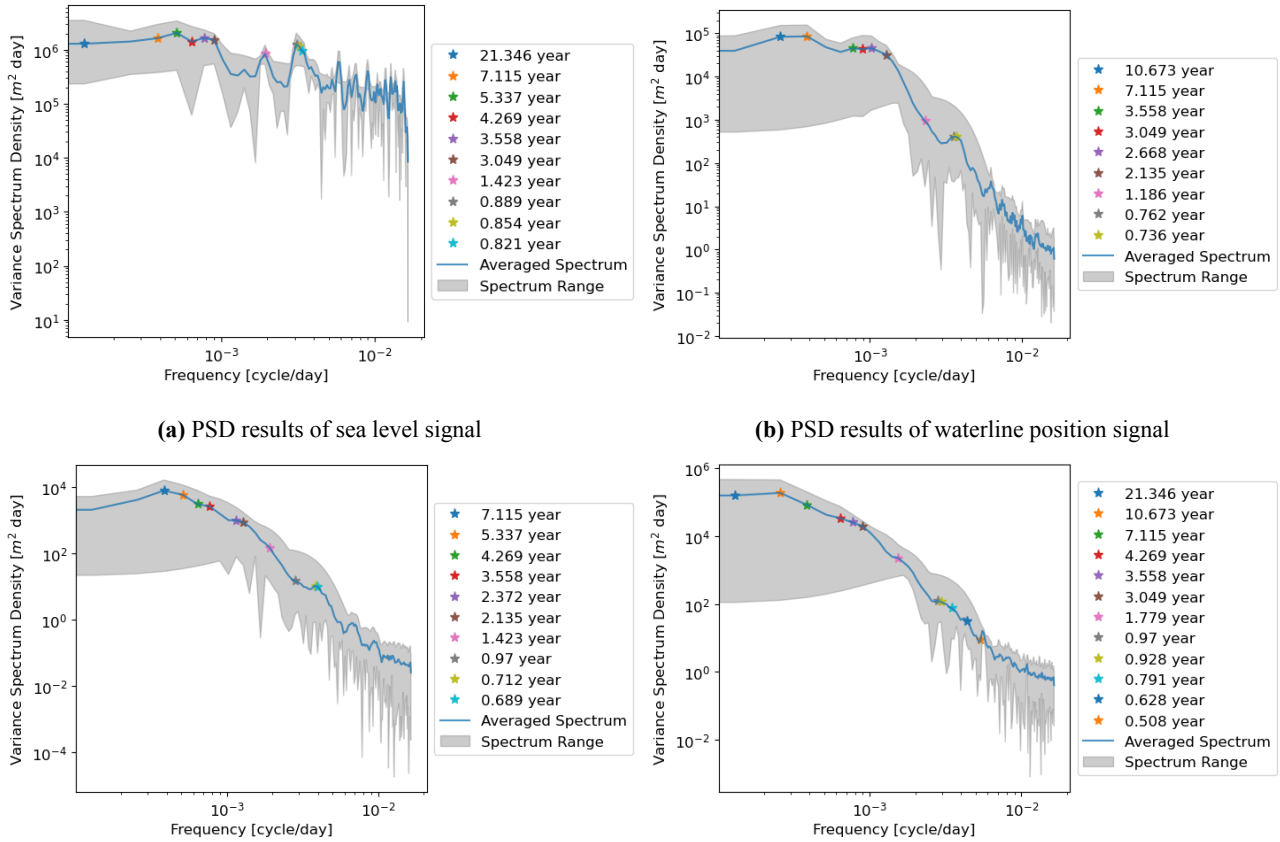

(a) PSD results of sea level signal

(b) PSD results of waterline position signal

(c) PSD results of dune toe position signal

(d) PSD results of beach width signal

Figure 3.5: Aquitaine: Singular spectrum decomposition of sea level and topographic signal for the first eigenmode. N is the total amount of data points where the window size depends on the computation efficiency and high-frequency mechanisms to filter out.

Figure 3.6 presents the reconstructed signal from applying specific cut-off filter. To compare among the results and meanwhile achieve physical interpretation of long-term evolution trend, the 7.115-year is the optimal cut-off filter. Nevertheless, by the calculation of the p-value of the shoreline position changing rate, the value of the 7.12 cut-off filter does not provide a statistical reliance with a minus 0.025 waterline retreating rate. The hypothesis test suggests that there is no evidence to reject the changing rate is zero under the 7.12 cut-off filter. The IFFT Model presents a wide range of shoreline changing rates for all other applied filters. The divergence hinders the proper clarification of real shoreline responses to rising sea levels, yet in general, the moving direction of shoreline position is seaward. As for other indicators' results in the IFFT model, they suggest the seaward dune toe migration with an increasing subaerial beach width.

The SSA model results are shown in Figure 3.7. All the indicators suggest a coastal progradation at the research profile at Aquitaine, yet the computed shoreline position changing rates are still divergent. The long-term changing rate of shoreline position is also zero by implementing the largest window size. By using the window size N/3, The SSA Model result verifies the dissent of result of 7.12-year filter in the Model. Similarly, the SSA Model states that the research coastal site is progradating over the past decade, counteracting against the sea level rise-induced erosion. Table 3.1 provides the long-term changing rate of the sea table and all indicators.

The filtered signals from 7.12-year filter and N/3 window size are adopted as the representative year for all signals in the cross-correlation analysis, despite the dissent shoreline position changing rate. The bootstrap method shows that the results of 7.12-year combinations between oceanic and topo-

graphic data locate outside the 95 percent confidence interval. This suggests distinct analysed results by using this filter. In correspondence with the above-mentioned progradation phenomenon, Figure 3.8 reveals a weak cross-correlation between the shoreline position/dune toe position and the rising sea level at the zero lags. It is then convincing not to refer to a clear relationship between rising sea levels and topographic evolution. In contrast, the positive correlation between sea level and beach width can be interpreted as a pseudo-relation with the simultaneously increasing amount. Accordingly, the results from two data-driven models demonstrates that the coastal site was counteracting sea level rise impact in the long term evolution. The contradiction can presumably be attributed to continuous alongshore sediment transport input, where the total sediment amount increased annually, shown in Figure 3.4d.

Table 3.1: Aquitaine: Linear Fitting results of the SSA and IFFT filtered signal, the cut-off year in IFFT Model is 7.115 year and the window size in SSA Model is N/3. The symbol means that there is no statistical evidence proving the changing rate is non-zero. SL: sea level variation, SP: shoreline position, DP: dune toe position, BW: beach width

Aquitaine	SL (mm/year)	SP (m/year)	DP (m/year)	BW (m/year)	BV ($m^3/m * year$)
IFFT	4.202	-0.025*	0.1	0.51	8.417
Cross-correlation	-	0.267	0.128	0.766	-
SSA	3.46	0.0	0.11	0.82	8.417
Cross-correlation	-	0.043	-0.188	0.798	-

Inverse Fourier Filtering Transform Model

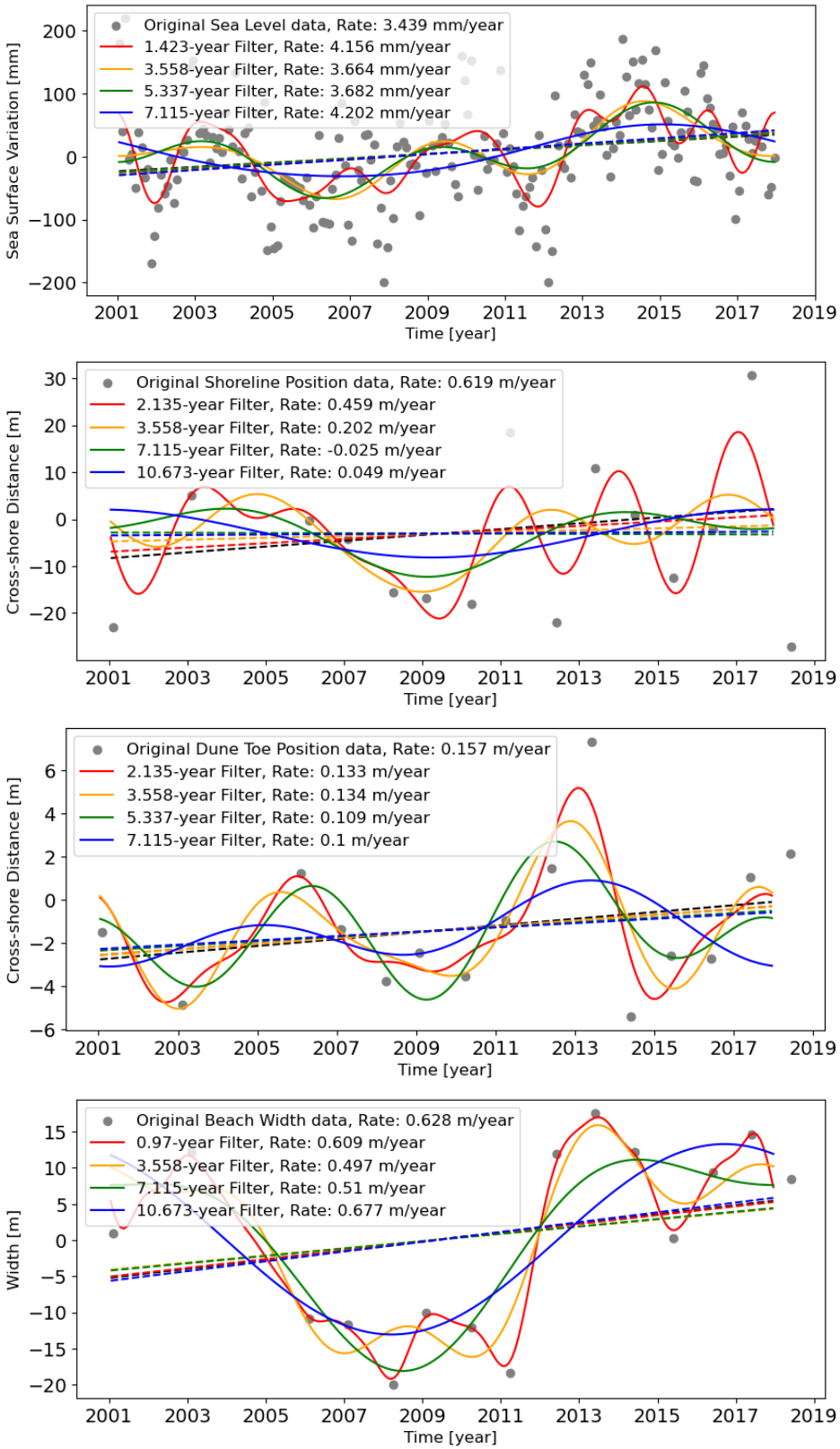

Figure 3.6: Aquitaine: Singular spectrum decomposition of sea level and topographic signal for the first eigenmode. N is the total amount of data points where the window size depends on the computation efficiency and high-frequency mechanisms to filter out.

Singular Spectrum Analysis Model

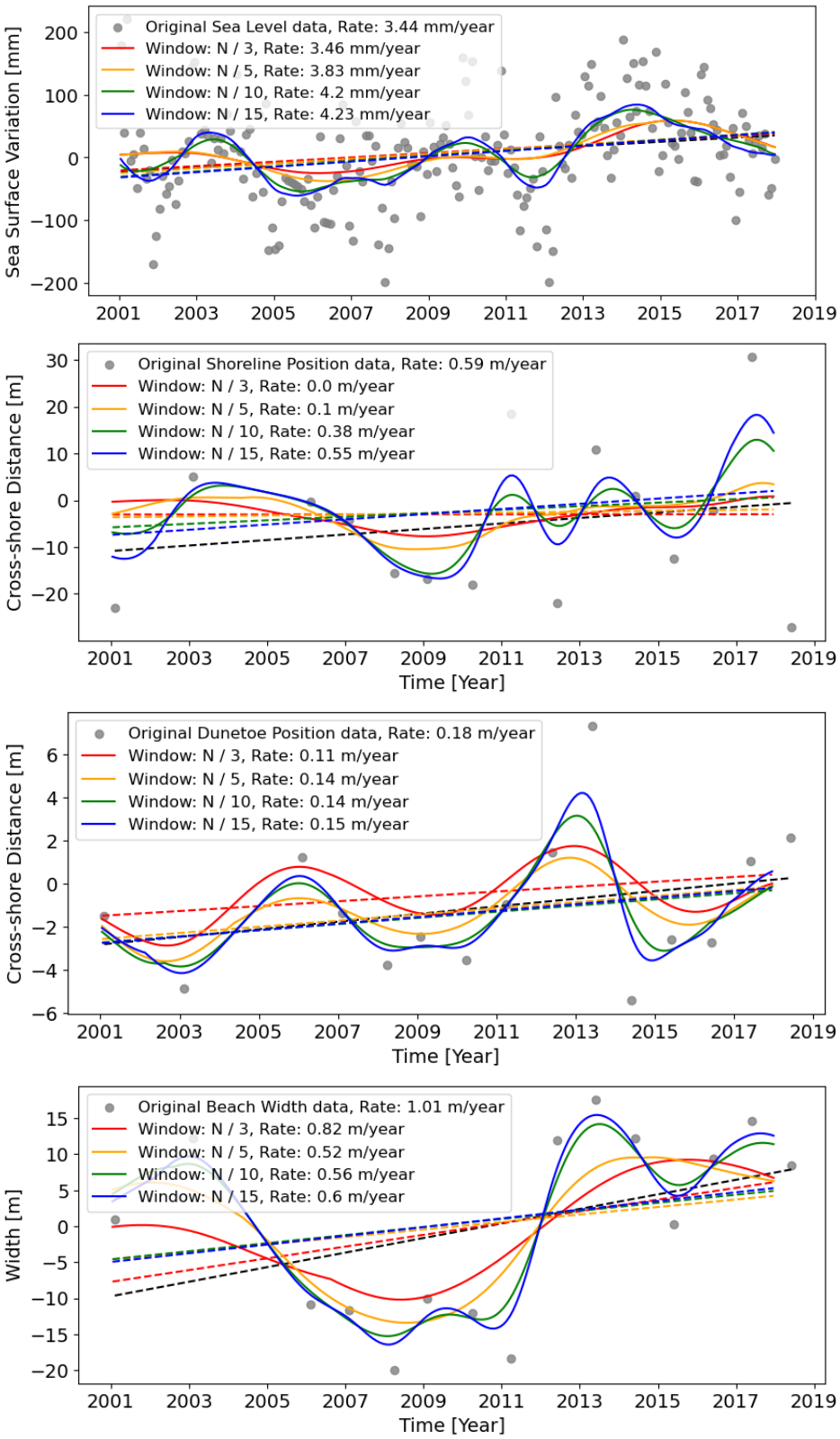

Figure 3.7: Aquitaine: Singular spectrum decomposition of sea level and topographic signal for the first eigenmode. N is the total amount of data points where the window size depends on the computation efficiency and high-frequency mechanisms to filter out.

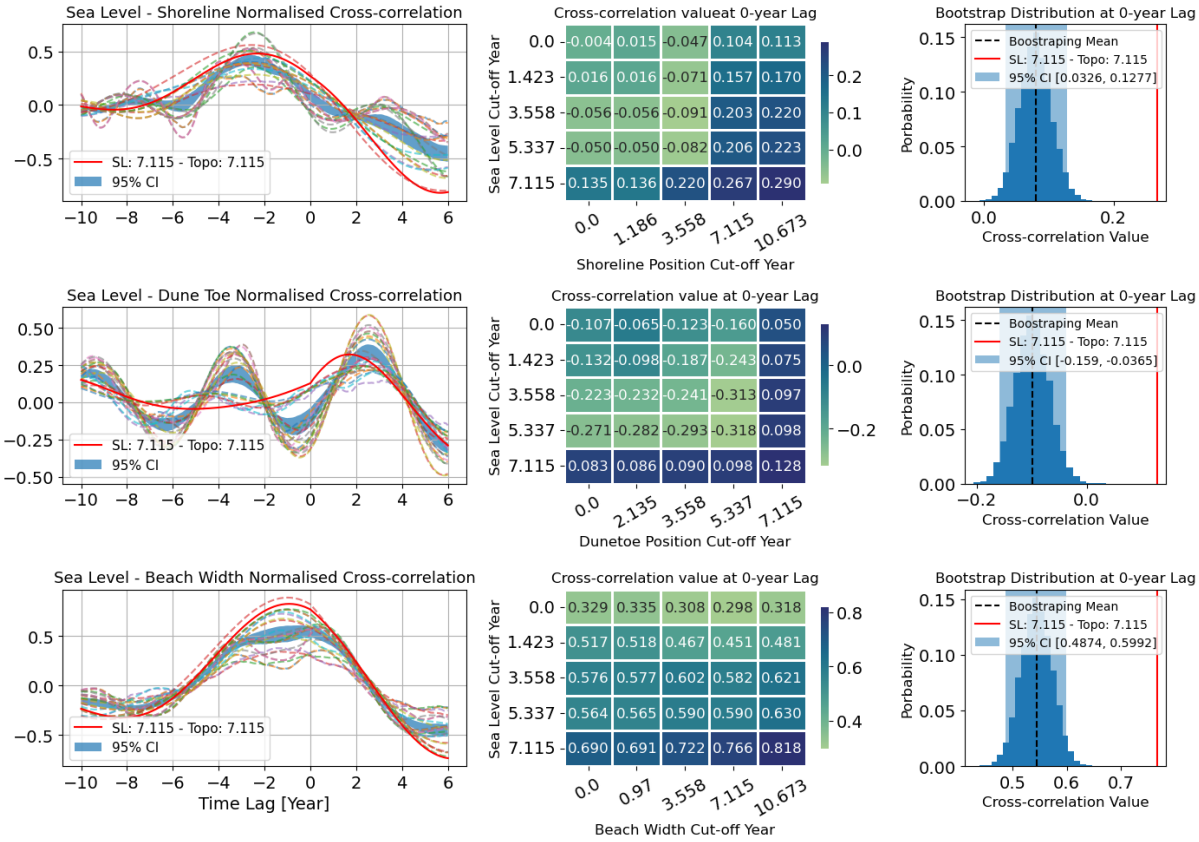

(a) IFFT normalized cross-correlation

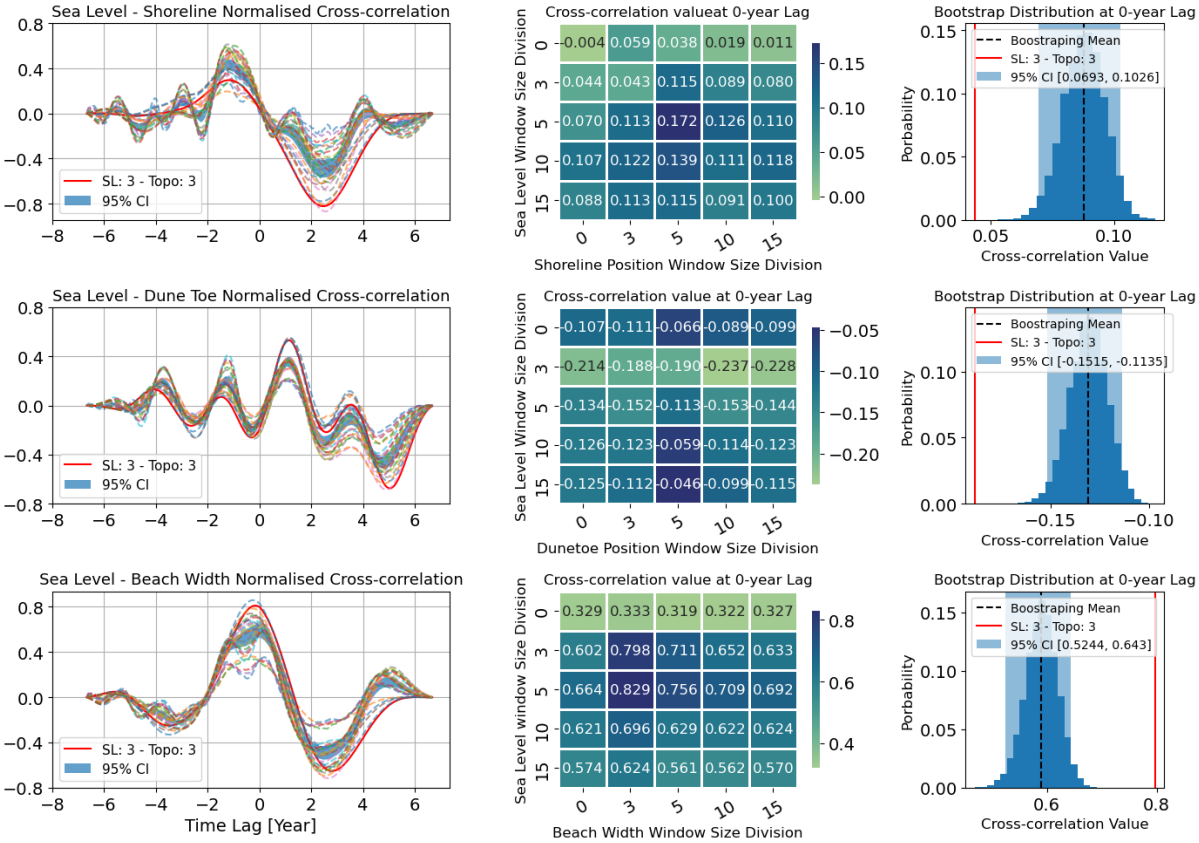

(b) SSA normalized cross-correlation

Figure 3.8: Aquitaine - Normalized cross-correlation between sea level surface and coastal indicators where the heat map and confidence interval are grounded on zero time-lag results. The legend pairs represent the combination of representative pairs, ”sea level data cutting year - indicator cutting year”.

3.2. Duck

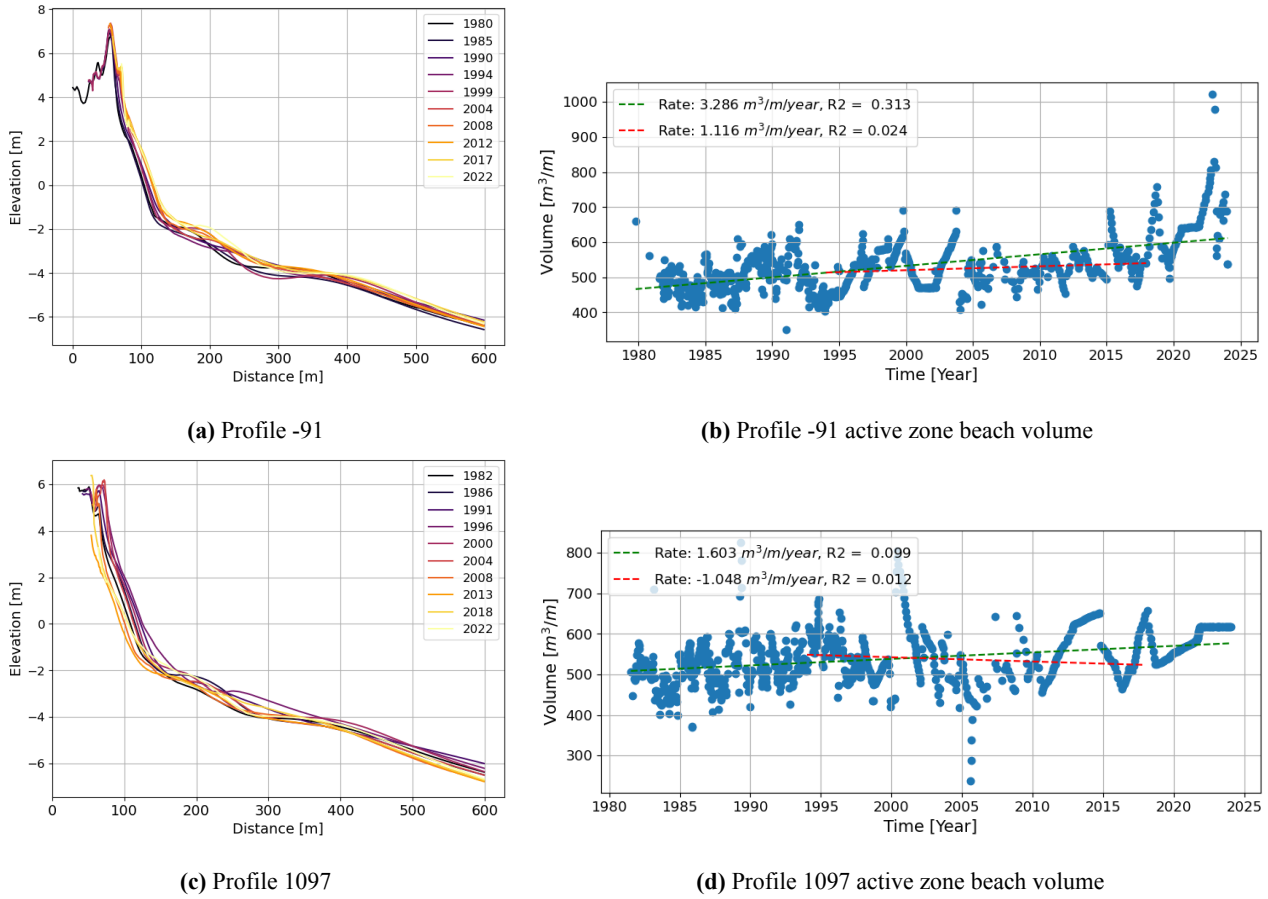

(a) Profile -91

(b) Profile -91 active zone beach volume

(c) Profile 1097

(d) Profile 1097 active zone beach volume

Figure 3.9: Duck: Evolution of two cross-section profiles north (Profile 1097) and south (Profile -91) to the pier. The measurement duration is divided into 10 segments for clear display. Beach volume is calculated from the depth of closure to the dune toe position.

The long-term evolution of the beach profile at FRF, Duck, reveals a strong regional variability at different sides of the FRF pier, shown in Figure 3.9. The direction of prevailing alongshore currents is toward the south, which conventionally leads to a shoreline accretion in the northern vicinity (Figure 3.9c) and shoreline erosion in the southern vicinity (Figure 3.9a) due to the pier-induced alongshore gradient. However, the long-term cross-section profile evolution of Profile -91 and Profile 1097 presents an opposite coastal behaviour. The coastal management type at the FRF pier region (Cohn et al., 2022) is natural and without anthropogenic engineering, it is thus difficult to deduce the reason for the peculiar migration direction. Zhang and Larson (2021) indicated that these two profiles are at the edge of the alongshore gradient influencing region, which may serve as the presumption of long-term phenomena studying.

Given the regional difference, these two profiles present two distinct migration directions. Yet without the detailed alongshore sediment transportation calculation, quantifying the contribution to any sediment-related mechanisms is difficult. Instead, the alternative is to evaluate the potential structural loss/gain of sediment amount in the active zone shown in Figure 3.9b and 3.9d. Within the studying temporal scope (the red dashed lines), the changing rate can be regarded as stable, compared to the initial sediment amount in the active zone. By inference, coastal migration at Duck Profile 1097 may possibly be attributed to the rising sea level effect rather than the influence of sediment transport.

Figure 3.10 provides the power spectrum of sea level and topographic signals at Profile 1097. Devi-

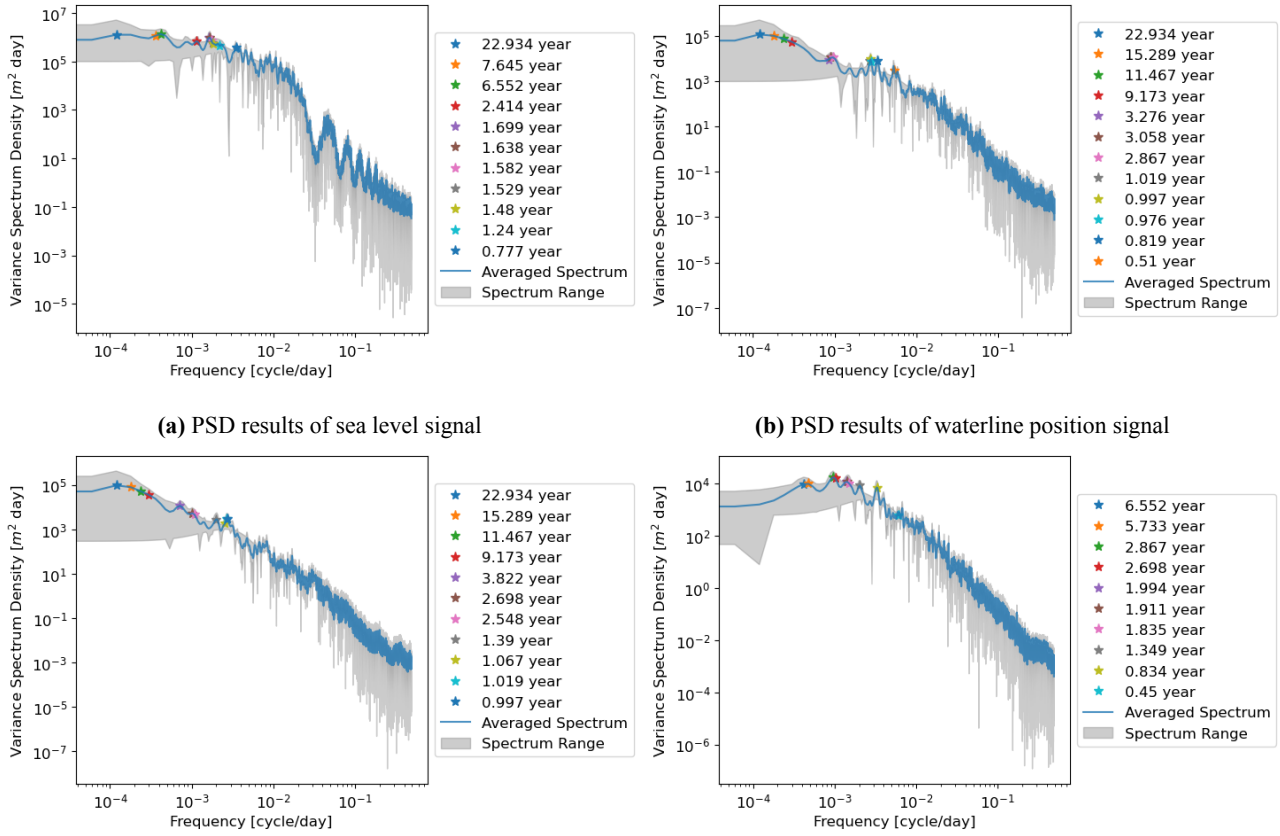

(a) PSD results of sea level signal

(b) PSD results of waterline position signal

(c) PSD results of dune toe position signal

(d) PSD results of beach width signal

Figure 3.10: Duck: Singular spectrum decomposition of sea level and topographic signal for the first eigenmode. N is the total amount of data points where the window size depends on the computation efficiency and high-frequency mechanisms to filter out.

ated from the spectrum analysis results of other coastal sites, the shoreline and dune toe position signals share more similar detected outcomes. The long-term events, 22.93-year, 15.289-year, 11.467-year, and 9.173-year, occur in both the shoreline and dune toe signals. The episodic mechanisms simultaneously exerted on the shoreline position and dune toe position. Reason can be ascribed to the narrow upper beach and primary foredune area, shown in Section 2.1.3. On the contrary, the beach width presents a distinct behaviour of composed mechanisms based on the spectrum analysis. The sea level variation acting as the driving force to topographic evolution may be weak at Profile 1097 by comparing the long-term disclosing periods in the spectrum. There is only one 22.93-year event in sea level variation - shoreline and dune toe position relation, and one 6.55-year event in sea level variation - beach width relation. The employed cut-off filter in the IFFT Model for sea level variation is 7.64 years, for shoreline position/ dune toe position is 9.173 years, and for beach width is 6.552 years. The adopted window size is the SSA Model is N/10. Despite the inconsistency of filter selection in the IFFT Model, the utilisation of different filters is based on the event-based interpretation and considered multi-decadal sea level rise impact.

The IFFT Model and SSA Model results provide identical morphological patterns at Duck Profile 1097, suggesting a coastal retrogradation. Figure 3.11 illustrates various filtered signals from the IFFT Model. The shoreline and dune toe position share a similar retreating rate, ranging from -1.5 m/year to -1.1 m/yea. In the SSA Model, the calculated results present more convergent changing rate values by applying different window sizes. The shoreline position retreated at approximately -1.55 meters per year and the dune toe position retreated at approximately -1.6 meters per year. Meanwhile, the filtered beach width signals show a relatively stable and low changing rate. The morphological

pattern satisfied the ideal sea level rise-induced coastal recession. Table 3.2 summarises the changing rate of each indicator with the corresponding filtered year.

Adhering to the changing patterns of indicators, the cross-correlation results of the IFFT and SSA models suggest that the rising sea level trends were correlated with coastal morphological responses. The bootstrapping results provide that the employments of these filters are located outside the confidence interval, showing the statistical difference. Moreover, the extreme values exist at 0 year-lag, implying these coastal adaptions to the sea level variation are in phase. It is followed by the wide-adopted intra-annual equilibrium adjustments to sea level rise-induced recession. It is thus possible to attribute the coastal recession to the rising sea level phenomenon.

Table 3.2: Duck Profile 1097: Linear Fitting results of the SSA and IFFT filtered signal, the cut-off year in the IFFT Model is 6.552 years and the window size in the SSA Model is N/10. SL: sea level variation, SP: shoreline position, DP: dune toe position, BW: beach width

Duck	SL (mm/year)	SP (m/year)	DP (m/year)	BW (m/year)	BV ($m^3/m * year$)
IFFT	3.54	-1.21	-1.2	0.0	-1.295
Cross-correlation	-	-0.735	-0.869	0.142	-
SSA	4.71	-1.57	-1.56	0.0	-1.295
Cross-correlation	-	-0.786	-0.853	0.087	-

Inverse Fourier Filtering Transform Model

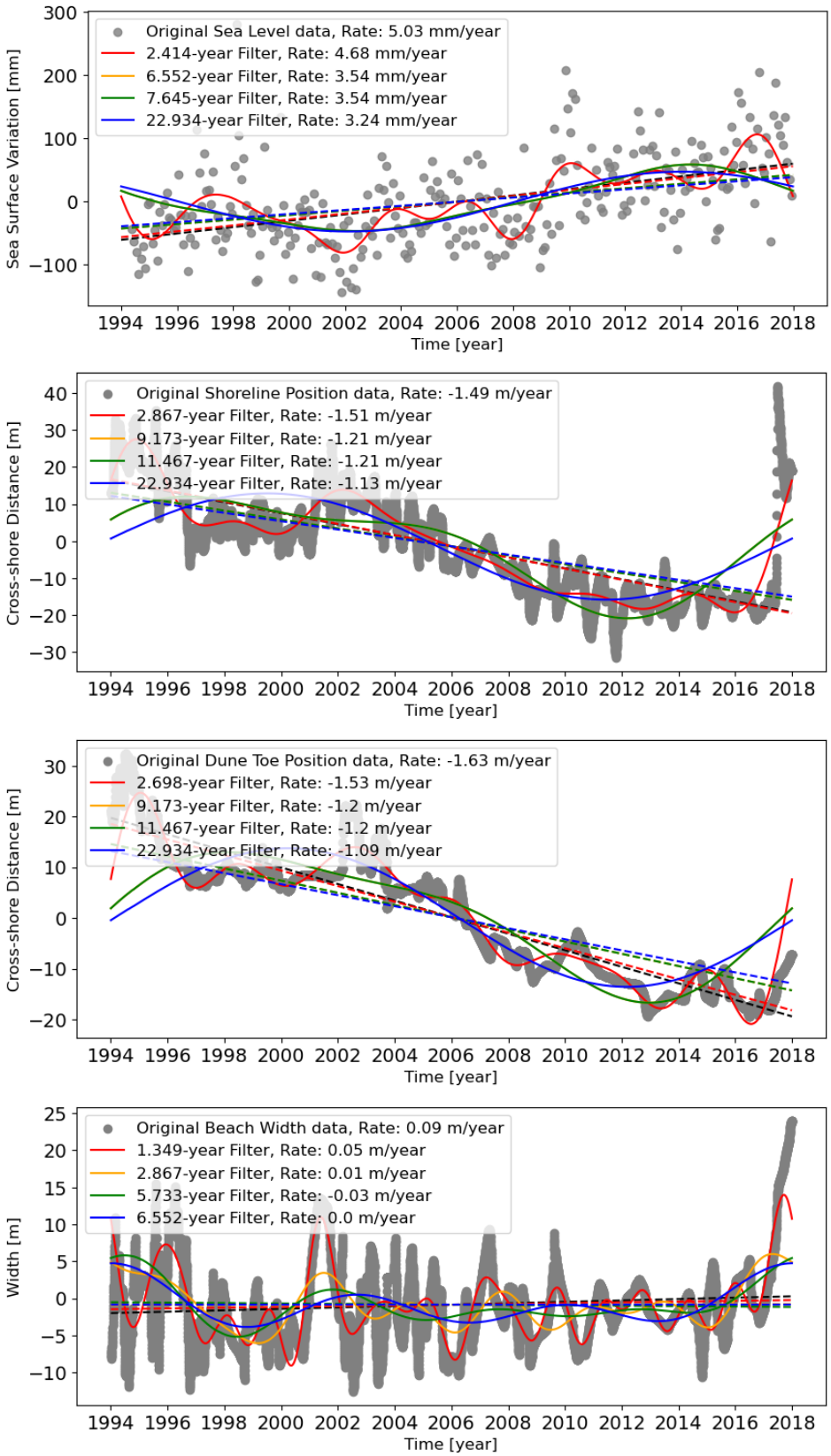

Figure 3.11: Duck: Singular spectrum decomposition of sea level and topographic signal for the first eigenmode. N is the total amount of data points where the window size depends on the computation efficiency and high-frequency mechanisms to filter out.

Singular Spectrum Analysis Model

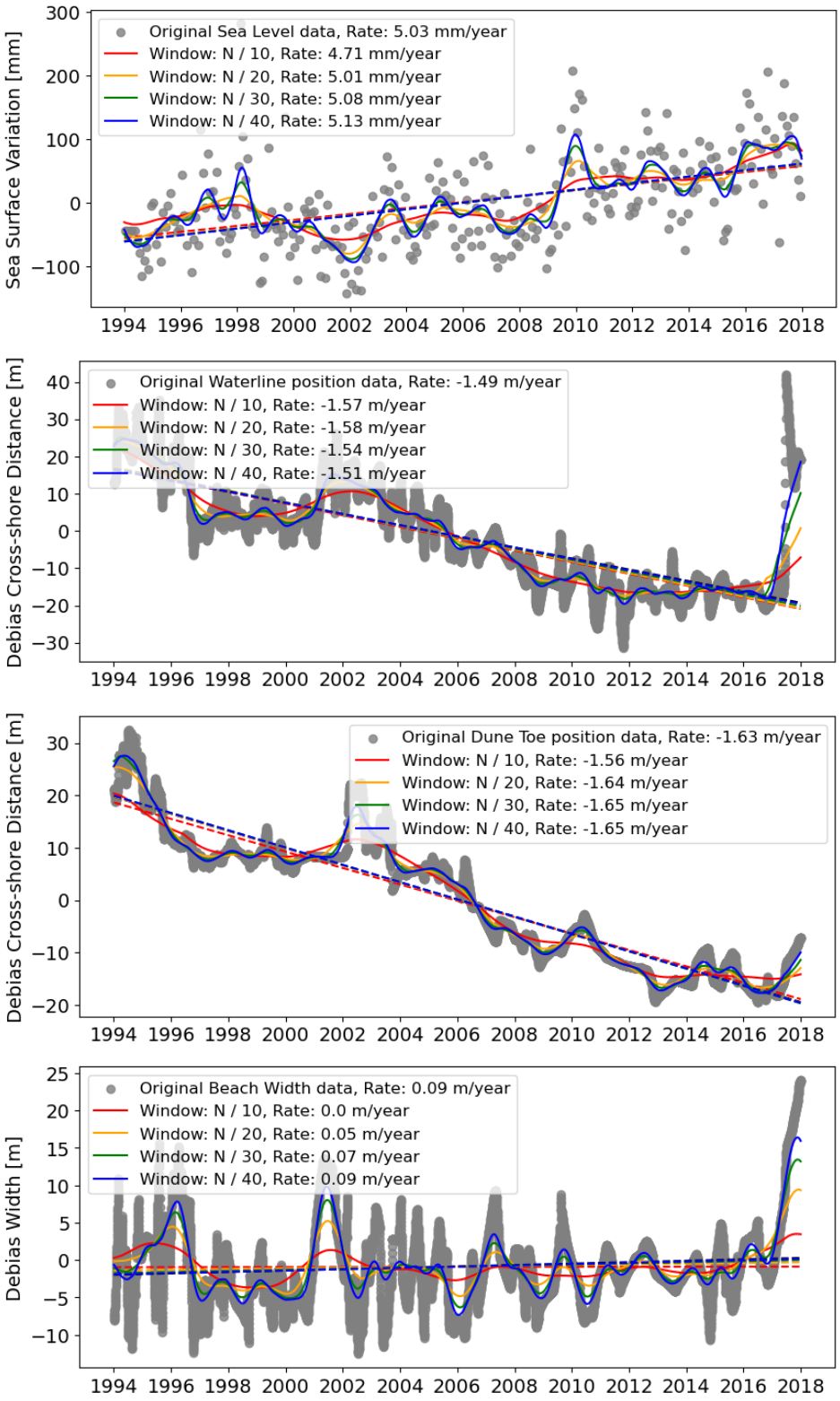

Figure 3.12: Duck: Singular spectrum decomposition of sea level and topographic signal for the first eigenmode. N is the total amount of data points where the window size depends on the computation efficiency and high-frequency mechanisms to filter out.

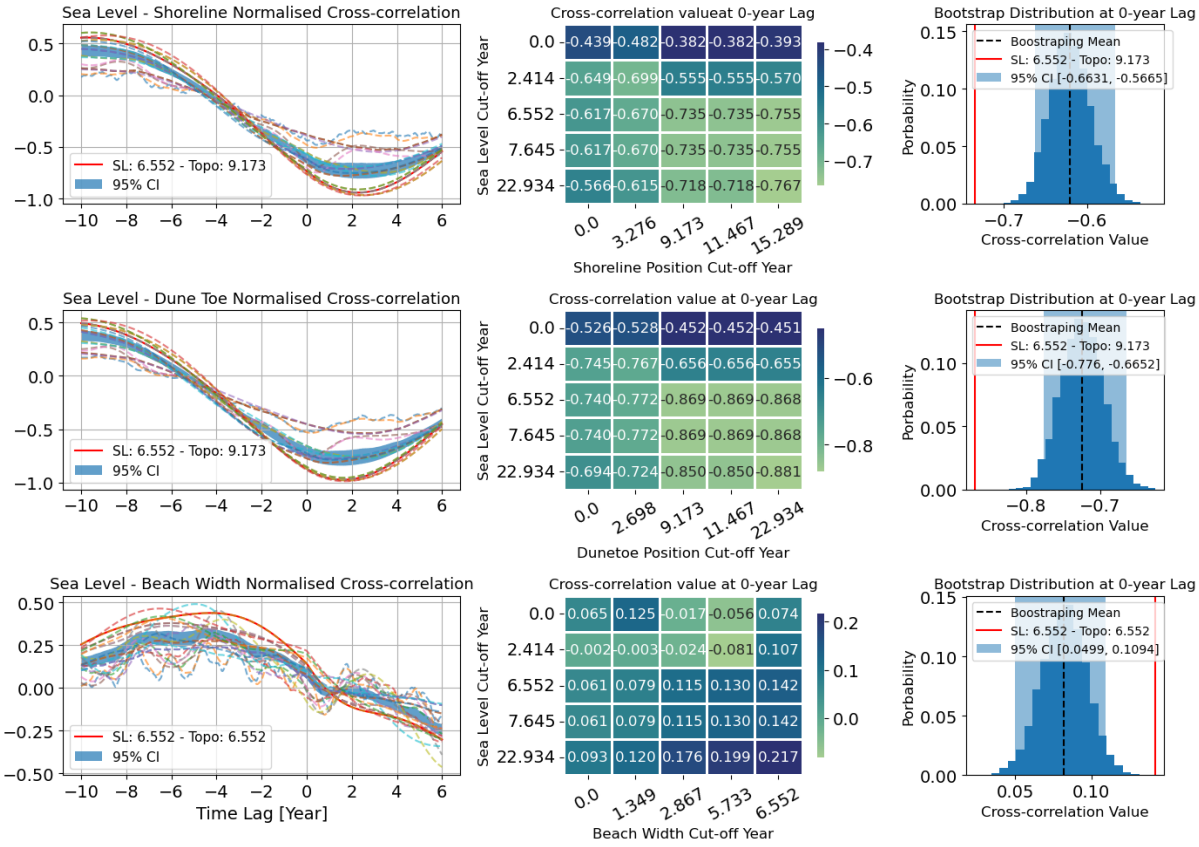

(a) IFFT normalized cross-correlation

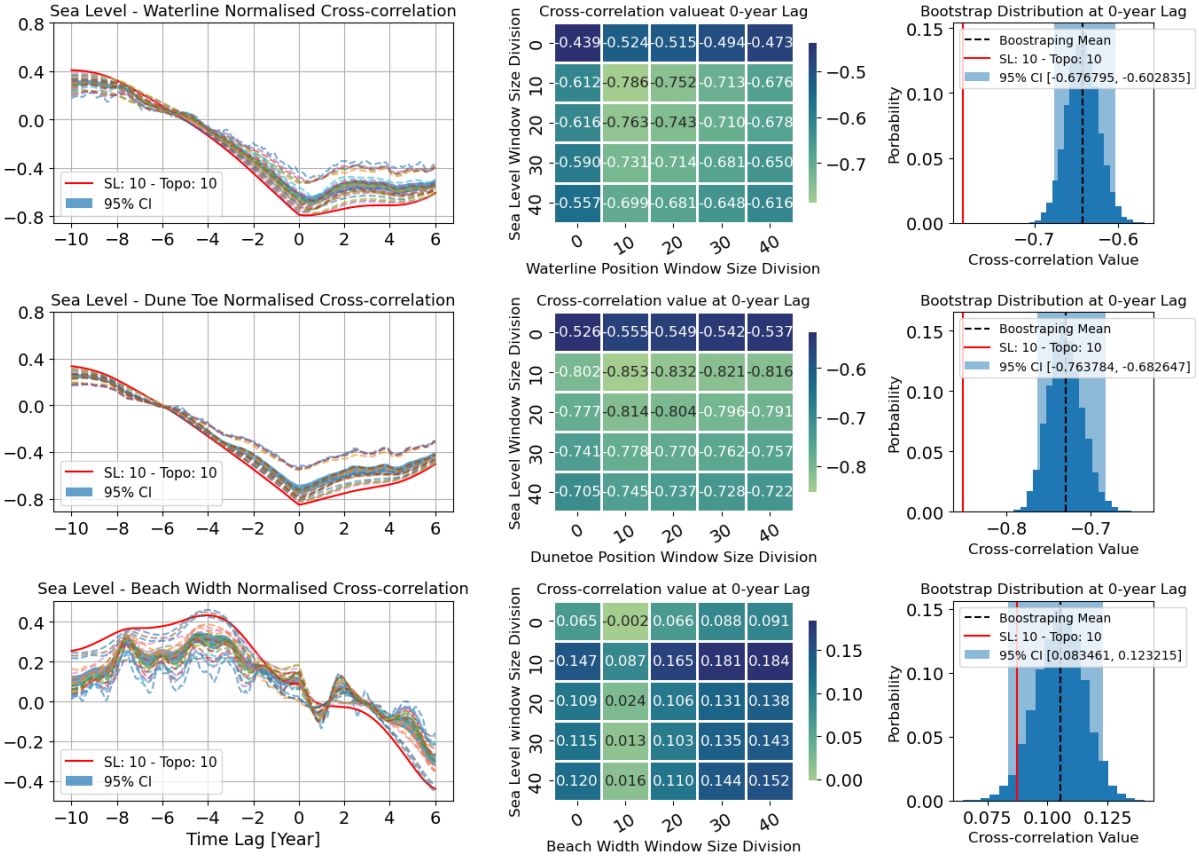

(b) SSA normalized cross-correlation

Figure 3.13: Duck - Normalized cross-correlation between sea level surface and coastal indicators where the heat map and confidence interval are grounded on zero time-lag results. The legend pairs represent the combination of representative pairs, ”sea level data cutting year - indicator cutting year”.

3.3. Hasaki

The power spectrum density results of the Hasaki coastal dataset are illustrated in Figure 3.14. As mentioned in Section 2.1.4, the dune toe position barely moved compared to the shoreline position, rendering similar evolving behaviours between shoreline position and beach width. The power spectrum analysis indicates nearly constituted rhythmic events between shoreline position and beach width, while distinct detected mechanism composition in the dune toe position. Comparing the power spectrum outcomes between shoreline position, and dune toe position, there are two identical detected long-period events, 5.61 years and 11.22 years in both sea level and dune toe position while only one period, 5.61 years in shoreline position. This suggests that the morphological formation of the dune system may be ascribed to the long-term sea level variation, whereas the formation of shoreline position is to other mechanisms.

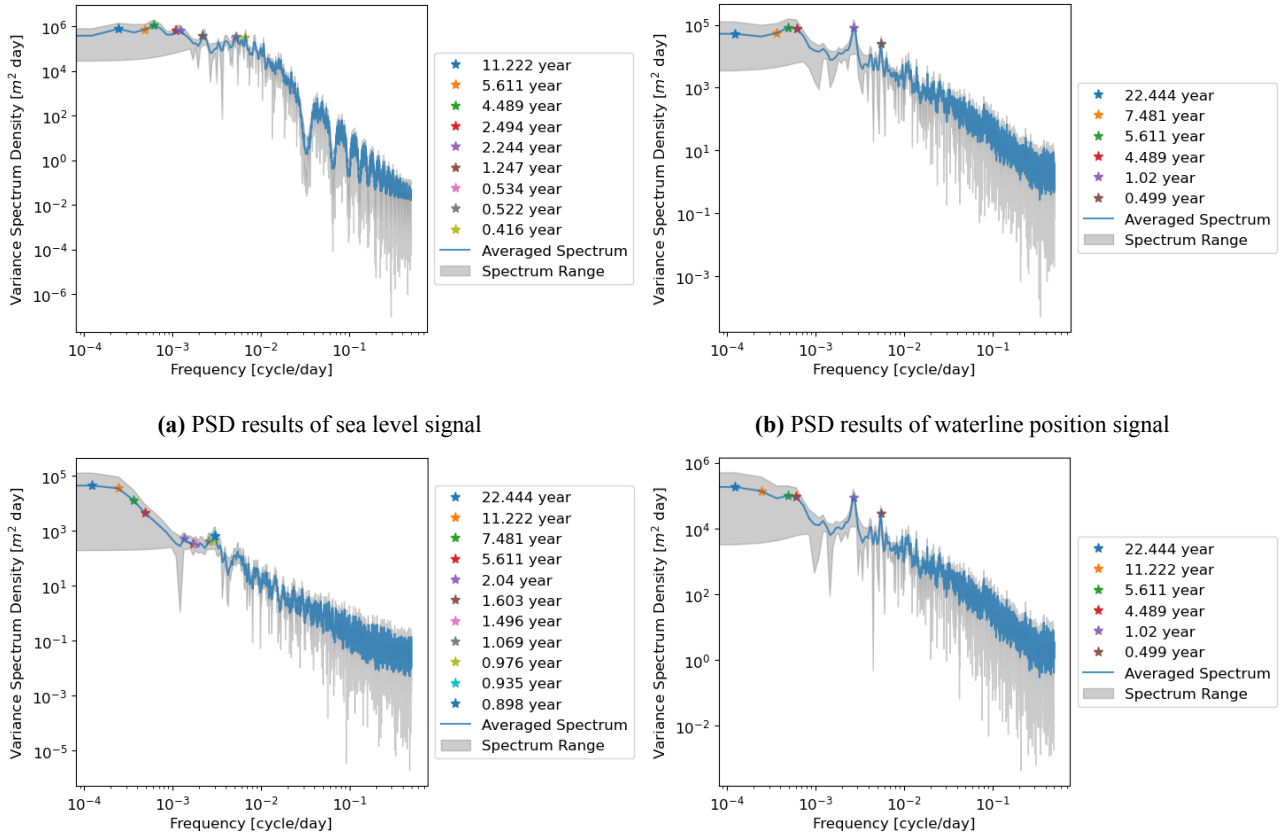

(a) PSD results of sea level signal

(b) PSD results of waterline position signal

(c) PSD results of dune toe position signal

(d) PSD results of beach width signal

Figure 3.14: Hasaki: Singular spectrum decomposition of sea level and topographic signal for the first eigenmode. N is the total amount of data points where the window size depends on the computation efficiency and high-frequency mechanisms to filter out.

Compared to other coastal sites, both the IFFT and SSA models' calculated changing rates of sea level and coastal indicators are more convergent. The model's results indicate that the waterline position and the dune toe position were migrating in opposite directions with a narrowing front beach. Table 3.3 shows the calculated changing rates of the sea level and indicators by applying different cut-off filters and window sizes. Two cut-off filters were therefore performed as the candidates in the cross-correlation analysis. The first one is the 5.61-year and the other one is the 11.22-year, which both provide the long-term hydrodynamical meanings and consistency among signals.

The cross-correlation analysis presented two distinct results in Figure 3.17, where the 11.22-year cut-off year filter of sea level signal strongly deviates from others. This is because merely a few Fourier

waves were embedded in the reconstructed signals, forming a long-period and small-amplitude long wave (see the blue line in Figure 3.15). The cross-correlation results will be contingent on the relatively complicated signal and derive high-correlated inner product values. Hence, in reality, implementing the 5.61-year filter onto all datasets is more persuasive while regarding the beach profile response to the sea level rise. As for the SSA Model, the adopted window size is N/10.

The cross-correlation results of the IFFT Model with a 5.61-year cut-off filter and the SSA Model both suggest that there is no relation between rising sea level signal and coastal response. At zero lag, all the correlation values are almost zero and located outside the bootstrapping confidence interval. This demonstrates the very weak relationship between sea level variation and topographic changes. Moreover, the opposite long-term evolution trends of shoreline and dune toe position are contradictory to the conventional sea level rise-induced coastal recession. It is then dubious to connect the profile evolution with sea level rise effects, especially since the rising magnitude is relatively slower than other coastal sites.

Table 3.3: Hasaki: Linear Fitting results of the SSA and IFFT filtered signal, the cut-off year in IFFT Model is 5.611 year and the window size in SSA Model is N/10. SL: sea level variation, SP: shoreline position, DP: dune toe position, BW: beach width

Hasaki	SL (mm/year)	SP (m/year)	DP (m/year)	BW (m/year)	BV ($m^3/m * year$)
IFFT	0.62	-0.64	0.42	-1.06	-
Cross-correlation	-	-0.020	0.086	-0.052	-
SSA	0.64	-0.69	0.48	-1.17	-
Cross-correlation	-	-0.006	0.088	-0.043	-

Inverse Fourier Filtering Transform Model

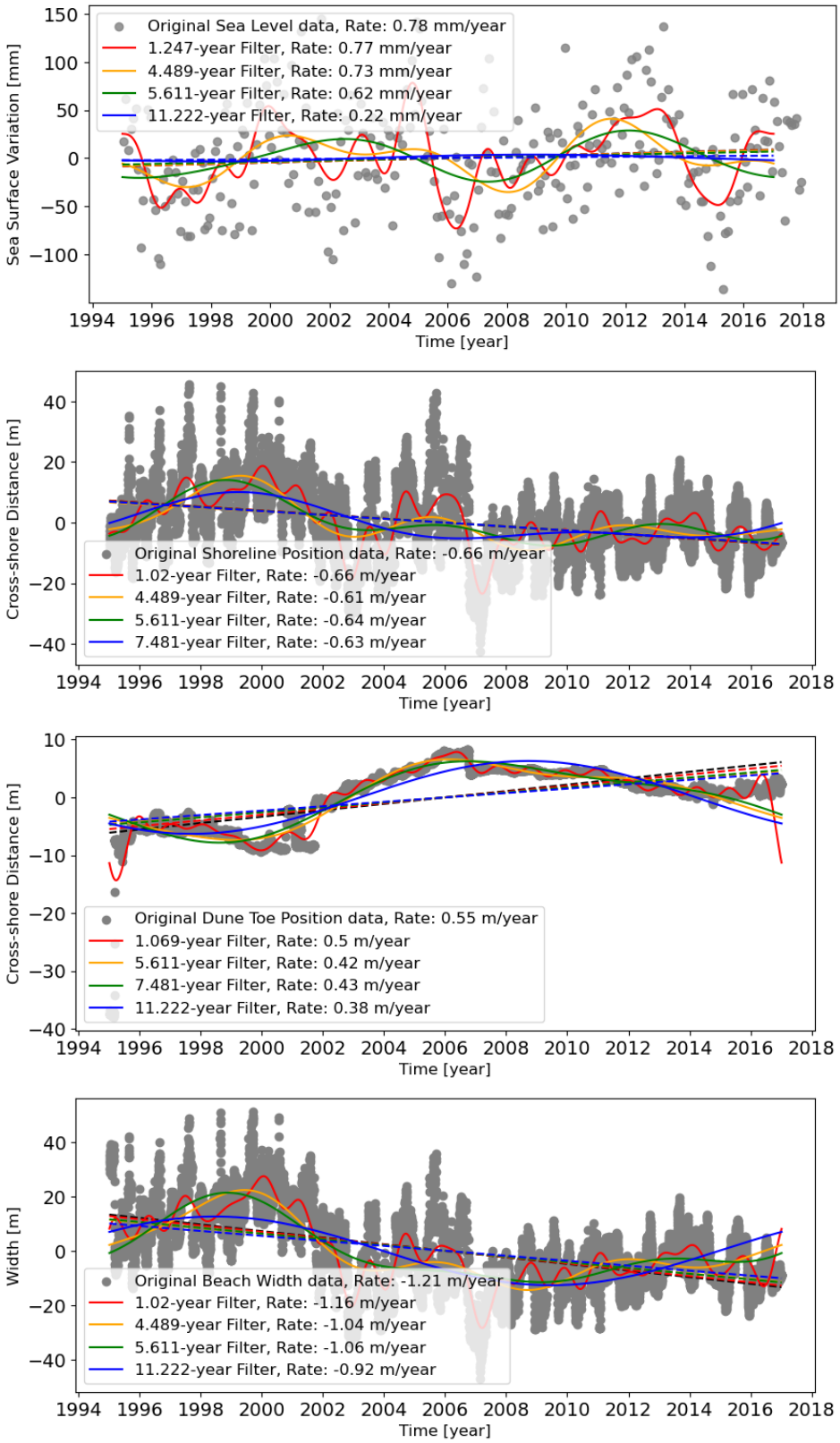

Figure 3.15: Hasaki: Singular spectrum decomposition of sea level and topographic signal for the first eigenmode. N is the total amount of data points where the window size depends on the computation efficiency and high-frequency mechanisms to filter out.

Singular Spectrum Analysis Model

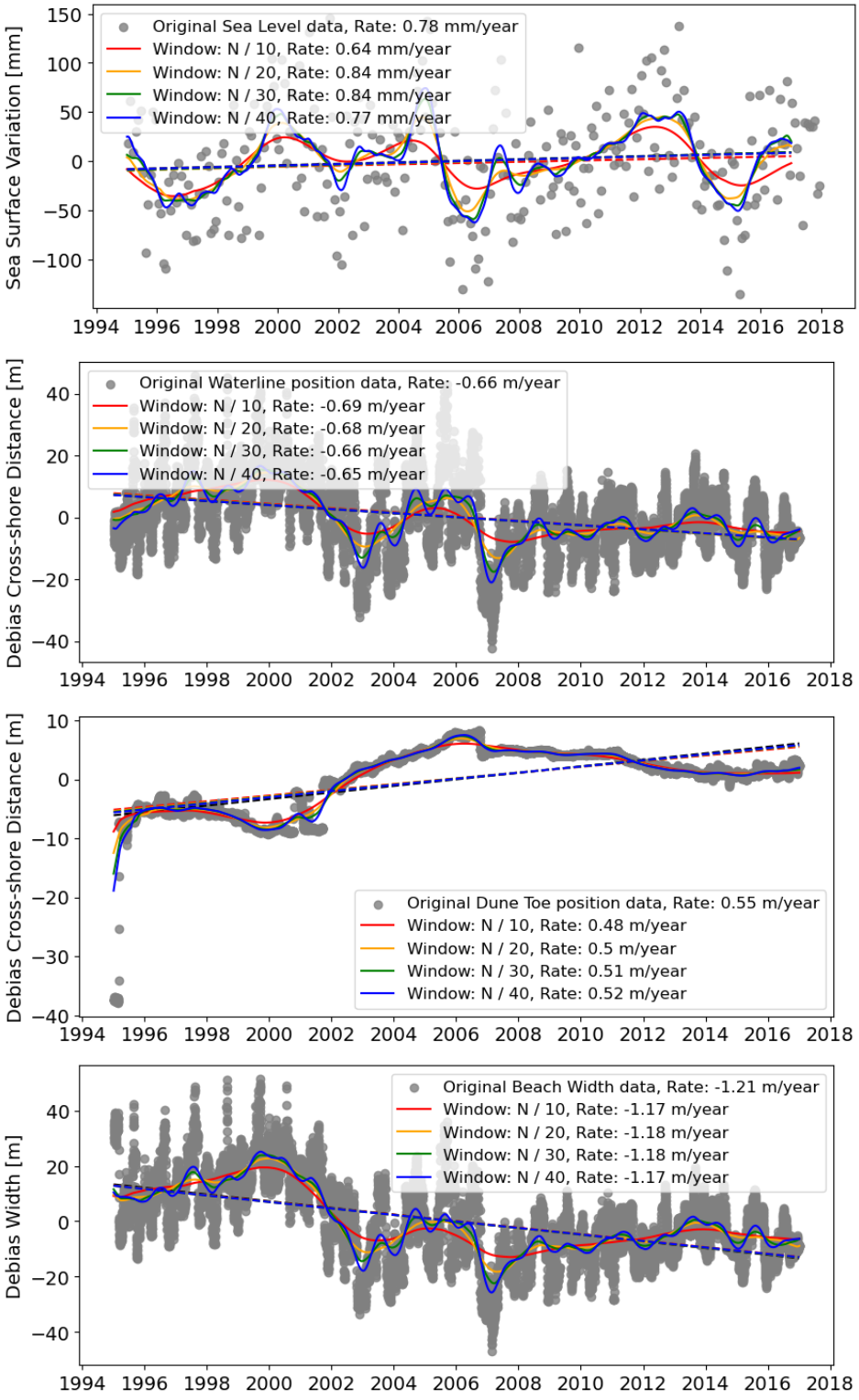

Figure 3.16: Hasaki: Singular spectrum decomposition of sea level and topographic signal for the first eigenmode. N is the total amount of data points where the window size depends on the computation efficiency and high-frequency mechanisms to filter out.

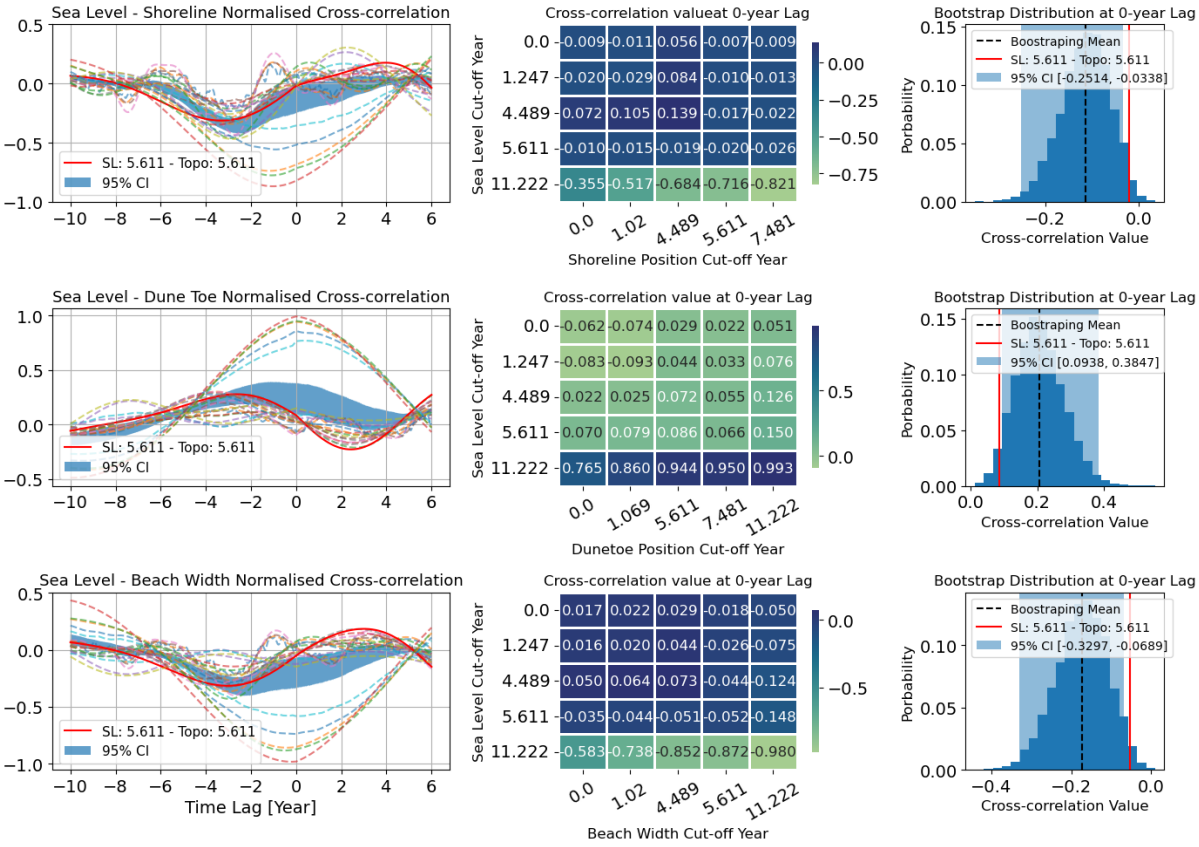

(a) IFFT normalized cross-correlation

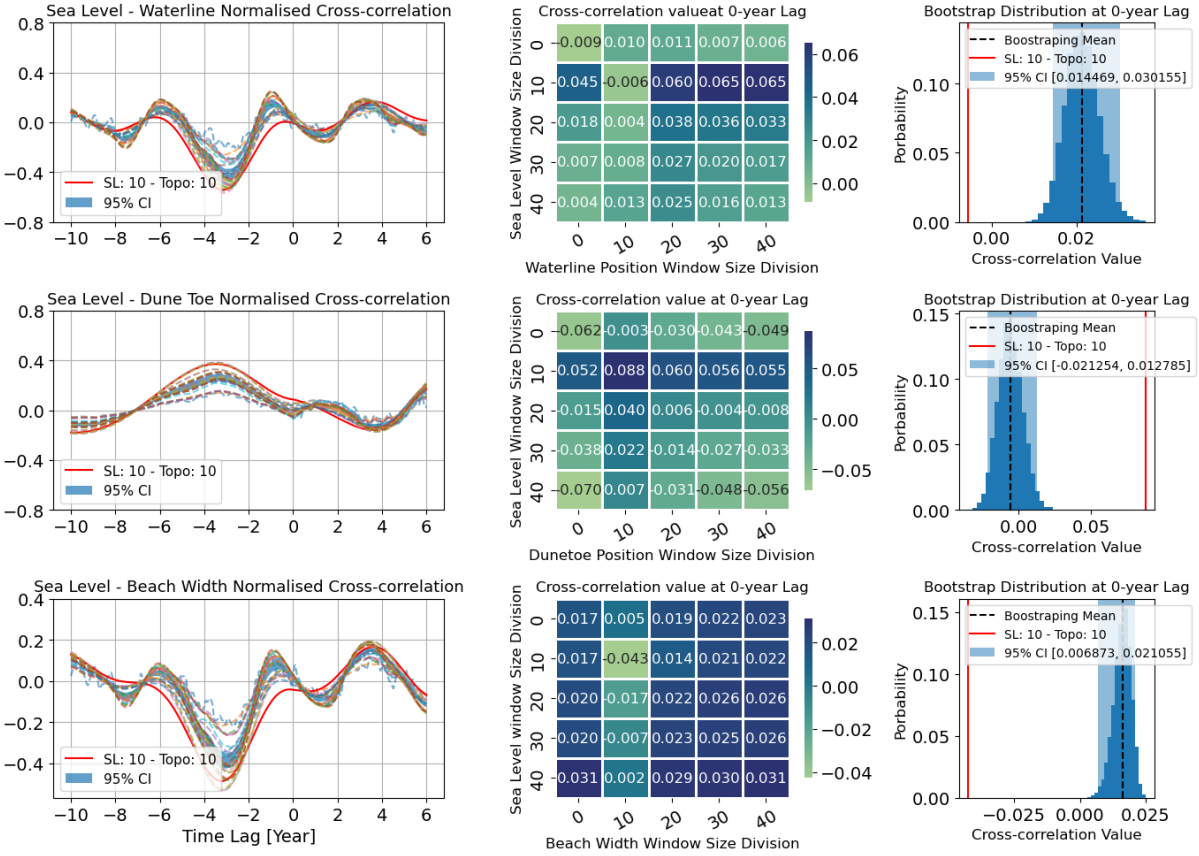

(b) SSA normalized cross-correlation

Figure 3.17: Hasaki - Normalized cross-correlation between sea level surface and coastal indicators where the heat map and confidence interval are grounded on zero time-lag results. The legend pairs represent the combination of representative pairs, ”sea level data cutting year - indicator cutting year”.

3.4. Jarkus

This section will present the analysed morphological evolution of the coastal area and its interaction with sea level variation at the Holland Coast. The first subsection will mention the power spectrum, IFFT Model, and SSA Model results of the sandy coast at Noordwijk, South Holland, and the other subsection will elaborate on the outcomes at Egmond, North Holland.

At Noordwijk, the rhythmic events detected from the power spectrum density results reveal intricate and massive driving forces for evolution were involved. The constituted mechanisms of shoreline position and beach width are more uniform and dissimilar for the dune toe position, shown in Figure 3.18. Rather than the 21.34-year sea level variation event contributing to the dune system formation, the identical longest period detected in both the sea level and dune toe signals is 6.099-year. The difference implies that additional multiple long-term events affect the development of the dune system. By contrast, the long-term 9.49-year and 10.67-year signals are found in the sea level variation, shoreline position, and beach width, but not in the dune toe position signal. This difference in morphological driving force at a long-term scale suggests that the long-term foreshore evolution is attributed to the decadal sea level variation rather than the rising sea level phenomenon. Consistent with the deduction, the 10.673-year filter was applied for sea level, shoreline position, and beach width signals instead of the 6.099-year filter. Despite the inconsistency, the 14.231-year filter was selected for the dune toe position signal in the IFFT Model under physical consideration.

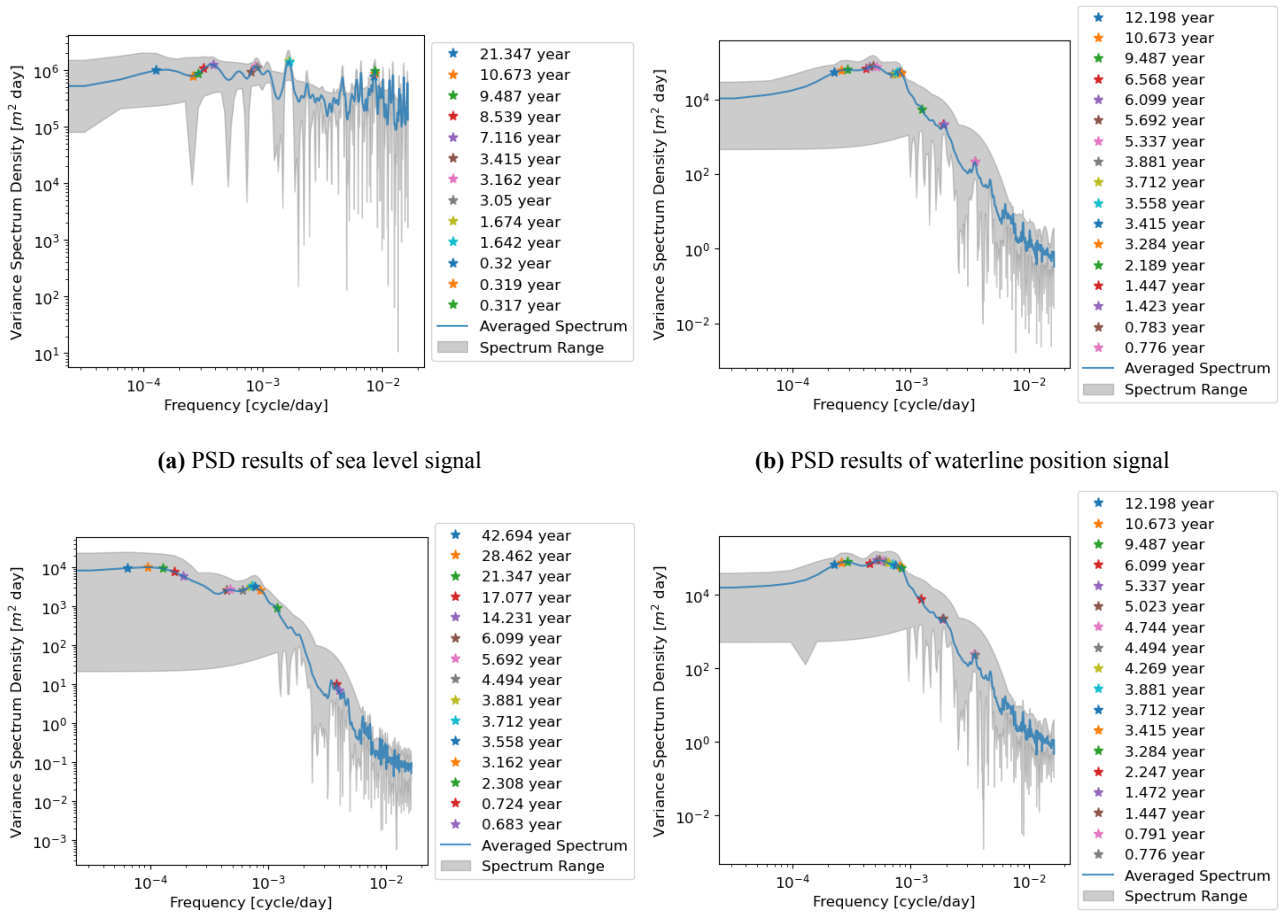

(a) PSD results of sea level signal

(b) PSD results of waterline position signal

(c) PSD results of dune toe position signal

(d) PSD results of beach width signal

Figure 3.18: Noordwijk: Singular spectrum decomposition of sea level and topographic signal for the first eigenmode. N is the total amount of data points where the window size depends on the computation efficiency and high-frequency mechanisms to filter out.

Compared to the power spectrum results at Noordwijk, Figure 3.19 illustrates that the long-term constituted mechanisms embedded in the signals are more demarcating at Egmond. The derived sea level variation spectrum provides a distinct period composition from topographic ones. The common interaction between sea level variation and topographic morphological change is the 4.494-year event, whereas more long-term mechanisms were discovered in forming the subaerial terrain. The 17.08-year and 14.23-year events only exist in the topographic data, showing that the morphological shaping forces for terrain may not directly originate from the sea level variation. Apart from that, the sediment transport shaping the dune system is more complicated due to other involved events. At Egmond, the cut-off filter in the IFFT Model utilized the 7.76-year filter for the sea level variation signal and the 14.23-year filter for the coastal indicators' signal.

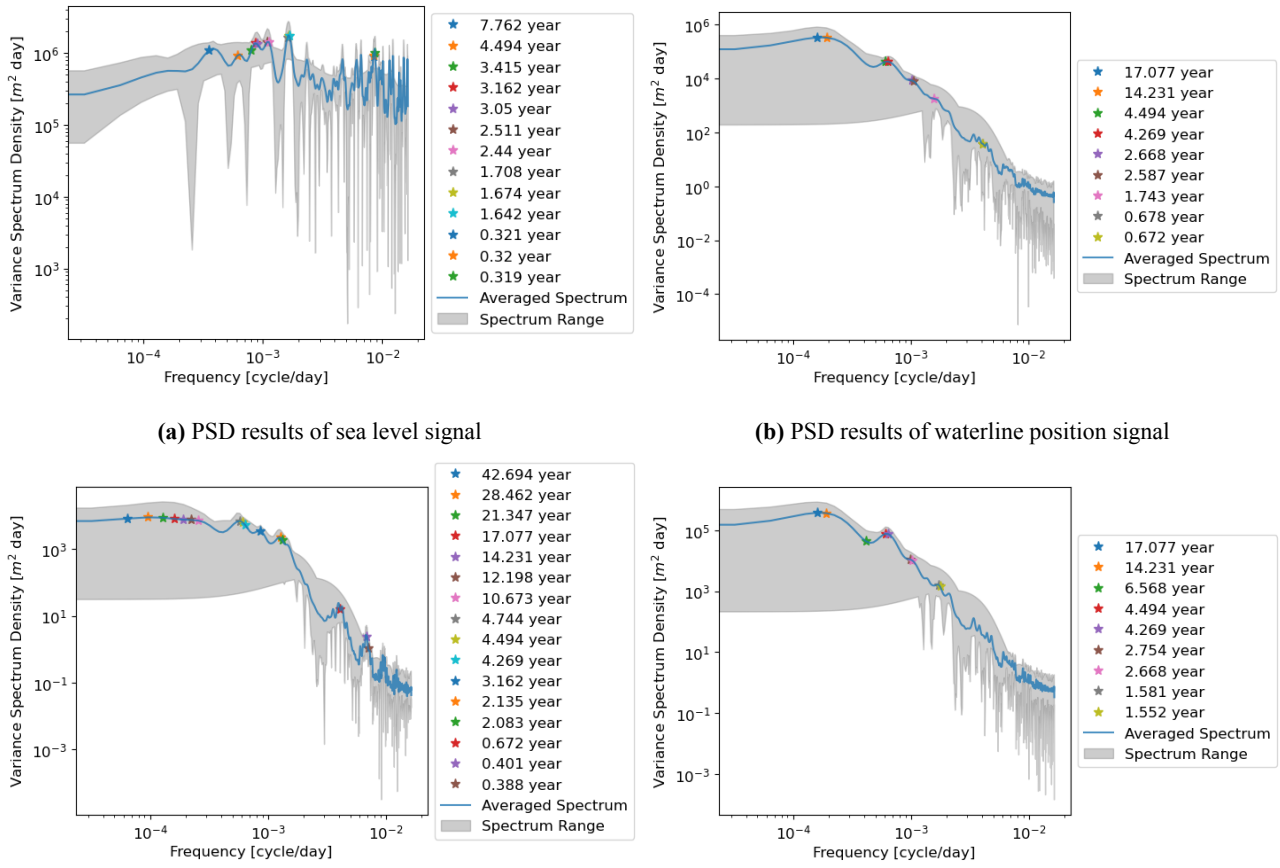

(a) PSD results of sea level signal

(b) PSD results of waterline position signal

(c) PSD results of dune toe position signal

(d) PSD results of beach width signal

Figure 3.19: Egmond: Singular spectrum decomposition of sea level and topographic signal for the first eigenmode. N is the total amount of data points where the window size depends on the computation efficiency and high-frequency mechanisms to filter out.

The IFFT Model and SSA Model suggest that the coasts at Noordwijk and Egmond were counteracting the rising sea level-induced erosion. Figure 3.20, 3.21 and Figure 3.23, 3.24 respectively show the reconstructed signals by applying the IFFT and SSA Model to two coastal sites. Table 3.4 and Table 3.5 specify that all the indicators slowly migrated seaward with an increasing width of the upper beach region. These results are similar to the coastal behaviour at the Aquitaine coast site, the coastal seaward movement was observed in both Noordwijk and Egmond. Although the spectrum analysis shows that the morphological driving forces are more complex at the Holland Coast. This proceeding coastal progradation that exists on the Holland coast is validated with the research of (van IJzendoorn et al., 2021). The environmental sediment transportation leading to coastal morphological change is more dominant than the sea level rise impact.

As the verification, the cross-correlation results of IFFT analysis and SSA analysis at these two sites (Figure 3.22 and Figure 3.25) both present a weak cross-correlation between the topographic signals and the rising sea level at zero lags. It is then convincing not to refer to a clear relationship between the sea level rising phenomenon and topographic evolutions.

Table 3.4: Noordwijk, Jarkus: Linear Fitting results of the SSA and IFFT filtered signal, the cut-off year in IFFT Model is 7.116 year and the window size in SSA Model is N/3. SL: sea level variation, SP: shoreline position, DP: dune toe position, BW: beach width

Jarkus	SL (mm/year)	SP (m/year)	DP (m/year)	BW (m/year)	BV ($m^3/m*year$)
IFFT	1.848	0.525	0.162	0.462	-
Cross-correlation	-	0.307	0.287	0.283	-
SSA	1.44	0.52	0.09	0.38	-
Cross-correlation	-	0.015	-0.138	0.142	-

Table 3.5: Egmond, Jarkus: Linear Fitting results of the SSA and IFFT filtered signal, the cut-off year in IFFT Model is 7.762 year and the window size in SSA Model is N/3. SL: sea level variation, SP: shoreline position, DP: dune toe position, BW: beach width

Jarkus	SL (mm/year)	SP (m/year)	DP (m/year)	BW (m/year)	BV ($m^3/m*year$)
IFFT	1.755	0.332	0.084	0.246	-
Cross-correlation	-	-0.013	0.156	-0.058	-
SSA	0.22	0.3	0.12	-0.41	-
Cross-correlation	-	0.040	0.004	-0.088	-

Inverse Fourier Filtering Transform Mode - Noordwijk

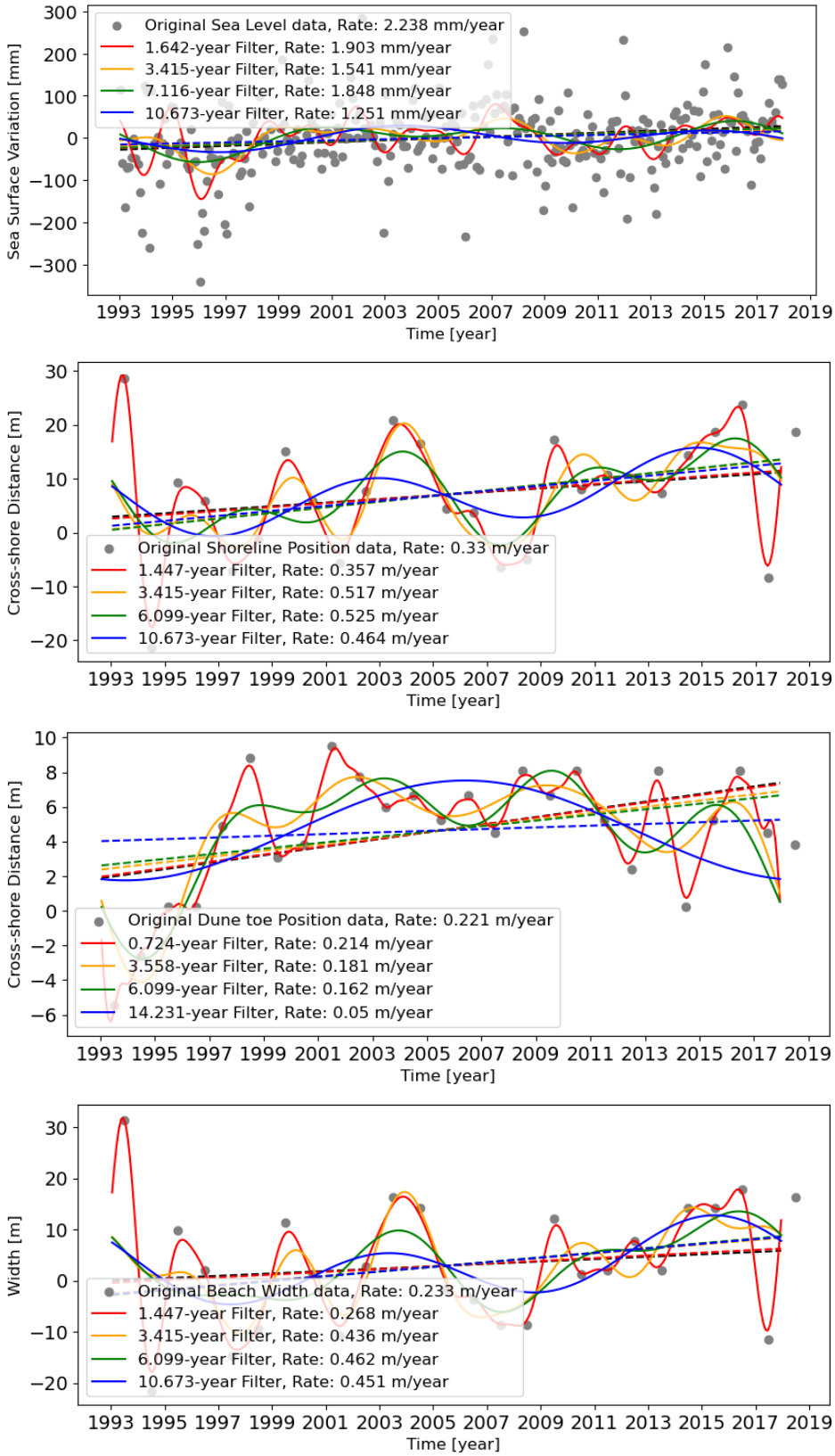

Figure 3.20: Noordwijk: Singular spectrum decomposition of sea level and topographic signal for the first eigenmode. N is the total amount of data points where the window size depends on the computation efficiency and high-frequency mechanisms to filter out.

Singular Spectrum Analysis Model - Noordwijk

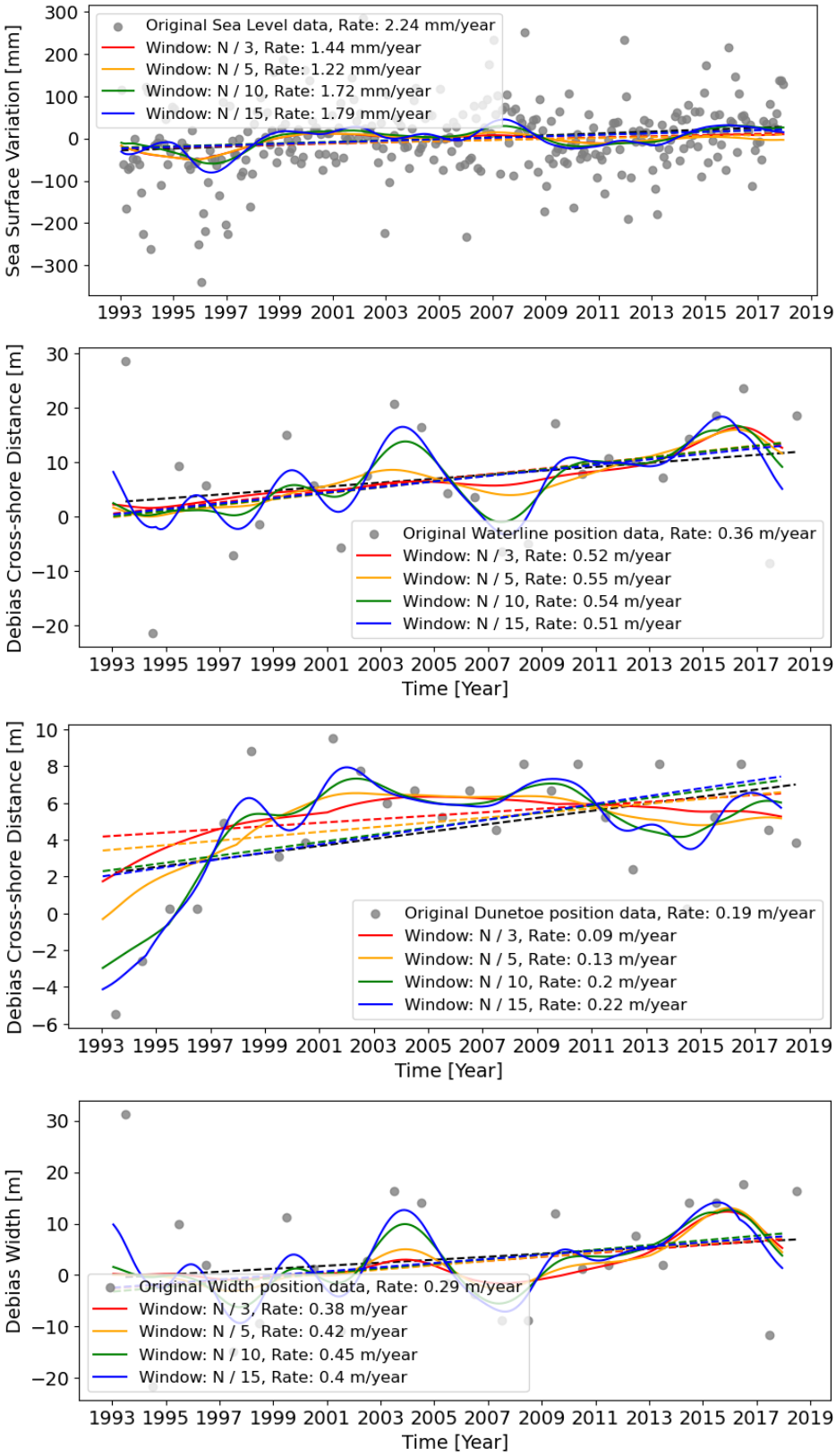

Figure 3.21: Noordwijk, Jarkus: Singular spectrum decomposition of sea level and topographic signal for the first eigenmode. N is the total amount of data points where the window size depends on the computation efficiency and high-frequency mechanisms to filter out.

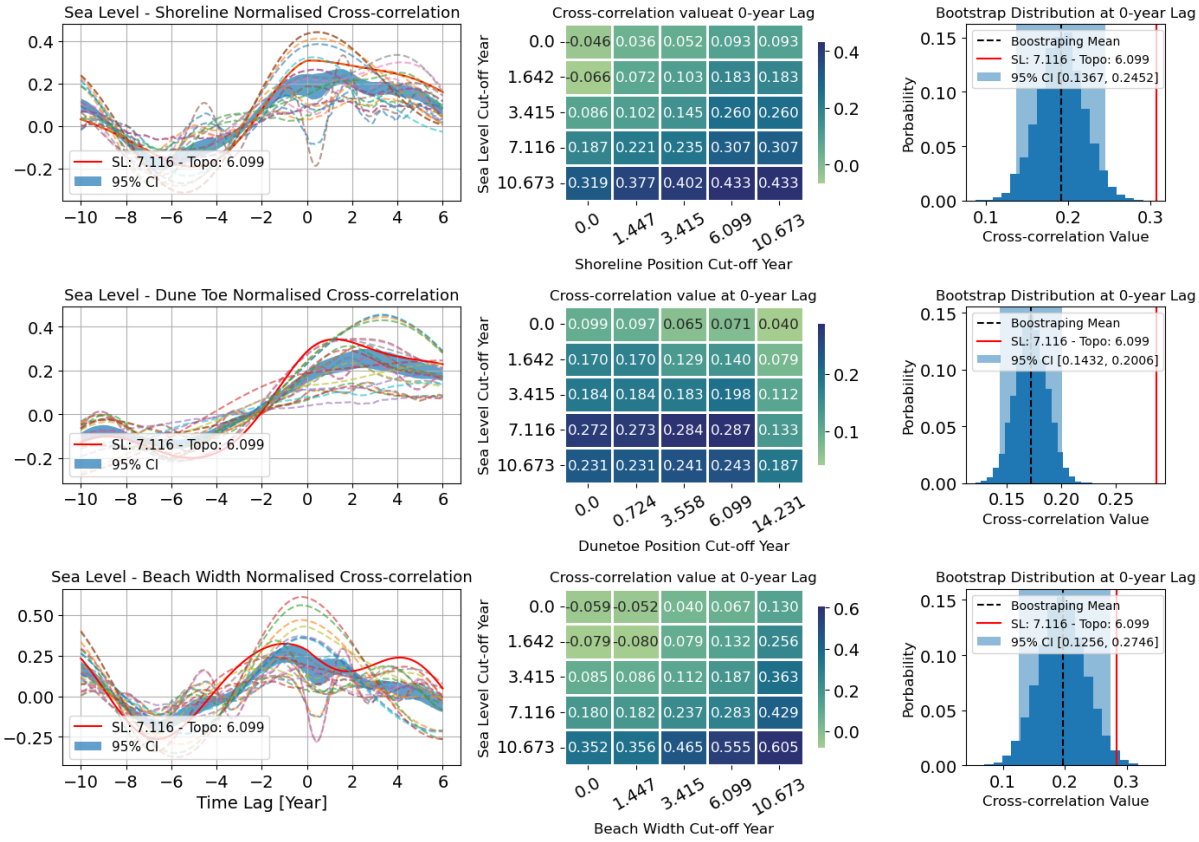

(a) IFFT normalized cross-correlation

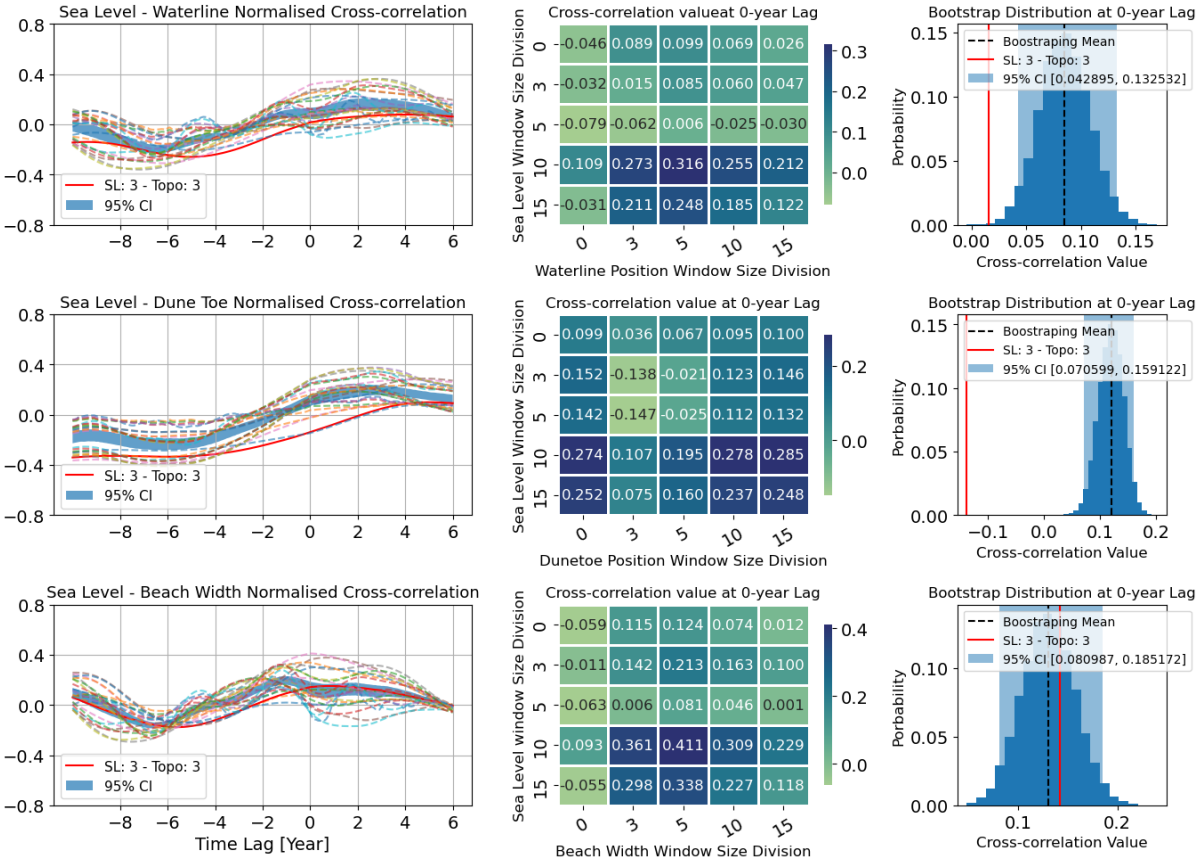

(b) SSA normalized cross-correlation

Figure 3.22: Noordwijk, Jarkus - Normalized cross-correlation between sea level surface and coastal indicators where the heat map and confidence interval are grounded on zero time-lag results. The legend pairs represent the combination of representative pairs, ”sea level data cutting year - indicator cutting year”.

Inverse Fourier Filtering Transform Model - Egmond

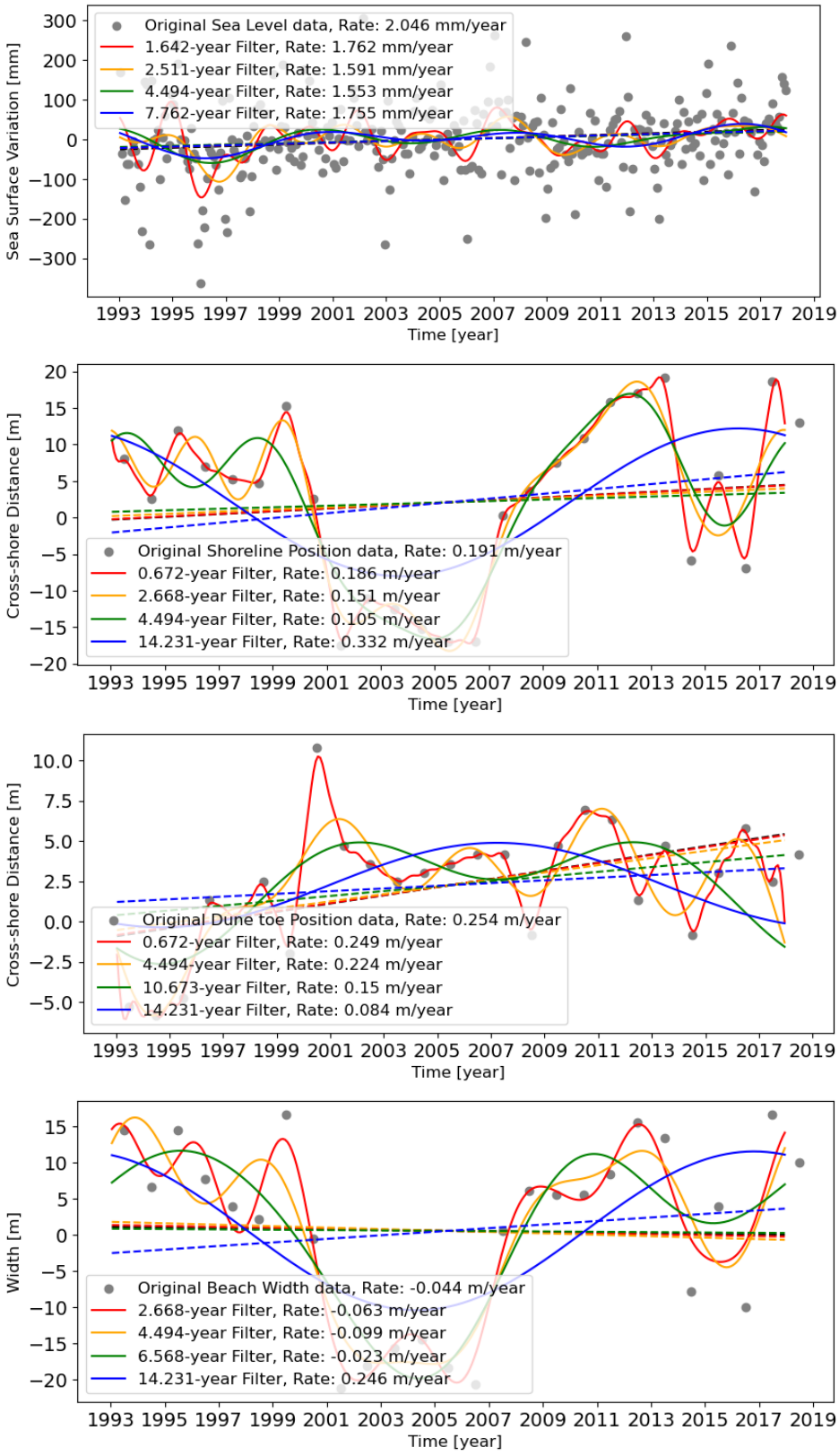

Figure 3.23: Egmond: Singular spectrum decomposition of sea level and topographic signal for the first eigenmode. N is the total amount of data points where the window size depends on the computation efficiency and high-frequency mechanisms to filter out.

Singular Spectrum Analysis Model - Egmond

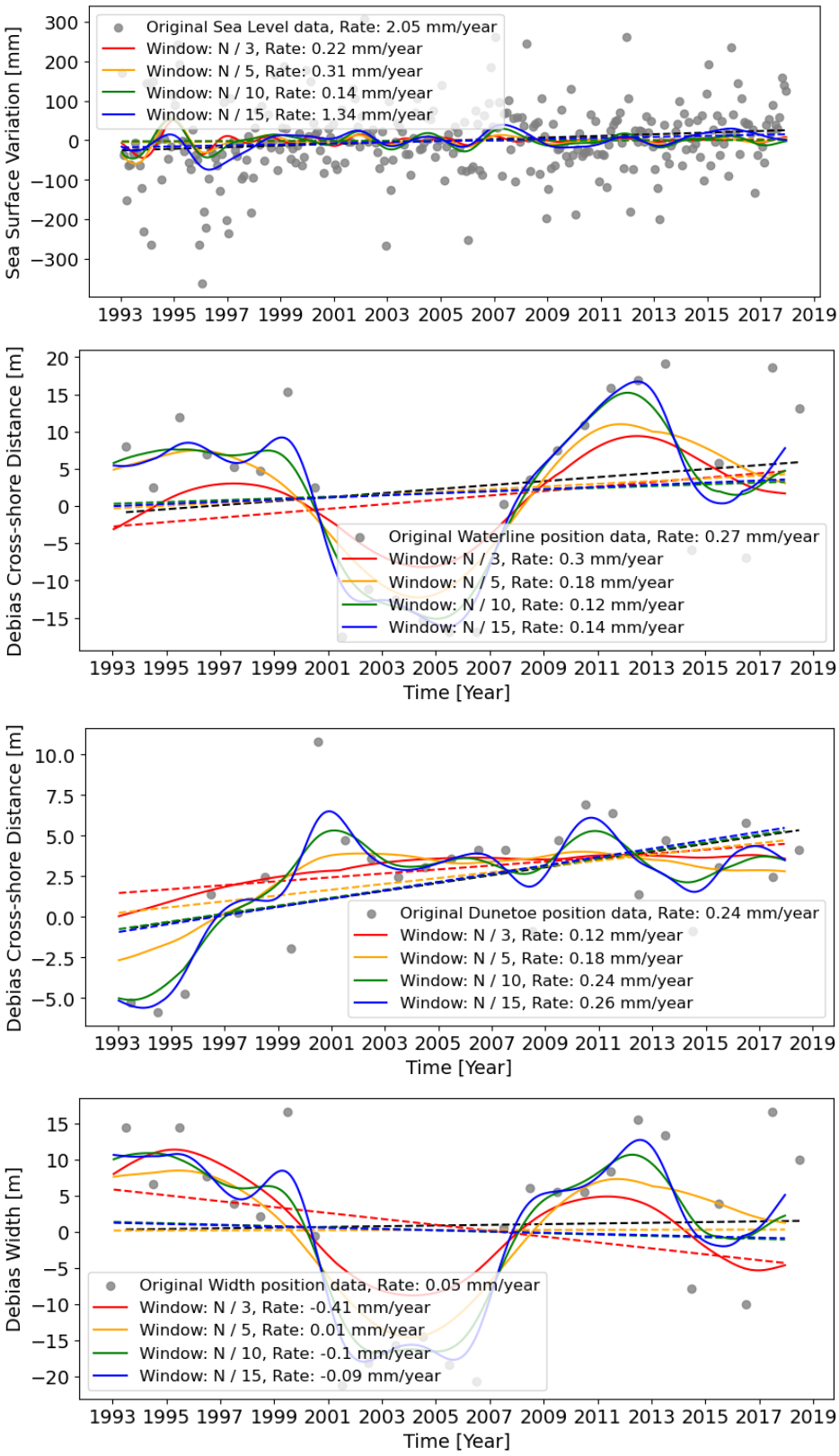

Figure 3.24: Egmond, Jarkus: Singular spectrum decomposition of sea level and topographic signal for the first eigenmode. N is the total amount of data points where the window size depends on the computation efficiency and high-frequency mechanisms to filter out.

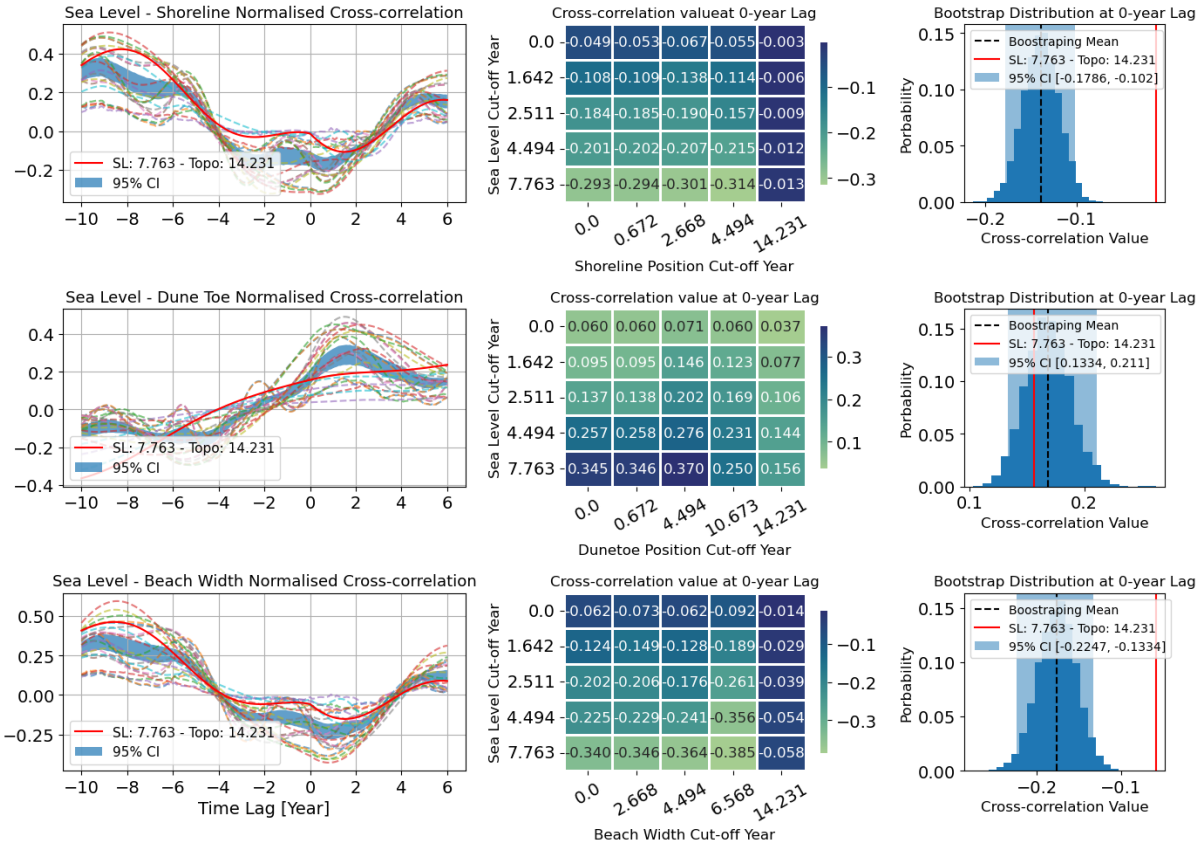

(a) IFFT normalized cross-correlation

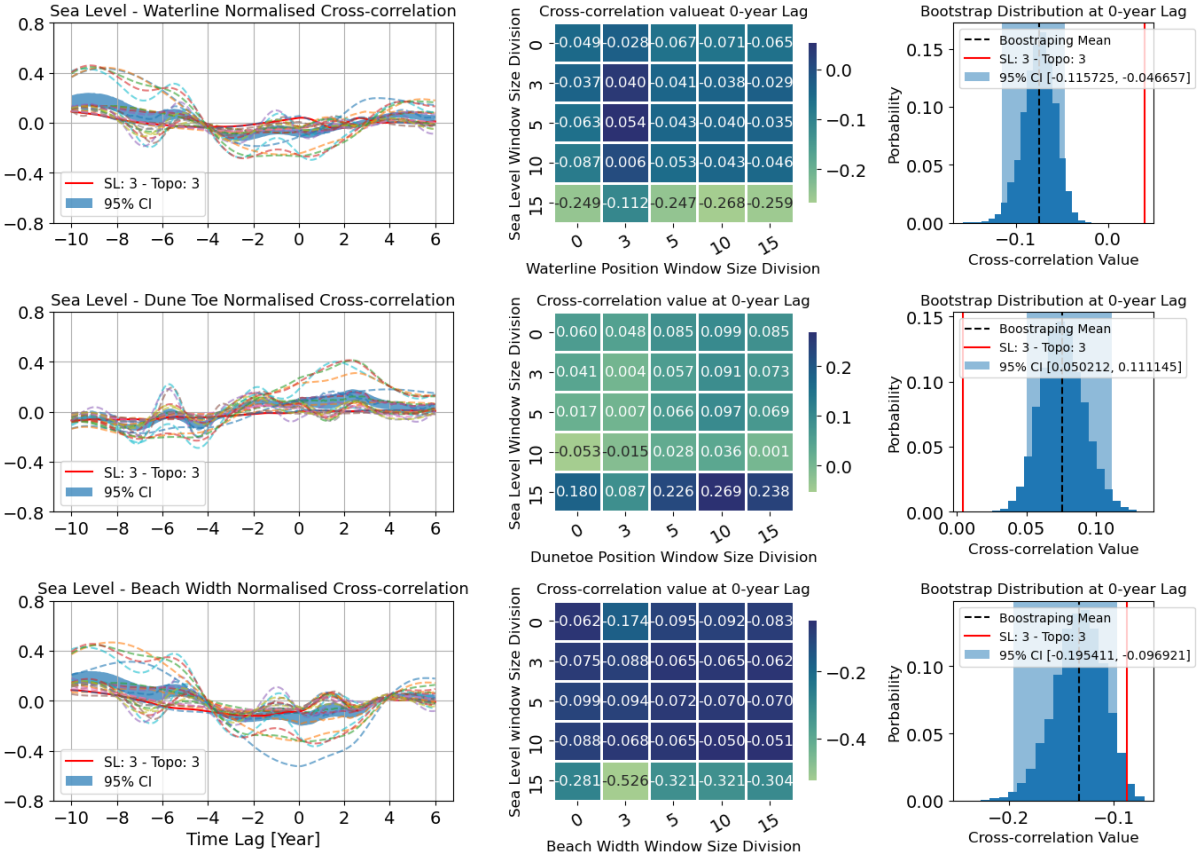

(b) SSA normalized cross-correlation

Figure 3.25: Egmond, Jarkus - Normalized cross-correlation between sea level surface and coastal indicators where the heat map and confidence interval are grounded on zero time-lag results. The legend pairs represent the combination of representative pairs, ”sea level data cutting year - indicator cutting year”.

3.5. Narrabeen

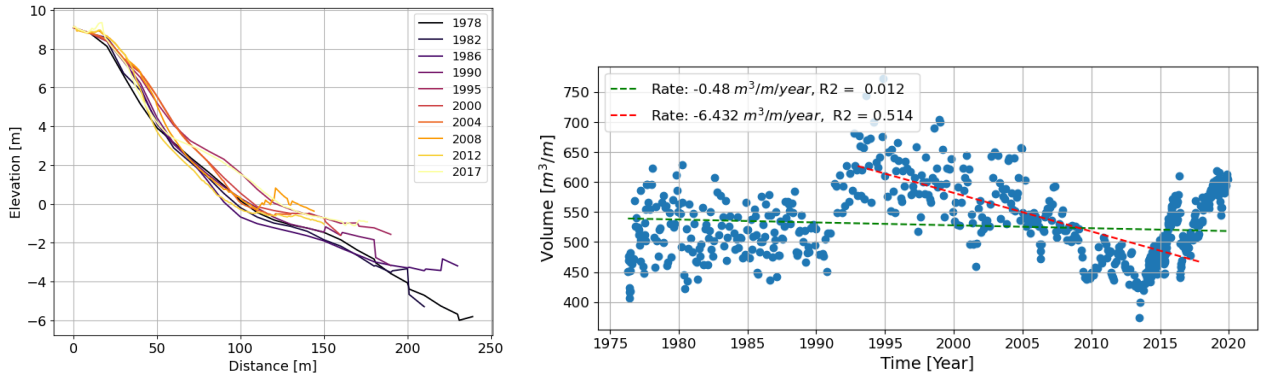

(a) PF1 Profile

(b) PF1 Profile subaerial area beach volume

Figure 3.26: Narrabeen: Evolution of PF1 cross-section profile. The measurement duration is divided into 10 segments for clear display. Beach volume is calculated from the land-water interface to the dune toe position.

Over the past 45 years, no particular migration trend was observed in the Narrabeen PF1 profile under the long-term scale. Figure 3.26 shows that the coastal profile first remained relatively stable between 1976 to 1990, subsequently migrated landward between 1993 to 2014, and moved seaward between 2014 to 2020. Hence, no direct sea level rise-induced coastal recession was discovered from the qualitative perspective of coastal profile evolution.

Figure 3.27 illustrates the power spectrum density analysis of the sea level and coastal indicators at the Narrabeen PF1 profile. The long-term sea level variation directly affected the formation of coastal morphological evolutions. Three long-term detected periods, 14.963-year, 11.22-year, and 8.98-year occur in both oceanic and topographic data, indicating the sea level variation strongly affects the profile development. Furthermore, the homogeneous constituted mechanisms in the three coastal indicators elaborate that the mono environmental transport can simultaneously influence the beach and backshore regions. This motivates the utilization of an event-based cut-off year to extract the long-term signal.

Figure 3.28 and Figure 3.29 display the filtered signals from the IFFT and SSA Model. Alike the reaction of Duck Profile 1097 to rising sea levels, the waterline and dune toe position moved landward, meanwhile, the beach width remained unchanged. Compared to the faster sea level rising rate at Duck, the magnitude at Narrabeen is lower with a rate between 1.96 mm/year to 3.96 mm/year (IFFT) and 3.8 mm/year to 3.96 mm/year (SSA Model). Subsequently, it can be expected that the recession speed for the shoreline position is relatively moderate with recession rates between -0.75 m/year to -1.02 m/year (IFFT) and -1.03 m/year to -1.08 m/year (SSA); for the dune toe position is -0.62 m/year to -0.73 m/year (IFFT), -0.73 m/year to -0.78 m/year (SSA) respectively. The beach width nearly changed in the duration. Adhering to the morphodynamic-based interpretation, 11.22 cut-of-year and N = 11 were selected as the representative values to simulate the long-term behaviours

Figure3.30 illustrates the cross-correlation of the filtered sea level and topographic signals. The shoreline and dune toe position present significant negative correlation values with the rising signal while the relationship with beach width is minor. The bootstrapping results also provide statistical evidence that the cross-correlation values are distinct. Table 3.6 summarises the changing rate of each indicator in the IFFT Model and window size in the SSA Model. The long-term coastal reactions to rising sea levels comply with the ideal coastal profile recession due to sea level rise. Nevertheless, Given the structural variation of the sediment budget, the sediment amount in the subaerial beach was significantly temporal-related and varied abruptly through time. The beach volume gradient implies that the area was experienced by the strong environment sediment transport where the sea level rise

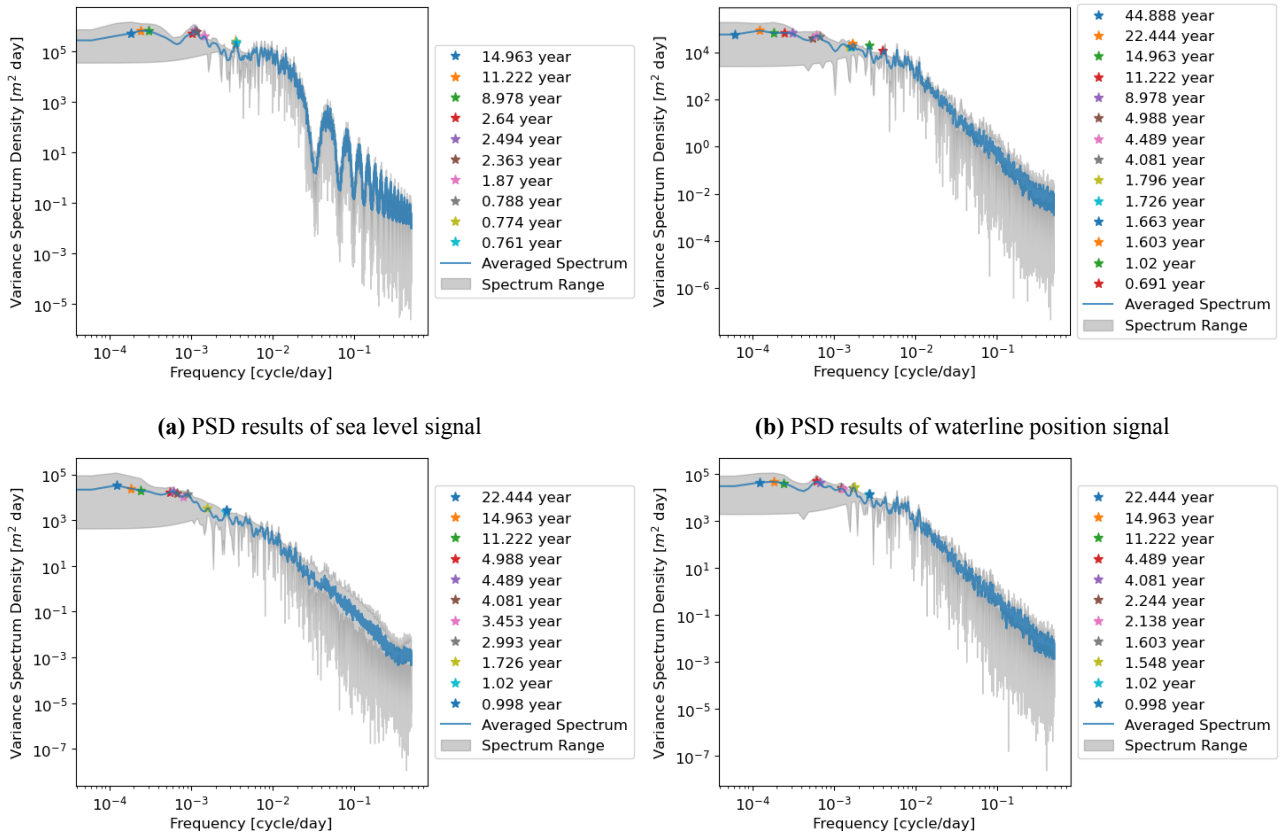

(a) PSD results of sea level signal

(b) PSD results of waterline position signal

(c) PSD results of dune toe position signal

(d) PSD results of beach width signal

Figure 3.27: Narrabeen: Singular spectrum decomposition of sea level and topographic signal for the first eigenmode. N is the total amount of data points where the window size depends on the computation efficiency and high-frequency mechanisms to filter out.

impact may be overshadowed. Recall that the adopted research temporal duration is from 1993 to 2018 (the red dashed line interval in Figure 3.26b), the accelerating rising sea level influence may be augmented. Yet the pure contribution to the beach morphological response from the sea level influence was blurred. On the contrary, the sea level rise-induced coastal recession may be offset by the growing beach volume after 2014.

Table 3.6: Narrabeen: Linear Fitting results of the SSA and IFFT filtered signal, the cut-off year in IFFT Model is 11.222 year and the window size in SSA Model is N/11. SL: sea level variation, SP: shoreline position, DP: dune toe position, BW: beach width

Narrabeen	SL (mm/year)	SP (m/year)	DP (m/year)	BW (m/year)	BV ($m^3/m * year$)
IFFT	3.01	-0.95	-0.7	-0.05	-3.585
Cross-correlation	-	-0.696	-0.755	-0.190	-
SSA	3.8	-1.05	-0.73	-0.01	-3.585
Cross-correlation	-	-0.641	-0.675	-0.064	-

Inverse Fourier Filtering Transform Model

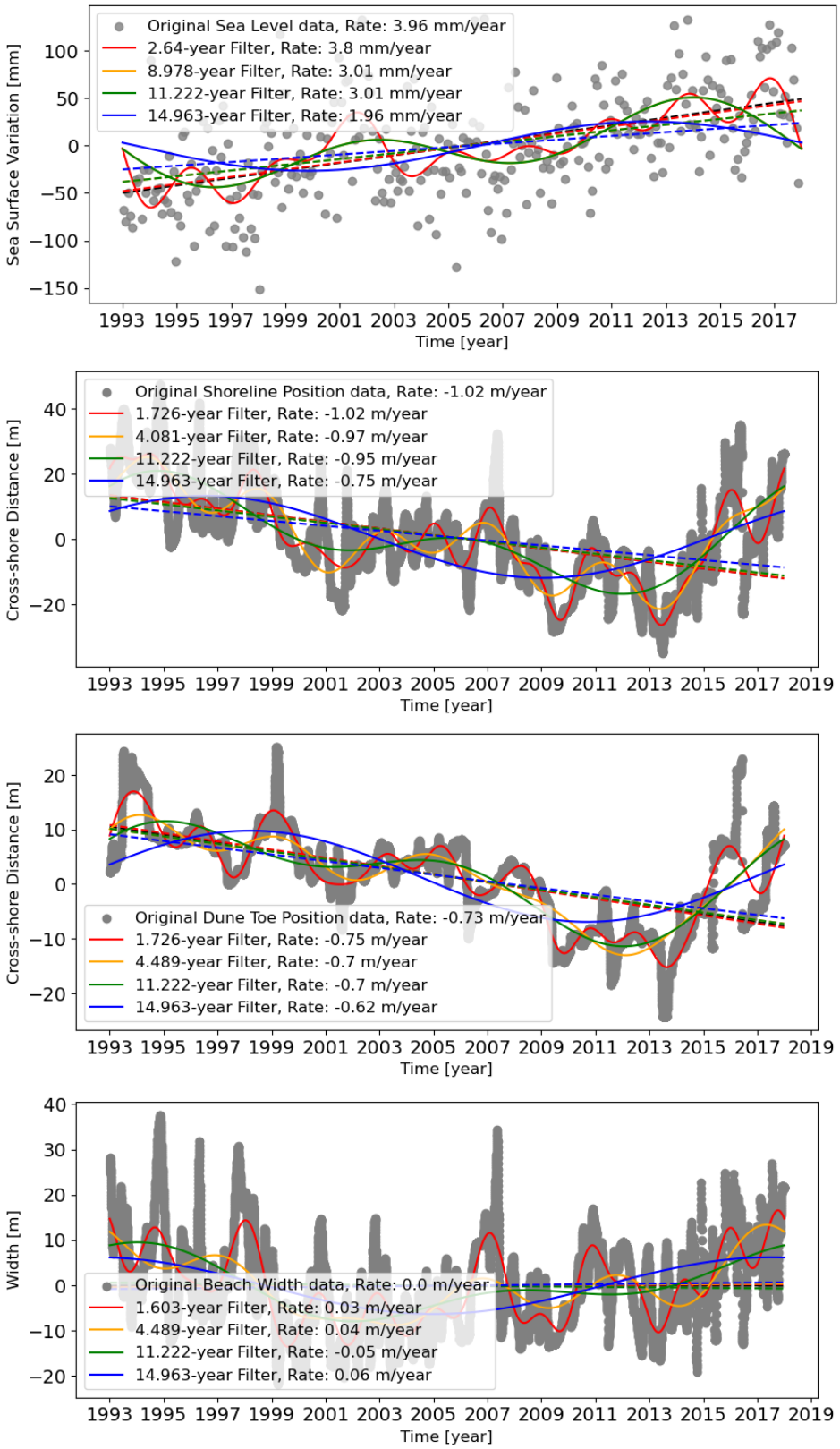

Figure 3.28: Narrabeen: Singular spectrum decomposition of sea level and topographic signal for the first eigenmode. N is the total amount of data points where the window size depends on the computation efficiency and high-frequency mechanisms to filter out.

Singular Spectrum Analysis Model

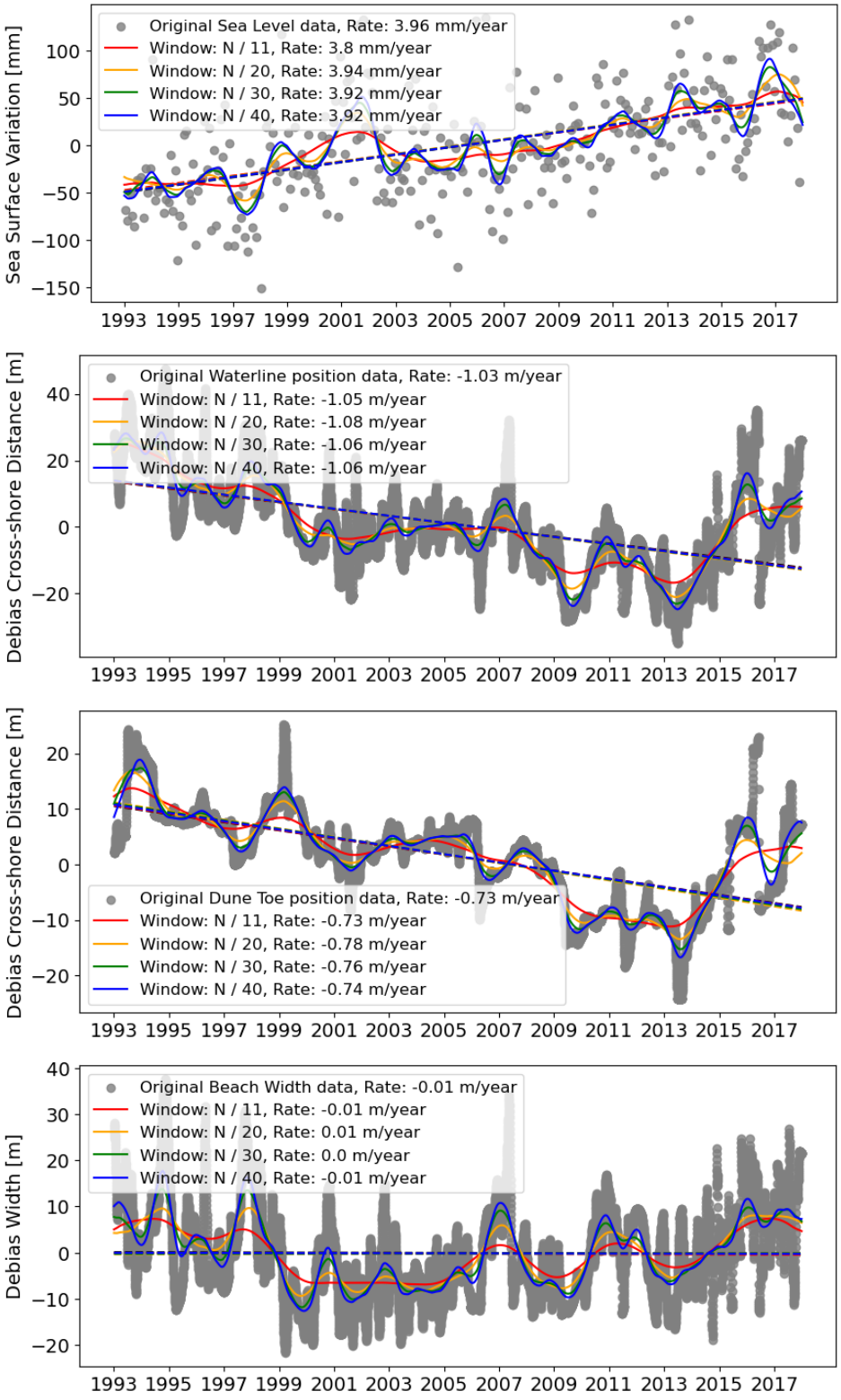

Figure 3.29: Narrabeen: Singular spectrum decomposition of sea level and topographic signal for the first eigenmode. N is the total amount of data points where the window size depends on the computation efficiency and high-frequency mechanisms to filter out.

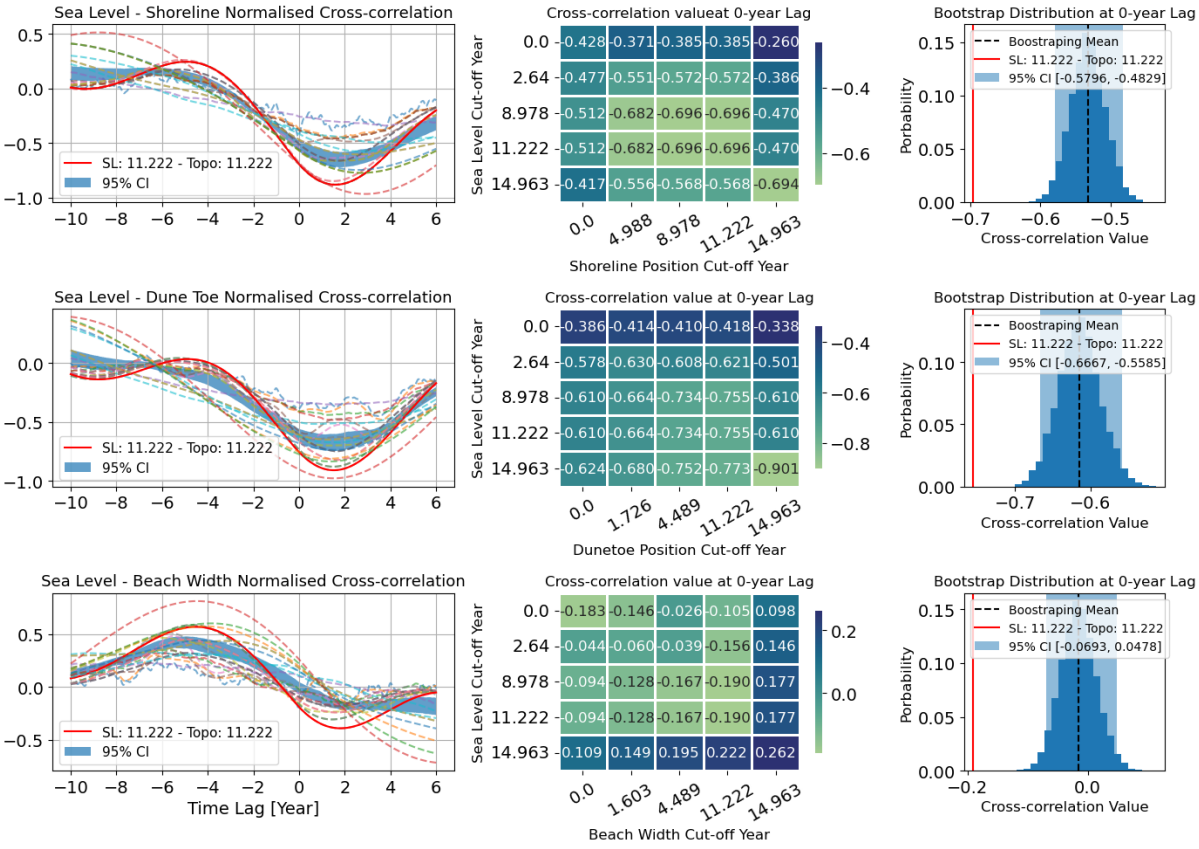

(a) IFFT normalized cross-correlation

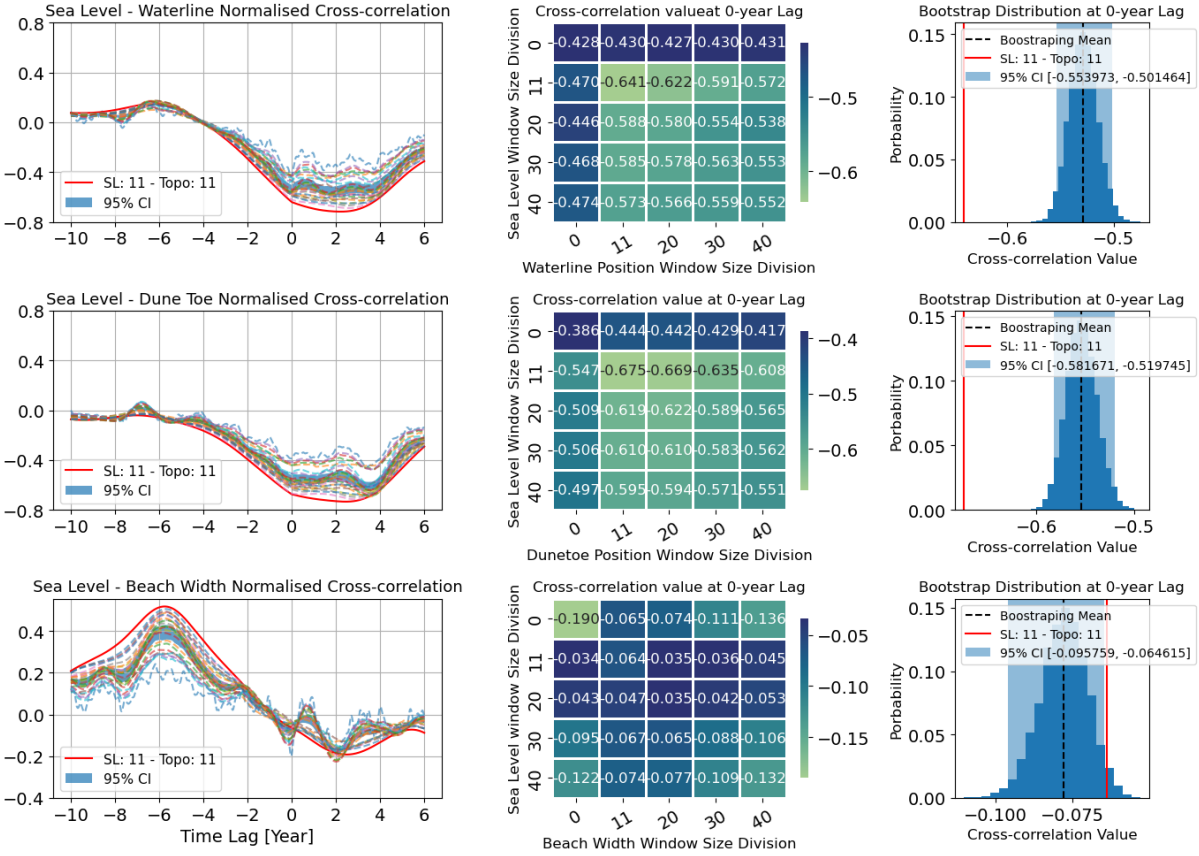

(b) SSA normalized cross-correlation

Figure 3.30: Narrabeen - Normalized cross-correlation between sea level surface and coastal indicators where the heat map and confidence interval are grounded on zero time-lag results. The legend pairs represent the combination of representative pairs, ”sea level data cutting year - indicator cutting year”.

Table 3.7: The Inverse Fourier Filtering Model Result

IFFT	Aquitaine	Duck (No. 1097)	Hasaki	Noordwijk, Jarkus	Egmond, Jarkus	Narrabeen PF1
Sea Level	4.202 mm/year	3.541 mm/year	0.22 mm/year	1.251 mm/year	1.755 mm/year	3.01 mm/year
Waterline	-0.025 m/year	-1.206 m/year	-0.63 m/year	0.464 m/year	0.105 m/year	-0.96 m/year
Correlation	0.267	-0.735	-0.821	0.433	-0.314	-0.696
Dune Toe	0.1 m/year	-1.203 m/year	0.43 m/year	0.05 m/year	0.084 m/year	-0.7 m/year
Correlation	0.128	-0.869	0.950	0.187	0.156	-0.755
Beach Width	0.51 m/year	0.001 m/year	-0.92 m/year	0.451 m/year	-0.023	-0.05 m/year
Correlation	0.766	0.141	-0.980	0.605	-0.385	-0.186
Beach Volume	8.417 m	-1.295	-	-	-	-3.585
Deductions	Alongshore current counteracts the sea level rise influence.	Sea level rise influence might be signicicant. Pier intervention dominates regional variance.	Sea level rise influence is monor. Relatively strong cross-shore transportation.	Coastal progradation outpaces sea level rise influence.	Coastal progradation outpaces sea level rise influence.	Sea level rise might be significant. Recession due to beach oscillations.

Table 3.8: The Singular Spectrum Analysis Model Result

SSA	Aquitaine	Duck (No. 1097)	Hasaki	Noordwijk, Jarkus	Egmond, Jarkus	Narrabeen PF1
Sea Level	3.46 mm/year	4.71 mm/year	0.64 mm/year	1.44 mm/year	1.44 mm/year	3.8 mm/year
Waterline	0.0 m/year	-1.57 m/year	-0.69 m/year	0.52 m/year	0.52 m/year	-1.05 m/year
Correlation	0.043	-0.786	-0.006	0.015	0.040	-0.641
Dune Toe	0.11 m/year	-1.56 m/year	0.48 m/year	0.09 m/year	0.09 m/year	-0.7 m/year
Correlation	-0.188	-0.853	0.088	-0.138	0.004	-0.73
Beach Width	0.82 m/year	0.0 m/year	-1.17 m/year	0.38 m/year	0.38	-0.01 m/year
Correlation	0.798	0.087	-0.043	0.142	-0.088	-0.064
Beach Volume	8.417 m	-1.295	-	-	-	-3.585
Deductions	Alongshore current counteracts the sea level rise influence.	Sea level rise influence might be signicicant. Pier intervention dominates regional variance.	Sea level rise influence is monor. Relatively strong cross-shore transportation.	Coastal progradation outpaces sea level rise influence.	Coastal progradation outpaces sea level rise influence.	Sea level rise might be significant. Recession due to beach oscillations.

Discussion

Two data-driven statistical models were developed to study the morphological response to the rising sea level. Both the Inverse Fourier Filtering (IFFT) Model and the Singular Spectrum Analysis (SSA) Model can efficiently remove the high-frequency mechanisms while capturing the long-term morphological patterns. As the event-based model, the IFFT Model can fully eliminate the constituted period of the signals below the specified year (called the cut-off year). However, the drawback of the IFFT Model can be ascribed to the strong boundary effects, which deviate the calculated linear fitting trend from the original signal. The IFFT Model filters out the specified constituted Fourier series in the signals while merely a few low-frequencies remain. The reconstructed signals from the inverse fast Fourier transform were subsequently restricted to the low frequency and small amplitude long wave. This procedure will tend to smear out the signal by representing the original data with limited sinusoidal waves. In reality, the coastal morphological and sea level variation, will not follow pure sinusoidal behaviours. An improper overlarge cut-off year will render the reconstructed signals purely flat lines and return zero changing rates of the signals.

In contrast, the SSA Model is a mathematics-based model, which deploys the lower-dimensional empirical orthogonal function (EOF) to extract the eigenmodes of the original signals. The first eigenmodes is subsequently regarded as the long-trend of the raw signal. In matters of many EOF analyses, the only parameter to determine the separated signals is window size. This renders the SSA method more rigid. Besides, despite adopting a large window size, the SSA approach can not fully eliminate the undesired seasonality or high-frequency events. Another critical downside of the singular spectrum analysis is obvious in corresponding to the physics-meaningless eigenmodes. Even though the recommended window length has been proposed in previous research, the researchers are still required to interpret the possible corresponding phenomenon consciously. The separated eigenvectors contain no physical meanings but a pure time series. The parameter-restricted procedure forces the researcher to manually interpret the trend. The potential beach responses to rising sea levels can thus be blurred or oversimplified, violating the presumption of sophisticated morphological changes.

The underlying hypotheses on the dynamics of changes in observation-based approaches are significant obstacles to unravelling the detailed morphological evolution. By using the power spectrum density as an auxiliary tool, the accurate sources of composition forces in the sea level or topographic signals remain unknown. Distinct selection of parameters in the model will lead to various results, providing divergent morphological patterns. In these two models, the candidate of filters is based on the existing and uniform driving forces portrayed in the spectrum analysis. Yet, there are no strict criteria providing the optimal choice but a hydrodynamic and morphological conjecture. A 15-year filter in one coastal site may not filter out the unwanted non-sea level rise-induced signal, meanwhile, a 10-year filter can also filter out too much signal. An inadequate cut-off year will lead to unwanted noises or over-clean signals.

From the coastal dynamic equilibrium perspective, the beach volume provides an alternative to detour the requirement of environmental transportation magnitudes. Yet, the calculated amount is highly dependent on the data continuity, proper spatiotemporal resolution, measurement range, and the defined calculating boundaries. The collected surveying datasets at Aquitaine and Narrabeen were more focused on the subaerial region while more focused on the submerged region at Duck. Different boundaries adopted will result in totally different results, rendering the uncertainty to a certain degree. Furthermore, the recent couple-year surveying range at Duck did not fully cover the coastal active zone, resulting in a requirement of value extrapolation. The extrapolated coastal volume values may lead to another uncertainty in sediment budget deduction.

The implemented cross-correlation analysis on the filtered signals provides insight into the relation-

ship between two distinct variables. A possible deficiency in the cross-correlation study between rising sea levels and topographic responses is the implicit pseudo-relation. For instance, the sea level and the beach width present a high correlation with each other, implying the rising sea level leads to an increasing subaerial beach width. But, in fact, the increasing beach width is owing to the alongshore sediment accretion rather than the rising sea level. In contrast, even if the cross-correlation results from all indicators properly reflect the ideal sea level rise-induced coastal recession, a pseudo-correlation may still exist.

Results from the Narrabeen PF1 Profile suggested the sea level rise strongly affected the profiles during the past two decades. Three coastal indicators reflect an ideal sea level rise-induced coastal retrogradation. However, Harley et al. (2011) revealed a beach oscillation phenomenon in the Narrabeen embayment beach where the adopted temporal scope in this research precisely overlapped. This phenomenon can either overshadow or augment the sea level rise-induced recession. It is thus difficult to attribute the coastal recession to the long-term rising sea level at the coastal site. Even though the filtering techniques were applied to remove high-frequency mechanisms, it is still burdensome to discern the source of morphological changes. This suggests that a longer research period is required to fully eliminate the seasonality.

Despite the fact that changing rates of each coastal indicator were qualitatively computed, the magnitude of coastal morphological response to sea level rise remains ambiguous. Another coastal site reflecting the possible sea level rise impact is Duck Profile 1097. For instance, the IFFT and SSA models suggest that the shoreline retreating rates are -1.2 meters per year and -1.5 meters per year respectively after the deployment of the filter. These values are much larger than the calculated values by using the Bruun Rule, implying more sediment transport was involved. This can be seen from the comparison between PSD analysis of sea level variation and shoreline position signal. Without the auxiliary hydrodynamic conditions and sediment transportation model, it is difficult to ascribe the ratio of coastal morphological changes to different sources under the 1D time series conditions. The long-term coastal recession is governed either by the sea level rise-induced erosion, environmentally related structural loss, or the superimposition of these two phenomena.

Both the IFFT and SSA Analysis demonstrate the observed counteraction to sea level rise impact by the environmental sediment transportation in the selected research profiles of Aquitaine, Hasaki, Noordwijk, and Egmond within the last two decades. It is not unexpected to neglect the potential hazard while assessing the coastal risk in coastal management. Evaluating the regional sea level rise impact in the future is intricate due to the non-linear interactions between rising sea levels and hydrodynamic conditions. The higher water table may amplify the impact that more waves penetrate into the upper shoreface and suppress sediment accretion, whereas more severe hydrodynamics may also lead to more sediment structural gain. Hence, a better qualitative assessment of the impact of sea level rise on the coastal region requires implementing multiple models and complete observation.

Conclusion

Decadal coastal datasets were analysed to unravel the correlation between long-term sea level rising trends and sandy beach morphological responses. To compare the regional difference from the global perspective, five coastal datasets with measurement duration over two decades. Followed by the widely adopted equilibrium coastal profile in the sea level rise study, the waterline position, dune toe position and beach width were used as the coastal indicators pragmatically. The indicator's spatial evolution reveals the spatiotemporal coastal migration of interaction of the sea level rise impact and ambient sediment transport.

Two statistical data-driven models were employed to capture the long-term variation in the time series. The inverse Fourier filtering transform (IFFT) model encompasses two steps, detecting the embedded seasonality by power spectrum density and reconstructing the signals by filtering out the specified cut-off year. This endowed the IFFT model to eliminate all the high-frequency oscillations, serving as a flexible and physics-based model. In contrast, the singular spectrum analysis (SSA) model first decomposes the original time series into multiple eigenmodes and then utilises the power spectrum density to inspect the remaining constituted frequency. It can properly capture the long-term trend in the signal and present a good fitting in event-induced variation whereas some high-frequency hydrodynamic mechanisms still stay in the trend.

These models can satisfyingly alleviate the high-frequency mechanism fluctuations embedded in the time series, nevertheless, the sediment structural gain/loss is still embedded in the time series. Without the assistance of longshore transport models, the corresponding magnitude remains ambiguous and subtle. As compensation, the long-term beach volume change performs a baseline for sediment conservation in supporting the outcomes of statistical models. Based on the employment of these two models in the decadal signals, the results of each coastal site can be summarized as follows.

1. Aquitaine: Long-term environmental sediment transport in Southern Aquitaine Coast offsets the sea level rise-induced coastal recession. Because of the prevailing alongshore current, the waterline and dune toe positions have gradually moved seaward with an increasing beach width. Low cross-correlation was found between sea level rising trend and topographic response.
2. Duck: Obvious regional variability regarding sea level rise impact exists at the Duck Coast, where the FRF pier strongly influences the waterline evolution. Updrift accretion counteracts the sea level rise influence while the downdrift erosion augments the impact. Sea level rise may significantly affect the location deviated from the vicinity of alongshore transport intervention, leading to an entire coastal recession. The coastal profile responds to sea level rise intra-annually.
3. Hasaki: The vertical land movement counterbalance the rising sea level, resulting in a slow rising rate. The waterline and dune toe positions show an opposite migration direction, which may be ascribed to the prevailing strong cross-shore sediment transport. A three-year cross-correlation lag was found and possibly attributed to coastal adaption to sea level rise while the detailed mechanism remains still unknown.
4. Jarkus: The environmental sediment transport dominates the coastal profile evolution in North Holland Coast and Wadden Sea Coast. Coastal profiles slowly migrate seaward, overriding the sea level rise impact. No cross-correlation was found between sea level rising trend and beach morphological change.
5. Narrabeen: The embayment beach oscillation overshadows the coastal profile variation, hindering the evaluation of sea level rise impact. The oscillation period is approximately 25-30 years, suggesting that indicating a clear relationship is still difficult under a two-decadal measurement. The strong cross-correlation arose due to the overlapping interval of the shoreline retreating period in the oscillation.

In summary, the required time span for statistically unravelling the sea level rise may be over several decades. Within the short-term engineering scale, the ambient structural gain can counteract the sea level rise-induced recession. Yet, careful assessment of the coastal hazard by sea level rise should be taken into serious account to confront future challenges. This research may contribute to a better understanding of the relationship between sea level rise and accompanying subaerial beach morphology. The correlation results identify the nature of the phenomenon and provide a direct reference of the coastal response to sea level rise. This knowledge is important for engineers to take the appropriate coastal management and meanwhile be a keystone for developing advanced models in the future.

References

Aagaard, T., Davidson-Arnott, R., Greenwood, B., & Nielsen, J. (2004). Sediment supply from shoreface to dunes: linking sediment transport measurements and long-term morphological evolution. *Geomorphology*, *60*(1), 205-224.

Beckley, B. D., Callahan, P. S., Hancock III, D. W., Mitchum, G. T., & Ray, R. D. (2017). On the "cal-mode" correction to topex satellite altimetry and its effect on the global mean sea level time series. *Journal of Geophysical Research: Oceans*, *122*(11), 8371-8384.

Bosboom, J., & Stive, M. J. (2021). Coastal dynamics.

Bracewell, R., et al. (1965). Pentagram notation for cross correlation. the fourier transform and its applications. *New York: McGraw-Hill*, *46*, 243.

Broomhead, D., & King, G. P. (1986). Extracting qualitative dynamics from experimental data. *Physica D: Nonlinear Phenomena*, *20*(2), 217-236.

Bruun, P. (1962). Sea-level rise as a cause of shore erosion. *Journal of the Waterways and Harbors Division*, *88*(1), 117-130.

Burvingt, O., & Castelle, B. (2023). Storm response and multi-annual recovery of eight coastal dunes spread along the atlantic coast of europe. *Geomorphology*, *435*, 108735.

Casamayor, M., Alonso, I., Valiente, N. G., & Sánchez-García, M. J. (2022). Seasonal response of a composite beach in relation to wave climate. *Geomorphology*, *408*, 108245.

Cazenave, A., & Cozannet, G. L. (2014). Sea level rise and its coastal impacts. *Earth's Future*, *2*(2), 15-34.

Coco, G., & Murray, A. B. (2007). Patterns in the sand: From forcing templates to self-organization. *Geomorphology*, *91*(3), 271-290. (38th Binghamton Geomorphology Symposium: Complexity in Geomorphology)

Cohn, N., Brodie, K., Conery, I., & Spore, N. (2022). Alongshore variable accretional and erosional coastal foredune dynamics at event to interannual timescales. *Earth and Space Science*, *9*(12), e2022EA002447.

Cooley, J. W., & Tukey, J. W. (1965). An algorithm for the machine calculation of complex fourier series. *Mathematics of computation*, *19*(90), 297–301.

Core Writing Team, J. R., H. Lee. (2023). *Ipcc, 2023: Climate change 2023: Synthesis report. sixth assessment report of the intergovernmental panel on climate change* (Tech. Rep.). IPCC, Geneva, Switzerland.

Dastgheib, A., Martinez, C., Udo, K., & Ranasinghe, R. (2022). Climate change driven shoreline change at hasaki beach japan: A novel application of the probabilistic coastline recession (pcr) model. *Coastal Engineering*, *172*, 104079.

Dean, R., & Houston, J. (2016). Determining shoreline response to sea level rise. *Coastal Engineering*, *114*, 1-8.

Do, Anh TK, de Vries, Sierd, & Stive, Marcel JF. (2019). The estimation and evaluation of shoreline locations, shoreline-change rates, and coastal volume changes derived from landsat images. *Journal of Coastal Research*, *35*(1), 56–71.

Feagin, R. A., Sherman, D. J., & Grant, W. E. (2005). Coastal erosion, global sea-level rise, and the loss of sand dune plant habitats. *Frontiers in Ecology and the Environment*, *3*(7), 359-364.

FitzGerald, D. M., Fenster, M. S., Argow, B. A., & Buynevich, I. V. (2008). Coastal impacts due to sea-level rise. *Annu. Rev. Earth Planet. Sci.*, *36*, 601–647.

Ghil, M., Allen, M. R., Dettinger, M. D., Ide, K., Kondrashov, D., Mann, M. E., … Yiou, P. (2002). Advanced spectral methods for climatic time series. *Reviews of Geophysics*, *40*(1), 3-1-3-41.

Hannachi, A., Jolliffe, I. T., Stephenson, D. B., et al. (2007). Empirical orthogonal functions and related techniques in atmospheric science: A review. *International journal of climatology*, *27*(9), 1119–1152.

Harley, M. D., Masselink, G., Ruiz de Alegría-Arzaburu, A., Valiente, N. G., & Scott, T. (2022). Single extreme storm sequence can offset decades of shoreline retreat projected to result from sea-level rise. *Communications Earth & Environment*, *3*(1), 112.

Harley, M. D., Turner, I. L., Short, A. D., & Ranasinghe, R. (2011). A reevaluation of coastal embayment rotation: The dominance of cross-shore versus alongshore sediment transport processes, collaroy-narrabeen beach, southeast australia. *Journal of Geophysical Research: Earth Surface*, *116*(F4).

Harvey, T. C., Hamlington, B., Frederikse, T., & Nerem, R. S. (2020). Drivers of coastal united states relative sea-level trends during the satellite altimeter-era. In *Agu fall meeting abstracts* (Vol. 2020, pp. OS007–04).

Hauer, M. E., Fussell, E., Mueller, V., Burkett, M., Call, M., Abel, K., … Wrathall, D. (2020). Sea-level rise and human migration. *Nature Reviews Earth & Environment*, *1*(1), 28–39.

Hesp, P. (2002). Foredunes and blowouts: initiation, geomorphology and dynamics. *Geomorphology*, *48*(1), 245-268. (29th Binghamton Geomorphology Symposium: Coastal Geomorphology)

Houser, C., Wernette, P., Rentschlar, E., Jones, H., Hammond, B., & Trimble, S. (2015). Post-storm beach and dune recovery: Implications for barrier island resilience. *Geomorphology*, *234*, 54-63.

Idier, D., Bertin, X., Thompson, P., & Pickering, M. D. (2019). Interactions between mean sea level, tide, surge, waves and flooding: mechanisms and contributions to sea level variations at the coast. *Surveys in Geophysics*, *40*(6), 1603–1630.

Kiguchi, M., Takata, K., Hanasaki, N., Archevarahuprok, B., Champathong, A., Ikoma, E., … others (2021). A review of climate-change impact and adaptation studies for the water sector in thailand. *Environmental Research Letters*, *16*(2), 023004.

Kuriyama, Y. (2002). Medium-term bar behavior and associated sediment transport at hasaki, japan. *Journal of Geophysical Research: Oceans*, *107*(C9), 15-1-15-12.

Larson, M., Capobianco, M., & Hanson, H. (2000). Relationship between beach profiles and waves at duck, north carolina, determined by canonical correlation analysis. *Marine Geology*, *163*(1), 275-288.

Larson, M., Capobianco, M., Jansen, H., Rózyński, G., Southgate, H. N., Stive, M., … Hulscher, S. (2003). Analysis and modeling of field data on coastal morphological evolution over yearly and decadal time scales. part 1: Background and linear techniques. *Journal of Coastal Research*, *19*(4), 760–775.

Le Cozannet, G., Garcin, M., Yates, M., Idier, D., & Meyssignac, B. (2014). Approaches to evaluate the recent impacts of sea-level rise on shoreline changes. *Earth-Science Reviews*, *138*, 47-60.

Lentz, E. E., Thieler, E. R., Plant, N. G., Stippa, S. R., Horton, R. M., & Gesch, D. B. (2016). Evaluation of dynamic coastal response to sea-level rise modifies inundation likelihood. *Nature Climate Change*, *6*(7), 696–700.

Lincke, D., & Hinkel, J. (2021). Coastal migration due to 21st century sea-level rise. *Earth's Future*, *9*(5), e2020EF001965.

Luque, P., Gómez-Pujol, L., Ribas, F., Falqués, A., Marcos, M., & Orfila, A. (2023). Shoreline response to sea-level rise according to equilibrium beach profiles. *Scientific Reports*, *13*(1), 15789.

Masselink, G., Brooks, S., Poate, T., Stokes, C., & Scott, T. (2022). Coastal dune dynamics in embayed settings with sea-

level rise–examples from the exposed and macrotidal north coast of sw england. *Marine Geology*, *450*, 106853.

Nicolae Lerma, A., Castelle, B., Marieu, V., Robinet, A., Bulteau, T., Bernon, N., & Mallet, C. (2022). Decadal beach-dune profile monitoring along a 230-km high-energy sandy coast: Aquitaine, southwest france. *Applied Geography*, *139*, 102645.

Nina Golyandina, A. Z. (2013). *Singular spectrum analysis for time series*. Springer Berlin, Heidelberg.

Phillips, J. D. (2018). Environmental gradients and complexity in coastal landscape response to sea level rise. *CATENA*, *169*, 107-118.

Prabhu, K. M. (2014). *Window functions and their applications in signal processing*. Taylor & Francis.

Ranasinghe, R., Callaghan, D., & Stive, M. J. (2012). Estimating coastal recession due to sea level rise: beyond the bruun rule. *Climatic Change*, *110*, 561–574.

Schuerch, M., Spencer, T., Temmerman, S., Kirwan, M. L., Wolff, C., Lincke, D., … others (2018). Future response of global coastal wetlands to sea-level rise. *Nature*, *561*(7722), 231–234.

Schuster, A. (1898). On the investigation of hidden periodicities with application to a supposed 26 day period of meteorological phenomena. *Terrestrial Magnetism*, *3*(1), 13-41.

Smith, J. O. (2008). *Mathematics of the discrete fourier transform (dft): with audio applications*. Julius Smith.

Spada, G., Bamber, J. L., & Hurkmans, R. T. W. L. (2013). The gravitationally consistent sea-level fingerprint of future terrestrial ice loss. *Geophysical Research Letters*, *40*(3), 482-486.

Spanhoff, R., Biegel, E. J., Burger, M., & Dunsbergen, D. W. (2003). Shoreface nourishments in the netherlands. In *Proceedings coastal sediments* (Vol. 3).

Stammer, D., Cazenave, A., Ponte, R. M., & Tamisiea, M. E. (2013). Causes for contemporary regional sea level changes. *Annual review of marine science*, *5*, 21–46.

Suanez, S., Yates, M., Floc'h, F., & Accensi, M. (2023). Using 17 years of beach/dune profile monitoring to characterize morphological dynamics related to significant extreme water level events in north brittany (france). *Geomorphology*, *433*, 108709.

Turner, I. L., Harley, M. D., Short, A. D., Simmons, J. A., Bracs, M. A., Phillips, M. S., & Splinter, K. D. (2016). A multi-decade dataset of monthly beach profile surveys and inshore wave forcing at narrabeen, australia. *Scientific data*, *3*(1), 1–13.

Uehara, K., Sojisuporn, P., Saito, Y., & Jarupongsakul, T. (2010). Erosion and accretion processes in a muddy dissipative coast, the chao phraya river delta, thailand. *Earth Surface Processes and Landforms*, *35*(14), 1701-1711.

van IJzendoorn, C. O., de Vries, S., Hallin, C., & Hesp, P. A. (2021). Sea level rise outpaced by vertical dune toe translation on prograding coasts. *Scientific reports*, *11*(1), 12792.

Vautard, R., & Ghil, M. (1989). Singular spectrum analysis in nonlinear dynamics, with applications to paleoclimatic time series. *Physica D: Nonlinear Phenomena*, *35*(3), 395-424.

Vitousek, S., Barnard, P. L., Limber, P., Erikson, L., & Cole, B. (2017). A model integrating longshore and cross-shore processes for predicting long-term shoreline response to climate change. *Journal of Geophysical Research: Earth Surface*, *122*(4), 782-806.

Welch, P. (1967). The use of fast fourier transform for the estimation of power spectra: A method based on time averaging over short, modified periodograms. *IEEE Transactions on Audio and Electroacoustics*, *15*(2), 70-73.

Woodworth, P. L., Melet, A., Marcos, M., Ray, R. D., Wöppelmann, G., Sasaki, Y. N., … others (2019). Forcing factors affecting sea level changes at the coast. *Surveys in Geophysics*, *40*(6), 1351–1397.

Wu, W., Biber, P., & Bethel, M. (2017). Thresholds of sea-level rise rate and sea-level rise acceleration rate in a vulnerable coastal wetland. *Ecology and Evolution*, *7*(24), 10890-10903.

Zhang, J., & Larson, M. (2021). Decadal-scale subaerial beach and dune evolution at duck, north carolina. *Marine Geology*, *440*, 106576.

Zhao, J., Huang, S., Huang, Q., Wang, H., Leng, G., & Fang, W. (2020). Time-lagged response of vegetation dynamics to climatic and teleconnection factors. *CATENA*, *189*, 104474.

Equation Derivation Appendix

7.1. Inverse Fourier Filter Transform

An important technique to characterize the rhythmic feature within the time series signal is the power spectral density (PSD), which depicts the power distribution among the constituted frequency. Three approaches (Direct Conversion, Periodogram, and Welch's Method) are hereby introduced for the spectrum probability calculation. Firstly, the Cooley–Tukey Fast Fourier Transform (FFT) (Cooley & Tukey, 1965), served as the most popular algorithm to compute the discrete Fourier transform (DFT). This approach was used to perform the direct conversion from the time domain to the frequency domain. Secondly, (Schuster, 1898) proposed the periodogram, which is the common power spectral density estimation method. The entire signal is expressed by harmonic frequencies and concurrently converted into PSD by DFT. Despite the convenience and simplicity of these two approaches, the "grassy" signal will consequently be generated due to the full fast Fourier transform (undertaken of one FFT on the entire signal). One method to improve the result of the chaotic spectrum is via Welch's Method (Welch, 1967). Welch's method compartments the time series signal into several (overlapping) snippets and applies FFT on each of them. In this case, the signal in the frequency domain can be distinguished if there is an abrupt change in seasonality formation within the time domain. The final step of Welch's method is to average over the converted power spectrum, smoothing the spectrum meanwhile maintaining the spectrum characteristic of the initial signal. Figure **??** illustrates the PSD comparison by using these three methods.
The signal compartmentation associated with non-periodic FFT will result in two downsides (Prabhu, 2014), augmentation of FFT's boundary effect and spectral leakage. An appropriate way to improve Welch's method is via window functions (also called signal tapering) (Smith, 2008). These window functions will taper the data to zero and constrict the signal oscillation at the boundaries (endpoints), reducing the effect of leakage and boundary signal deviations. Zero-padding is the final step to facilitate processed data quality. It is a technique of adding zeros behind the time series sequence, which elongates the vector employed in the fast Fourier Transform. Typically the sequence's size is extended to equal a power of two for efficient implementation in the radix-2 butterflies step in the FFT algorithm (Prabhu, 2014). A longer FFT signal will increase the bins in the frequency domains, leading to a finer frequency resolution, yet meanwhile, coerce the signal in the frequency domain to become more chaotic. Therefore, one more two to the power of order is extended. For example, if the time series has 400 data points, the series will be elongated to 2^9. To capture the sea level rise signal, the size of the 5-year snippet with Hann window and 50 % overlapped is implemented.

7.2. Singular Spectrum Analysis

The singular spectrum analysis (SSA) can be dated back to 1986 (Broomhead & King, 1986), who applied a method in the delays of the dynamical system to estimate the dimension and reconstruct the Lorenz attractor by using singular-value decomposition (SVD) on the trajectory matrix. Later in 1989, Vautard and Ghil (Vautard & Ghil, 1989) indicated SSA as an application to the Karhunen-Loeve decomposition, which states that a stochastic process can be represented as the infinite linear superimposition of orthogonal functions. From there, SSA can be perceived as a particular case of empirical orthogonal function (EOF) analysis at a specific location (Zhang & Larson, 2021).

SSA aims to decompose the original signal series into a sum of subset components, including varying trends, oscillations, periodic signals, and noise. The algorithm can be separated into four main steps, raw signal decomposition and subset reconstruction. A brief introduction to SSA is shown as the following, the detailed process can be derived from (Nina Golyandina, 2013). In the first step, the lagged vectors are extracted from the original time series and further embedded into a trajectory

matrix. Consider a real value, non-zero and finite original time series as $\Phi = [x_1, x_2, \ldots, x_N]$ of size N, the window size as L, and the K number lagged vectors X_i (K = N - L + 1).

The lagged vectors X_i and trajectory matrix $\mathbf{X}$ are defined respectively as:

$$X_i = (x_i, x_{i+1}, x_{i+2}, \ldots, x_{i+L-1})^T \quad (1 \leq i \leq K) \tag{7.1}$$

$$\mathbf{X} = [X_1, X_2, X_3, \ldots, X_K] = \begin{bmatrix} x_1 & x_2 & x_3 & \ldots & x_K \\ x_2 & x_3 & x_4 & \ldots & x_{K+1} \\ . & . & . & \ldots & . \\ . & . & . & \ldots & . \\ . & . & . & \ldots & . \\ x_L & x_{L+1} & x_{L+2} & \ldots & x_N \end{bmatrix} \tag{7.2}$$

The second step is to utilize the singular spectrum decomposition for the trajectory matrix X where its SVD of Gramian matrix ($S = A^T A$) can be rewritten into subsets of matrices (also called elementary matrices) as

$$\mathbf{X} = [\mathbf{X}_1, \mathbf{X}_2, \mathbf{X}_3, \ldots, \mathbf{X}_d] \quad where \quad d = rank(\mathbf{X}) \tag{7.3}$$

Each of the subset matrices is then constituted by the so-called i^{th} eigentriple of the SVD (Equation 7.4). The eigenvalues are denoted by λ and sequenced in the decreasing order of magnitudes ($\lambda_1 > \lambda_2 > \cdots > \lambda_L > 0$). U vectors ($U_1, U_2, \ldots, U_L$) are the corresponding eigenvectors of these eigenvalues.

$$\mathbf{X_i} = \sqrt{\lambda_i} U_i V_i^T \tag{7.4}$$

The third step is to separate these elementary matrices into several groups $I = [I_1, I_2, \ldots, I_m]$ with the specified combination of indices $I_i = [i_1, i_2, i_3, \ldots, i_p]$, and sum them up the within the groups.

$$\mathbf{X} = \mathbf{X_{I_1}} + \mathbf{X_{I_2}} + \cdots + \mathbf{X_{I_m}} \tag{7.5}$$

The Final step in SSA is diagonally averaging the grouped matrices from the Equation (7.5) and producing the elementary reconstructed series $\chi^{(k)} = [\tilde{x}_1^{(k)}, \ldots, \tilde{x}_N^{(k)},]$ (right-hand part of Equation (7.6)) which the initial series Φ (left-hand part of Equation (7.6)) is decomposed into.

$$x_n = \sum_{k=1}^{m} \tilde{x}_n^{(k)} \quad (n = 1, 2, \ldots, N) \tag{7.6}$$

Hereafter we use the eigenmode (see Figure 2.21) to represent the pair result from SSA, corresponding to different selected combinations of elementary matrices in the grouping mentioned in step three. Four eigenmodes were sketched for SSA on all raw signals for better result visualisation. Moreover, each group contains only one elementary matrix, preserving the main trend of the raw signal as SSA1 and meanwhile spilt parts of the unwanted seasonality and noise from SSA2 to SSA4.

As an advanced time series technique, SSA can efficiently and properly capture the non-linear, non-harmonic, box-shape, saw-tooth-shape signals owing to its data-adaptive properties (Ghil et al., 2002). This surpasses the necessary many overtones of basis functions for depicting the complicated regression model. An example is that SSA can describe a square wave directly while massive Fourier series are superimposed to capture the trend. Moreover, neither the stationary time series nor model parameters are required for SSA, endowing the application with fewer restrictions and parameter

training. Despite its powerfulness, SSA has critical flaws as the ”lower dimension” application of EOF analysis. Firstly, there is no direct physical meaning of the eigenmode but the researcher has to propose the interpretation for corresponding phenomena. Secondly, the significant difference in behaviours of SSA outcomes merely depends on the window size and grouping, rendering it a relatively rigid approach.

Selecting a suitable window size is subsequently very important in SSA. In general, the window size is bounded in the interval $2 \leq L \leq N/2$. The larger the L, the more detail will be decomposed (Zhang & Larson, 2021; Nina Golyandina, 2013), providing a strong separation concerning the small perturbation in L. On the contrary, a too-large window size can over-separate the signal of interest and mix up with other eigenmodes. Adoptions of window size are different based on the obtained coastal data and will be introduced later. In the sea level rising study, we expect an implicit but embedded trend to exist and hence employ a relatively smaller window size to prevent eigenmodes from mixing up, shown in Figure 2.21.